The top-quark pair-production cross-section measurement in the dilepton final states at proton-proton collisions with $\sqrt{s}$ =7 TeV

Yasuyuki Okumura
Nagoya University
okumura@hepl.phys.nagoya-u.ac.jp

Abstract

This thesis presents the results of the top-quark pair-production ($t\bar{t}$ production) cross-section measurement at proton-proton collisions with $\sqrt{s} = 7$ TeV at the Large Hadron Collider (LHC), which is the energy frontier accelerator as of 2011. The top-quark (t-quark) is the heaviest of all known particles, and it was discovered at the Tevatron with $\sqrt{s} = 1.96$ TeV in 1995. Owing to its largest mass, the t-quark is expected to be sensitive for new phenomena, and thus a precise measurement of the $t\bar{t}$ production at the energy frontier is one of the first priorities of experimental particle physics programs.

This analysis uses 0.70 fb^{-1} of pp collision data corresponding to production of 10^5 times of the $t\bar{t}$ creations, which has already exceeded the number of $t\bar{t}$ pairs produced at the Tevatron. The analysis extracts the $t\bar{t}$ events in final states characterized by two isolated high p_T leptons, a large missing transverse momentum (E_T^{miss}) corresponding to two neutrinos from leptonic W boson's decays, and jets originating from b-quarks, which are so-called "dilepton final states". The measurement is based on the well-evaluated detector performances especially in the high intensity environment of the LHC. The following has been achieved owing to the intensive study of the detector performance: (1) the optimization of the $t\bar{t}$ event selection, (2) the evaluation of the signal acceptance, and (3) the background rate estimation. Thus far, 1,400 candidate events were obtained from the pp collision data with expected the signal purity of 83%. Using the obtained samples, the cross-section is measured to be:

$$175 \pm 6 \text{ (stat.)} \, ^{+14}_{-11} \text{ (syst.)} \pm 8 \text{ (lumi.) pb},$$

where stat, syst, and lumi denote the statistical error, the sum of systematic errors, and the uncertainty originating from the luminosity determination, respectively. This result is in good agreement with the SM prediction of 164.6 $^{+11.5}_{-15.8}$ pb. The uncertainty level achieved by this analysis is less than 10% and compatible to that of the SM theory.

The research covers following achievements:

- Confirmation of the presence of t-quark at the LHC
- Establishment of the method to identify $t\bar{t}$ events at the LHC pp collisions and to evaluate the background contamination
- The first precise measurement of the $t\bar{t}$ production rates in the dilepton final state at the 7 TeV collisions
- First detailed study of the $t\bar{t}$ production kinematic properties in the LHC which confirms the current particle physics Standard Model describes them well.

The methods developed and the studies performed for the $t\bar{t}$ cross-section measurement are applicable for other physics analyses using t-quark, e.g. a new physics search program with signatures of $t\bar{t} + E_T^{miss}$ or $t\bar{t}$+jets. The $t\bar{t}$ identification method established in the present work forms the basis for these physics programs. For analyses in which the $t\bar{t}$ production is a dominating background such as the supersymmetry search program, the $t\bar{t}$ background can be evaluated with reference to this experimental result, and it would improve their sensitivity.

Contents

Chapter 1

Introduction

Modern elementary particle physics is described by the quantum field theory where six leptons and six quarks are elementary particles, and gauge fields introduced by gauge-symmetry requirements in the gauge group $(SU(3)_C \otimes SU(2)_L \otimes U(1)_Y)$ produce interactions between the particles. This theory is so-called the "Standard Model Theory" of the particle physics (SM). Since any significant disagreement between results from collider experiments and the SM has not been reported yet as of 2011, theoretical and experimental studies for precise verifications of the theory and quests for new phenomena beyond the SM have been performed toward further developments of the particle physics. In particular, a precise measurement in the high energy frontier is one of the most important approaches since high energy particle collisions can probe new quantum effects, such as new heavy particle pair-productions. As of 2011, the Large Hadron Collider (LHC), which has been operated since 2009, is the energy frontier collider, where proton and proton collide at the center-of-mass energy $\sqrt{s} = 7$ TeV[*1]. This thesis discusses top-quark (t-quark) pair-production cross-section measurements at the $\sqrt{s} = 7$ TeV pp collisions, using data recorded by the ATLAS detector at the LHC.

The t-quark is an interesting object that can provide many interesting tests of the particle physics theory. It is the heaviest elementary particle of all known particles in the SM, and its mass has been measured to be 173.18 $\pm$ 0.56 (stat.) $\pm$ 0.76 (syst.)[*2] GeV at $p\bar{p}$ collisions with $\sqrt{s} = 1.96$ TeV at the Tevatron collider [5], which is the former energy frontier accelerator. Owing to its large mass, there are several theoretical models that predict new phenomena in the $t\bar{t}$ production and decay.

This research has led to the first precise measurement of the $t\bar{t}$ production cross-section at pp collisions with $\sqrt{s} = 7$ TeV as:

$$175 \pm 6 \text{ (stat.)} \, {}^{+14}_{-11} \text{ (syst.)} \pm 8 \text{ (lumi.) pb.}$$

The uncertainty of the measurement is limited to be less than 10% in total, with following achievements:

[*1] The center-of-mass energy, which is denoted as $\sqrt{s}$, is defined as invariant mass of the center-of-mass system of pp collisions. The four-momentum of circulating protons is $p_1 = (3.5 \text{ TeV}, 0, 0, 3.5 \text{ TeV})$, $p_2 = (3.5 \text{ TeV}, 0, 0, -3.5 \text{ TeV})$. The four-momentum of the center-of-mass system, which is $p_1 + p_2$, is $(7 \text{ TeV}, 0, 0, 0)$, and the $\sqrt{s} = 7$ TeV for the case of LHC, simply $\sqrt{s} = 2E_p$.

[*2] This is $\approx 340,000$ times larger than that of an electron.

- Understanding of the kinematic properties of the $t\bar{t}$ signal events and possible background candidates
- Optimization of the scheme to collect the $t\bar{t}$ samples from pp collision data
- Evaluation and calibration of the detector performances.

In particular, the LHC is not only the energy frontier accelerator but also the intensity frontier hadron collider owing to a high frequency of pp crossings and intensive proton beams. It is expected that multiple collisions occur per a bunch crossing in average, and they can affect the detector performances significantly. Therefore, the correct understanding of the detector performance in the LHC environment is indispensable prerequisite for the precise measurement. The optimized analysis for the experimental environment enables to identify more than 1,400 $t\bar{t}$ candidate events from pp collisions of 0.70 fb^{-1} with a high purity ($\approx 83\%$) in the dilepton final states that are characterized by a pair of two isolated leptons (electrons or muons). This $t\bar{t}$ samples extracted from collision data are used for the $t\bar{t}$ production cross-section measurement and the studies of kinematic properties of the t-quark pair-production.

Furthermore, I have been leading the commissioning of the ATLAS Level-1 muon trigger system. Since muon identification is the key component in distinguishing leptonic $t\bar{t}$ decays from many backgrounds in pp inelastic scattering, a superior performance of the muon trigger which was established by successful commissioning and calibrations is a significant contribution to the precise measurement. The timing adjustment of detector hit signals, which is the most important calibration of the coincidence trigger logic, was done with enough high precision ($\approx$ 1 ns) for the high and uniform trigger efficiency. Achievements in the muon trigger commissioning and operation are discussed as the second main topic of this thesis.

As reviewed above, this thesis contains the following discussions: In Chapter 2, the theoretical background related to $t\bar{t}$ production at pp collisions is summarized. In Chapter 3, the experimental apparatus of the LHC accelerator and the ATLAS detector are introduced. In Chapter 4, the achievements of the muon trigger commissioning are explained. In Chapter 5, the data analysis to measure the $t\bar{t}$ cross-section is explained, and comparisons with other $t\bar{t}$ cross-section measurements are presented.

Chapter 2

Theoretical background

The LHC is a proton-proton collider with $\sqrt{s} = 7$ TeV, and the $t\bar{t}$ production at pp collisions is described as the interaction between gluons and quarks which constitute protons. Figure 2.1 describes the $t\bar{t}$ production and the t-quark decay, which gives the total cross-section of $t\bar{t}$ production as follows:

$$\sigma_{t\bar{t}+X} = \int_0^1 dx_1 \int_0^1 dx_2 \sum_{ij} f_i(x_1, \mu_F) f_j(x_2, \mu_F) \hat{\sigma}_{ij \to t\bar{t}+X}(\hat{s}) \tag{2.1}$$

where i and j denote the initial state partons, and x_1 and x_2 are the proton momentum fraction carried by the parton i and j in the interaction $ij \to t\bar{t}+X$. $\hat{\sigma}_{ij \to t\bar{t}+X}(\hat{s})$, which is called partonic cross-section, denotes the cross-section of the $t\bar{t}$ production via interaction between parton i and parton j with the interaction energy of $\sqrt{\hat{s}}$[*1]. In the calculation of the total cross-section, the partonic cross-section is integrated with the appropriate weight according to the momentum distributions of the partons represented by f_i in Equation 2.1 as a function of the momentum fraction x and a factorization-scale parameter μ_F.

Since the t-quark is the only quark being heavier than W bosons[*2], it decays into immediately $t \to bW$ via the electroweak interaction[*3] (i.e. without complicating hadronization processes), and the branching fraction of $t \to bW$ is predicted to be 100% by the SM. Owing to the properties, the decay of t-quark is simple enough to predict by the SM theory with a small uncertainty. Therefore, measuring the $t\bar{t}$ production events in the LHC gives a good opportunity for a first precise test of the SM theory in high-energy pp collisions with $\sqrt{\hat{s}}$ that allows the $t\bar{t}$ production ($\sqrt{\hat{s}} > 2m_t$). Furthermore, many theoretical models that extend the SM expect that new phenomena are associated with the $t\bar{t}$ production, due to the large mass of the t-quark. Therefore, significant disagreement between the SM prediction and the measurements may be an important hint for the new phenomena.

In this chapter, the t-quark is introduced in Section 2.1, the $t\bar{t}$ production and decay process are discussed in Section 2.2 and Section 2.3, and the new phenomena which could be observed

[*1] The center of mass energy of the parton-parton collision system is evaluated to be $\sqrt{\hat{s}} = \sqrt{x_1 \cdot x_2} \cdot \sqrt{s} = \sqrt{x_1 \cdot x_2} \cdot 7$ TeV at the LHC pp collisions.

[*2] m_t and m_W have been measured to be 173.1 GeV and 80.4 GeV, respectively.

[*3] The decay-time constant of the t-quark $\tau_{t \to bW}$ is $\approx 10^{-25}$, while typical time-scale of hadronization τ_{QCD} is $\approx 10^{-23}$.

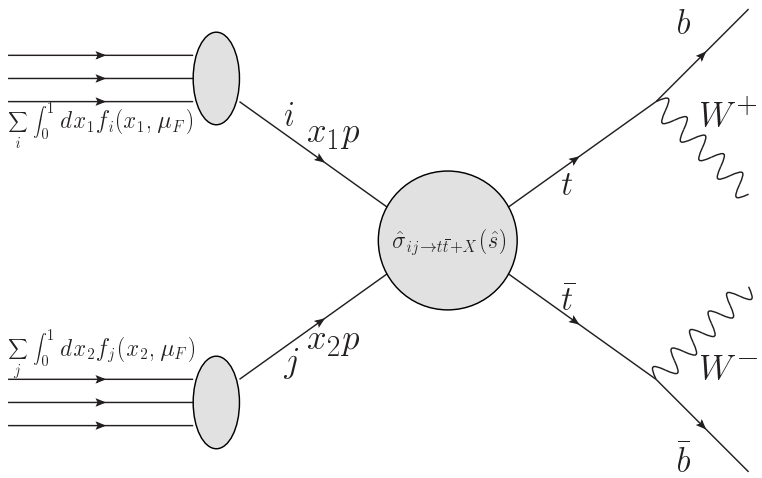

Figure 2.1: Diagram of the $t\bar{t}$ production and decay at the pp collisions.

in the $t\bar{t}$ production are mentioned in Section 2.4.

2.1 The Standard Model and the top-quark

The modern particle physics is described by the SM. The theory is based on the gauge symmetry assumption in $SU(3)_C \otimes SU(2)_L \otimes U(1)_Y$ group. The SM contains quarks, leptons, gauge bosons, and an additional scalar boson as summarized in Table 2.1, 2.2, and 2.3. All the particles have been observed in experiments except for the scalar boson. Quarks and leptons have spin quantum number equal to $\frac{1}{2}$. Therefore, they follow the Fermi statistics and constitute matters. The gauge bosons are introduced by the requirement of the gauge symmetry. They have spin quantum number equal to 1 and follow the Bose statistics. The gauge bosons carry forces and are called propagators of interactions. The only scalar boson is introduced to explain the mass of elementary particles via the mechanism of spontaneous symmetry breaking. It is called the Higgs boson.

The t-quark is classified as the third generation of the up-type quark, as shown in Table 2.1. The t-quark was discovered at $p\bar{p}$ collision experiments at the Tevatron accelerator, which is the former energy frontier experiment, in 1995 [3, 4]. Its mass has been measured to be 173.18 $\pm$ 0.56 (stat.) $\pm$ 0.76 (syst.) GeV there [5]. The LHC is a proton-proton (pp) collider with $\sqrt{s} = 7$ TeV, where the t-quark and anti t-quark pairs ($t\bar{t}$) are produced in the strong interaction of quark and anti-quark annihilation ($q\bar{q} \to t\bar{t}$) or gluon-gluon fusion ($gg \to t\bar{t}$) in the tree level approximation, as shown in Figure 2.2.

2.2 Prediction of the $t\bar{t}$ pair-production by Quantum Chromodynamics (QCD)

A $t\bar{t}$ is created by gluon-gluon fusion or quark and anti-quark annihilation via gluon exchange in the SM, and the corresponding partonic cross-section is evaluated by the perturbative technique

	1-generation	2-generation	3-generation	Spin	T_L^3	Q	$Q - T_L^3$
quark	$\begin{pmatrix} u_L \\ d_L \end{pmatrix}$	$\begin{pmatrix} c_L \\ s_L \end{pmatrix}$	$\begin{pmatrix} t_L \\ b_L \end{pmatrix}$	$\frac{1}{2}$	$\begin{pmatrix} +\frac{1}{2} \\ -\frac{1}{2} \end{pmatrix}$	$\begin{pmatrix} +\frac{2}{3} \\ -\frac{1}{3} \end{pmatrix}$	$+\frac{1}{6}$
	u_R	c_R	t_R	$\frac{1}{2}$	0	$+\frac{2}{3}$	$+\frac{2}{3}$
	d_R	s_R	b_R	$\frac{1}{2}$	0	$-\frac{1}{3}$	$-\frac{1}{3}$
lepton	$\begin{pmatrix} \nu_{eL} \\ e_L \end{pmatrix}$	$\begin{pmatrix} \nu_{\mu L} \\ \mu_L \end{pmatrix}$	$\begin{pmatrix} \nu_{\tau L} \\ \tau_L \end{pmatrix}$	$\frac{1}{2}$	$\begin{pmatrix} +\frac{1}{2} \\ -\frac{1}{2} \end{pmatrix}$	$\begin{pmatrix} 0 \\ -1 \end{pmatrix}$	$-\frac{1}{2}$
	e_R	μ_R	τ_R	$\frac{1}{2}$	0	-1	-1
	ν_{eR}	$\nu_{\mu R}$	$\nu_{\tau R}$	$\frac{1}{2}$	0	0	0

Table 2.1: Fermions in the SM. 6 quarks and 6 leptons are categorized into three generations according to their mass. Spin quantum numbers, third component of iso-spin(T_L^3), electronic charge(Q), and the $Q - T_L^3$ (corresponding to hyper charge (Y)) are summarized in the table. Up-type quarks have electric charge equal to $+\frac{2}{3}e$ and down-type quarks have electric charge equal to $-\frac{1}{3}e$, where e is elementary charge corresponding to the charge of electrons. Up-type leptons are electrically neutral and down-type leptons have electric charge of $-e$.

		Spin	T_L^3	Q	$Q - T_L^3$
gluon	G^μ	1	0	0	0
$W^\pm$	$\begin{pmatrix} W_\mu^+ \\ W_\mu^- \end{pmatrix} = \begin{pmatrix} \frac{W_\mu^1 + W_\mu^2}{\sqrt{2}} \\ \frac{W_\mu^1 - W_\mu^2}{\sqrt{2}} \end{pmatrix}$	1	$\begin{pmatrix} +1 \\ -1 \end{pmatrix}$	$\begin{pmatrix} +1 \\ -1 \end{pmatrix}$	0
Z^0	$Z_\mu = \cos\theta_W W_\mu^3 - \sin\theta_W B_\mu$	1	0	0	0
γ	$A_\mu = \sin\theta_W W_\mu^3 + \cos\theta_W B_\mu$	1	0	0	0

Table 2.2: Gauge bosons in the SM. All of them are introduced by assumption of gauge symmetry. They carry the strong force (gluon), weak force ($W^\pm, Z^0$), and electromagnetic force (γ). The $W^\pm$ has electronic charge of $\pm e$ and the others are electronically neutral. Only gravitation is not introduced in the SM theory, and not mentioned in the table.

		Spin	T_L^3	Q	$Q - T_L^3$
Higgs	$\phi = \begin{pmatrix} \phi^+ \\ \phi^0 \end{pmatrix}$	0	$\begin{pmatrix} +\frac{1}{2} \\ -\frac{1}{2} \end{pmatrix}$	$\begin{pmatrix} +1 \\ 0 \end{pmatrix}$	$\frac{1}{2}$

Table 2.3: The Higgs boson which is introduced to give the mass to the elementary particle with gauge symmetry in the SM. To give the mass to W, Z bosons, the Higgs field forms a doublet in $SU(2)_L \otimes U(1)_Y$.

in the QCD theory. In this section, the prediction of the $t\bar{t}$ production in QCD theory is summarized.

2.2.1 Running coupling constant

In the QCD calculation, the coupling constant, which is denoted by α_s, depends on the momentum transfer in the interactions (Q^2), where Q is equal to a total kinetic energy used to

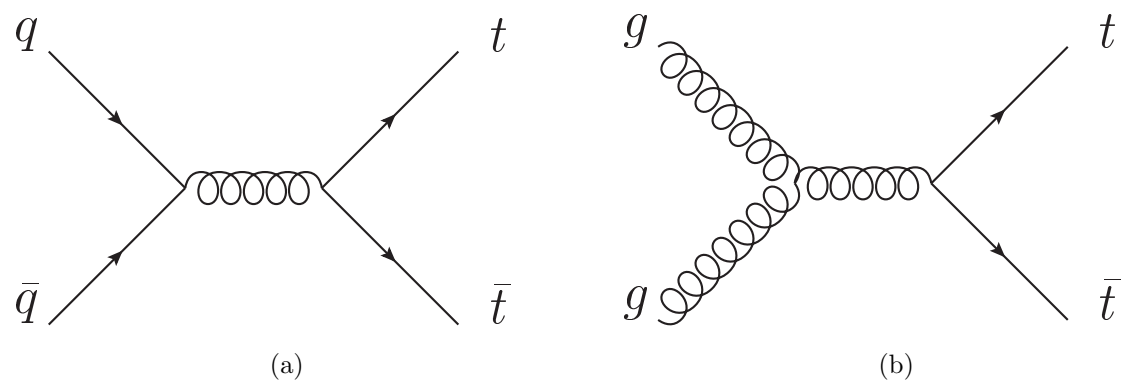

Figure 2.2: Two main $t\bar{t}$ production processes at the LHC are shown in the tree level Feynman diagram. (a) $q\bar{q}$ annihilation. (b) gg fusion.

create a t-quark pair in the event. The running coupling constant is described as a function of Q^2, as the following:

$$\alpha_s(Q^2) = \frac{1}{b_0 \ln \frac{Q^2}{\Lambda^2_{QCD}}}, \tag{2.2}$$

where:

$$b_0 = \frac{11N_C - 2n_f}{12\pi}, \tag{2.3}$$

where n_f is the number of quark flavors, the mass of which is lower than Q, and $N_C = 3$ stands for the number of quark colors. The $\alpha_s(Q^2)$ has been well measured by several measurements with several values of Q, as shown in Figure 2.3. The Q dependence of the α_s is predictable by the renormalization theory. Details are discussed in the Appendix A.1.

The momentum transfer Q is typically $> 2m_t$, and α_s is expected to be ≈ 0.1 in the $t\bar{t}$ production. The small α_s allow the perturbative technique to work to in the calculation of the $t\bar{t}$ cross-section, as discussed in the next section. A scale (μ_R) that is so-called "renormalization scale" is introduced in the renormalization to keep consistent dimension in the renormalization. The renormalization scale is chosen to be m_t and the fluctuation is evaluated with the interval of renormalization scale in $[\frac{m_t}{2}, 2m_t]$. The choice of the μ_R is arbitrary and a 4% level of uncertainties corresponding to it is expected in the theoretical $t\bar{t}$ cross-section calculation.

2.2.2 Perturbative QCD and partonic cross-section of the $t\bar{t}$ production

The $t\bar{t}$ production cross-section is evaluated by means of the perturbative QCD (p-QCD) calculations. Since the proton consists of uud quarks (the valence quarks), gluons, and $q\bar{q}$ (the sea quarks introduced via loop interactions), the process is described as interaction of these constituents, so-called "partons". The cross-section of the interaction between partons (partonic cross-section), which is denoted as $\hat{\sigma}_{ij\to t\bar{t}+X}(\hat{s})$ in Equation 2.1, is evaluated with the p-QCD technique.

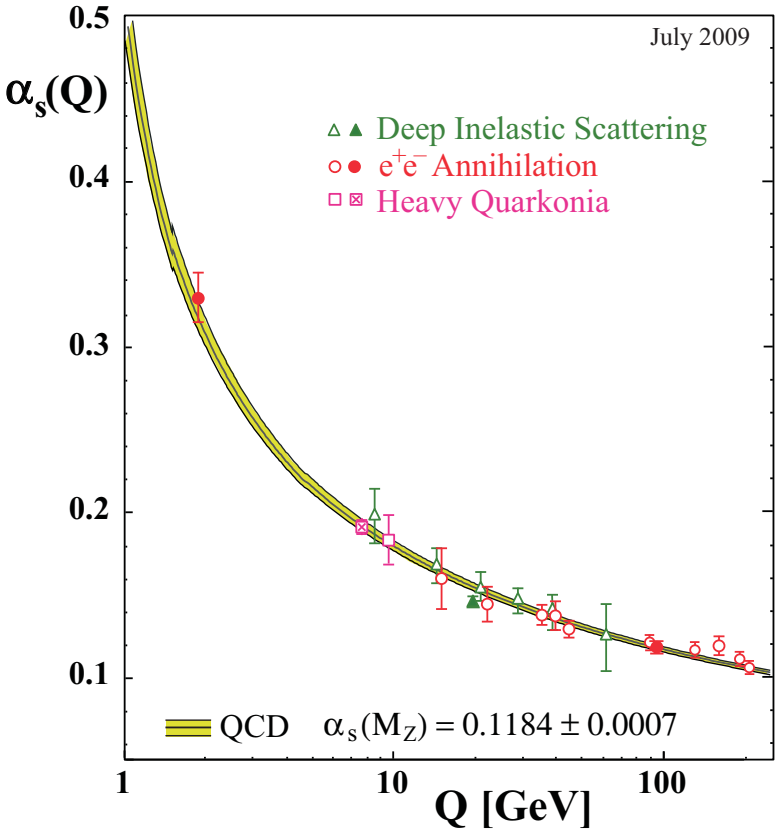

Figure 2.3: Summary of measurements of α_s as a function of the respective energy scale Q. The curves are QCD predictions for the combined world average value of $\alpha_s(M_{Z^0})$ [7]

.

In p-QCD, an observable $\hat{\sigma}_{ij\to t\bar{t}+X}(\hat{s})$ can be expanded as:

$$\hat{\sigma}_{ij\to t\bar{t}+X}(\hat{s}) = \sigma_1(\hat{s})\alpha_s + \sigma_2(\hat{s})\alpha_s^2 + \sigma_3(\hat{s})\alpha_s^3 + \dots . \tag{2.4}$$

Each order of the cross section can be calculated by the Feynman diagram technique. Figure 2.2 and Figure 2.4 show the diagrams of $t\bar{t}$ production in the lowest order and the second lowest order approximation, respectively, which are the leading-order (LO) and the next-leading-order (NLO) approximation. In this analysis, the theoretical prediction of the $t\bar{t}$ events is given by the LO+NLO approximation of the p-QCD.

2.2.3 The parton distribution function

The partonic cross-section for collisions of two partons with x_1 and x_2 is integrated in possible range of the momentum with the appropriate weight function, which is called the parton distribution function (PDF). It is denoted as f_i in Equation 2.1, where i denotes the flavor of the initial partons (u, d, c, s, g, and b), and the fraction of momentum carried by the partons in the interaction is given by x. For the different parton flavor, the PDF is very different[*4]. The

[*4]The PDF normalization and basic requirements are mentioned in the Appendix A.2.

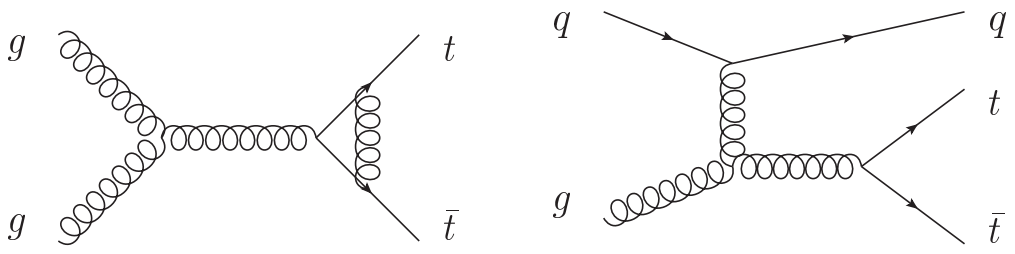

Figure 2.4: $t\bar{t}$ production Diagrams in next-to-leading order approximation (NLO).

PDF of the valence quarks have a peak at $x \approx 1/3$, while the gluon PDF is small at large x ($x > 0.1$) and grows rapidly for small x, which is roughly scaled by x^{-2}.

As a further application of the PDF, instead of including soft parton emissions in the initial state in the p-QCD calculation, such contributions with $k_T < \mu_F$ are taken into account in the parton distribution function in order to avoid a divergence for a low-p_T limit (so-called a collinear limit). The lower limit is called a factorization scale (μ_F), and thus far, the parton distribution function is modified into $f_i(x, \mu_F)$. The choice of μ_F is arbitrary and generally the momentum transfer $\approx Q$ is chosen for μ_F. Since the emitted soft gluons have the momentum less than Q, this means that all the initial state radiated soft gluons (ISR) are taken into account by parton distribution function (Figure 2.6(a)). For the calculation of $t\bar{t}$ cross-section, $\mu_F = m_t$ is selected. The evolution of $f_i(x, \mu_F)$ for μ_F is evaluated by the so-called DGLAP evolution equation [8] and the theoretical prediction is checked to be well consistent with the measurements [9]. The parton distribution function evaluated with input from both experiments and theories are shown in Figure 2.5.

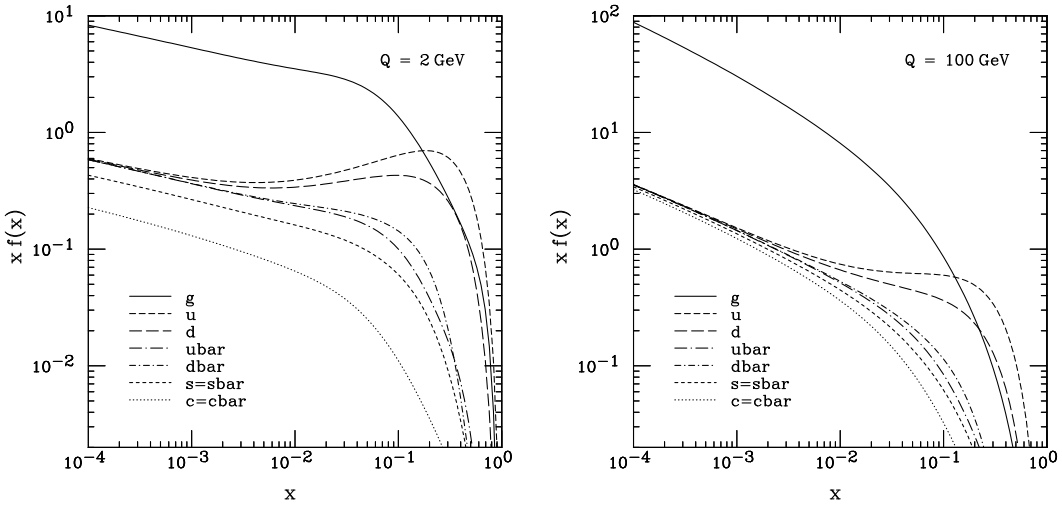

Figure 2.5: An example of parton distribution functions sets at $Q = 2$ GeV and 100 GeV (CTEQ6M) [9].

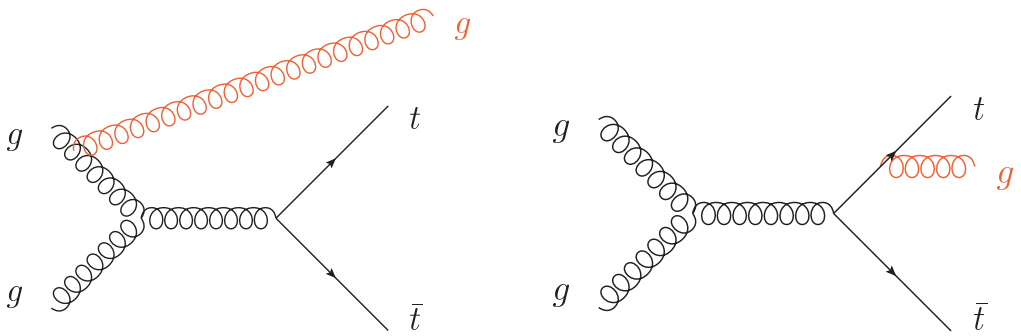

(a) (b)

Figure 2.6: Examples of (a) initial state radiation (ISR) and (b) final state radiation (FSR).

The (x, Q) and (x_1, x_2) of the $t\bar{t}$ production events at the LHC are shown in Figure 2.7. The $t\bar{t}$ production cross-section is proportional to the integral of the PDF in these parameter spaces, and the pure $t\bar{t}$ samples enable the validation of the PDF in the kinematic regions.

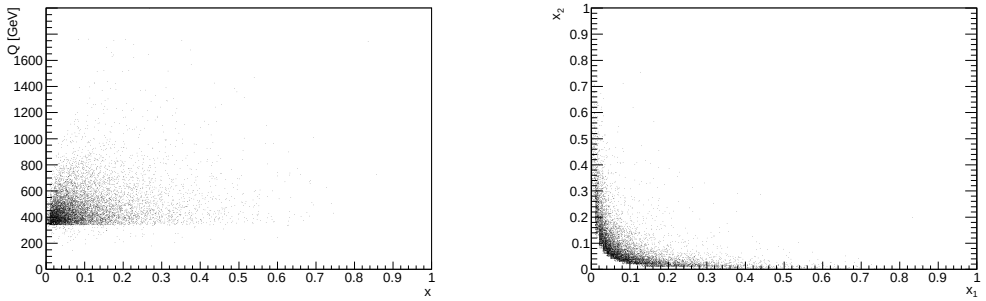

(a) (b)

Figure 2.7: The kinematic parameter region of (a) (x, Q) and (b) (x_1, x_2) that permit the $t\bar{t}$ production at the pp collisions with $\sqrt{s} = 7$ TeV. These figures are obtained in the $t\bar{t}$ event simulation given by the CTEQ6.6 [10] and the NLO $t\bar{t}$ event generator [11].

2.2.4 Total cross-section prediction within the SM

The $t\bar{t}$ production cross-section in 7 TeV pp collisions is estimated by the p-QCD calculation and the given parton distribution functions (CTEQ66 [10]). With the assumption that the t-quark mass is 172.5 GeV, the $t\bar{t}$ production cross-section is evaluated to be:

$$\sigma_{t\bar{t}}^{\mathrm{SM}} = 164.57\ ^{+4.30}_{-9.27}(\mathrm{scales})\ ^{+7.15}_{-6.51}(\mathrm{PDF})\ \mathrm{pb}, \tag{2.5}$$

where the first uncertainty corresponds to an uncertainty originating from the renormalization and factorization scales ($\approx 4\%$), and the second one corresponds an uncertainty from the PDF parametrization ($\approx 4\%$) [6]. Additionally the predictions for various assumptions of the t-quark mass are summarized in the Appendix Figure A.1.

2.3 Prediction of the final states of $t\bar{t}$ events

2.3.1 Decay of the top-quark

The t-quarks decay immediately into bW since the t-quark is very heavy ($m_t \approx 2 \times m_W$). The partial width of the decay via electroweak interaction $t \to Wb$ is estimated to be 2 GeV by the following equation in the LO approximation:

$$\Gamma_t = \frac{G_F m_t^3}{8\pi\sqrt{2}} |V_{tb}|^2, \tag{2.6}$$

which depends on the t-quark mass, the Fermi coupling constant G_F, and the strength of the left-handed Wtb coupling V_{tb} in the CKM matrix. The width corresponds to a lifetime of $\tau \sim 10^{-25}$ sec, which is much smaller than the typical hadronization time scale $\tau_{QCD} \approx 10^{-23}$ sec. Therefore, the t-quark decays via electroweak interaction before the hadronization.

The t- and b-quarks form a weak iso-spin doublet and the transition from the t-quark into other generation quarks (i.e. d-quark or s-quark) is suppressed by the CKM matrix in the decay. The suppression factors are $|V_{ts}|^2/|V_{tb}|^2 \approx (\sin\theta_C)^4$ for a transition to s-quark, and $|V_{tu}|^2/|V_{tb}|^2 \approx (\sin\theta_C)^6$ for a transition to d-quark, where the θ_C is the Cabibbo angle, and $\sin\theta_C \approx 0.23$. Therefore, the t-quark is considered to decay into bW 100% of the times in the SM.

Owing to these properties of t-quark decays, the decay of the t-quark is simple enough to perform precise tests of the SM and the new phenomena with the t-quarks.

2.3.2 Decay of the W boson

W bosons decay into $W \to e\nu$, $W \to \mu\nu$, $W \to \tau\nu$, $W \to ud'$, and $W \to cs'$, while $W \to tb'$ is not allowed kinematically. The s' and d' stand for the weak interaction eigenstates which are by a linear combination of the mass eigenstates described with the CKM U_{CKM} matrix as:

$$\begin{bmatrix} d' \\ s' \\ b' \end{bmatrix} = U_{CKM} \begin{bmatrix} d \\ s \\ b \end{bmatrix}. \tag{2.7}$$

The coupling strength for the W gauge boson is proportional to the magnitude of the weak iso-spin, and all the left-handed fermions have the quantum number of weak-isospin 1/2. Then the branching fraction of W boson is predicted to be uniform for the following 9 final states:

$$\begin{pmatrix} e \\ \nu_e \end{pmatrix}_L, \begin{pmatrix} \mu \\ \nu_\mu \end{pmatrix}_L, \begin{pmatrix} \tau \\ \nu_\tau \end{pmatrix}_L, \begin{pmatrix} u \\ d' \end{pmatrix}_{LR}, \begin{pmatrix} c \\ s' \end{pmatrix}_{LR}, \begin{pmatrix} u \\ d' \end{pmatrix}_{LG}, \begin{pmatrix} c \\ s' \end{pmatrix}_{LG}, \begin{pmatrix} u \\ d' \end{pmatrix}_{LB}, \begin{pmatrix} c \\ s' \end{pmatrix}_{LB}. \tag{2.8}$$

The index L stands for the left-handed chirality of the field, and R, G, and B stand for colors only for quark doublets. The branching fraction for each final state is evaluated to be $\approx 1/9$.

2.3.3 Parton shower simulation

Soft parton emissions in final states should be described to predict completely the final state of $t\bar{t}$ events produced by the LHC, while the p-QCD suffers from the infrared divergence. While the divergence is avoided by an application of the PDF in the initial state (see Section 2.2.3), a theoretical technique called parton shower simulator is used to avoid the problem. The DGRAP evolution equation [8] can calculate probabilities that a parton decays into two partons with a LO approximation. The parton shower simulation uses the results given by the DGRAP evoluation equation, and a non-splitting probability of the parton decaying into any parton above k_T in the energy scale Q is introduced approximately as:

$$P(\text{no emission above } k_t) \equiv \Delta(k_t, Q) \approx \exp\left(-\frac{8\alpha_s}{3\pi}\int^{Q}\frac{dE}{E}\int\frac{d\theta}{\theta}\Theta(E\theta - k_t)\right), \qquad (2.9)$$

where the θ is the angle of emitted partons, and $\Theta(a)$ is a step function defined as 1 for $a > 0$ and 0 for $a < 0$. A random number is taken with $0 < r < 1$ from a uniform distribution in the simulation. A value of k_{T1} which solves $\Delta(k_{T1}, Q) = r$ is found for the given r. The given k_{T1} is treated as the virtuality of the (first) emitted parton in the simulation. The same procedure is repeated and next k_{T2} is found, with the constraint that k_{T2} is less than k_{T1}. This corresponds to the virtuality of the second emitted parton. This procedure is repeated until the scale k_{Ti} becomes less than the cut-off scale Q_0, which is a parameter tuned with respect to the experimental results. Currently the Q_0 is tuned with the charged particle multiplicity measurements at LEP.

2.3.4 Hadronization simulation

The b-quarks from the t-quark decays, the $q\bar{q}'$ from W decays, and other radiated gluons and quarks hadronize and are detected as a group of hadrons (hadron jets) in the detector. The hadronization process is calculated with several models in simulations. A widely used model involves stretching a color 'string' across quarks and gluons and breaking them up into hadrons, which represents the QCD strong potential. This model involves a number of non-perturbative parameters, which are tuned with respect to the experimental results.

The parton shower simulation and the hadronization simulation, which is introduced in the next section, gives the complete description of the hadrons in the final state. The parameter tuning can be validated in the $t\bar{t}$ production events in the LHC by focusing on the final state gluon radiation (FSR) (Figure 2.6(b)).

2.3.5 Event topologies of $t\bar{t}$ production

Since the t-quark decays into bW 100% of the time within the SM, the event topologies of the $t\bar{t}$ production are determined by the decay products of the two W bosons. Taking the combination of the two W bosons' final states, the $t\bar{t}$ final state is categorized, as shown in Figure 2.8.

Experimentally we can identify electrons, muons, τ leptons decaying into hadrons, and hadron jets. Therefore, the final states are classified into "all jets", "lepton+jets", "di-lepton", "lepton+hadronic τ", and "hadronic τ+jets". The branching fractions are $\approx 45\%$, $\approx 35\%$, 7%, 4%, and 9%, respectively, where "lepton" denotes electron or muon.

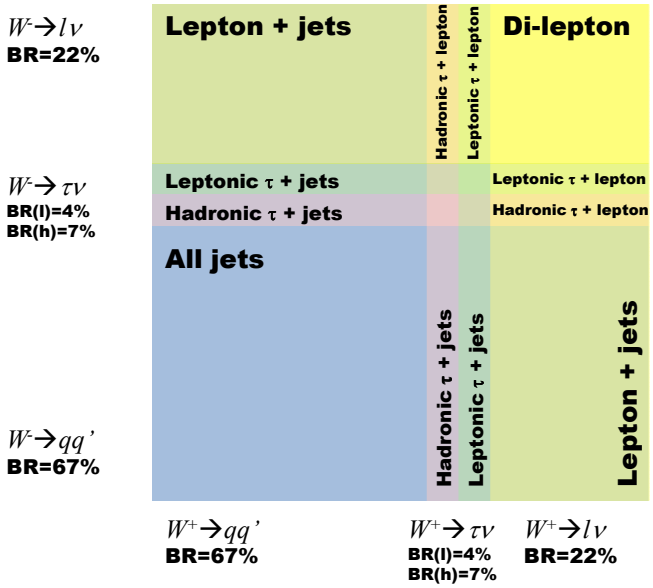

Figure 2.8: $t\bar{t}$ decay topologies are categorized with the decay products of two W bosons from $t \to bW$ decays.

The analysis presented in this thesis makes use of the dilepton final states. The dilepton channel has a clear signature characterized by two isolated high p_T lepton signals, and therefore, background candidates are well suppressed and controllable in the signal extraction. The final state consists of ee, $\mu\mu$, and $e\mu$ final states, the branching fraction of which is $\approx 7\%$. Even with this small branching fraction, more than 6,000 pairs of $t\bar{t}$ dilepton events are expected to be created in the given data sample of 0.70 fb^{-1} (see Section 5.2). Thus we can obtain enough amount of events to evaluate the $t\bar{t}$ cross-section in the dilepton final states.

2.4 New phenomena possible to be observed in the $t\bar{t}$ production

This section explains two possible phenomena that can modify the $t\bar{t}$ production property predicted by the SM, and motivate the precise measurements of the cross-section of $t\bar{t}$ production. Since the mass of the t-quark is large and about 170 GeV, the $t\bar{t}$ production process may be a probe for new phenomena such as the Higgs production and the supersymmetry particle production, both of which are motivated by the strong coupling between the t-quarks and the Higgs bosons. Section 2.4.1 gives an introduction of the Higgs production process associated with the $t\bar{t}$ events, and Section 2.4.2 explains pair-production of the t-quark partners, which has spin 0 (scalar t-quark), as a candidate of the possible extension of the SM.

2.4.1 The Higgs boson production associated with the $t\bar{t}$ production

Spontaneous symmetry breaking and the Higgs field

The Higgs field is a scalar field introduced to give the mass to all the gauge bosons by the mechanism of spontaneous gauge symmetry breaking, the details of which are discussed in Appendix A.4. Interactions between the Higgs boson and the SM fermions are also introduced as gauge invariant terms. This interaction, when the gauge symmetry is broken, produces the mass terms of the fermions. The coupling constants to the fermions are expected to be proportional to the mass of the fermions. The corresponding part of Lagrangian representing the third generation of quarks and leptons is given as:

$$\mathcal{L}_{\text{Yukawa}} = -\frac{1}{\sqrt{2}}(v+H)(Y_b\bar{b}b + Y_t\bar{t}t + Y_\tau\bar{\tau}\tau), \tag{2.10}$$

where coupling constants Y_b, Y_t, and Y_τ give origin of mass of the fermions. The mass is proportional to the coupling constants and the vacuum expectation value of the Higgs field ($v = 246$ GeV, see Appendix A.4). For example, mass is given for the third generation elementary particles as follows:

$$m_b = Y_b\frac{v}{\sqrt{2}} \tag{2.11}$$

$$m_t = Y_t\frac{v}{\sqrt{2}} \tag{2.12}$$

$$m_\tau = Y_\tau\frac{v}{\sqrt{2}}. \tag{2.13}$$

The coupling constants are unique to all the fermions according to their mass. What is especially important is that this results in the coupling constant of the t-quarks being the largest. The Y_t is ≈ 1.0 while coupling constants for the other fermions are less than 0.1, as shown in Figure 2.9. The largest Y_t can be measured experimentally in the $t\bar{t}$ production events, as discussed in the following section, which may be a significant hint to understand the mechanism of the symmetry breaking and develop the particle physics. Furthermore, the unnaturally large coupling constant between the t-quark and the Higgs boson motivate the correct understanding of t-quark from both experimental and theoretical approaches.

Higgs boson production associated with the $t\bar{t}$ production

In understanding the origin of the mass of elementary particles and the spontaneous gauge symmetry breaking, once the Higgs bosons are discovered, it is the most interesting to measure the coupling constants of the Higgs bosons to fermions. The linearity of the coupling constants according to the fermion mass is a good indication of the SM Higgs bosons. It can be a signature for physics beyond the SM if the coupling constants abandon the linear correlation. The largest Y_t contributes the Higgs boson production processes without higher loop correction, one of which is shown in Figure 2.10(a). It is called $t\bar{t}H$ production. The cross-section of $t\bar{t}H$ production is predicted to be proportional to the coupling constant Y_t and can be measured in $t\bar{t}$ samples. The cross-section is evaluated to be ≈ 0.1 pb, depending on the mass of the Higgs

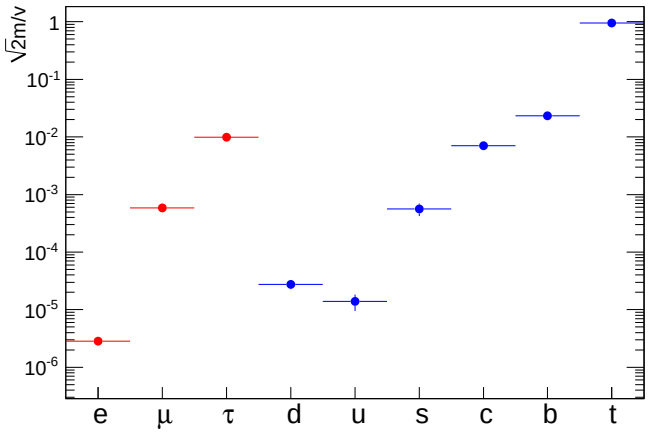

Figure 2.9: Expected coupling constant of fermions proportional to the fermion mass, expressed by $\frac{\sqrt{2}m_f}{v}$. The red points show the coupling for charged leptons and the blue points show the coupling for quarks.

boson, as shown in Figure 2.10(b). This process is very interesting in order to understand the coupling constant between the Higgs bosons and t-quark. For this purpose, it is important to understand the nominal $t\bar{t}$ production cross-section and its property at the LHC pp collisions without the production of the Higgs bosons. Especially it is essential to control the additional jets (e.g. ISR jets) well in the $t\bar{t}$ events so that we could handle the $H \to b\bar{b}$ decay signal associated with the $t\bar{t}$ events.

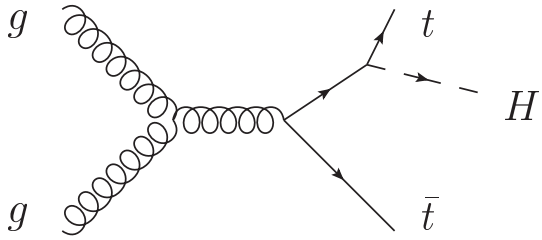

(a)

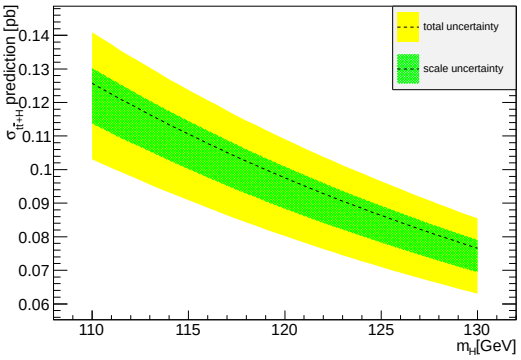

(b)

Figure 2.10: (a) An example of a $t\bar{t}H$ production diagrams. (b) Expected cross-section of $t\bar{t}H$ production with the PDF and scale uncertainties. It is typically $\sigma_{t\bar{t}+H} = 0.1$ pb and $\approx 10^{-3} \times \sigma_{t\bar{t}+X}$.

2.4.2 Production of the scalar partner of the top-quark

The hierarchy problem

Although the SM cannot predict the Higgs Boson mass, the possible range of the mass is limited by the experimental results. A Higgs mass smaller than 114.4 GeV is excluded according to the direct measurement at the LEP2 experiments at 95% confidence level [12], and the range from 125 GeV to 600 GeV is also excluded by the LHC experiments in 2011 [13, 14]. The SM prefers that the Higgs mass is light and an indirect upper bound of 158 GeV is set according to the precision measurements of electroweak parameters [15].

The Higgs boson couples to gauge bosons, fermions, and the Higgs boson itself in the SM. The coupling corrects the Higgs mass by the loop of these particles. The correction, which is shown in Figure 2.11, is proportional to the mass of the particle, as shown in Equation 2.14 and 2.15.

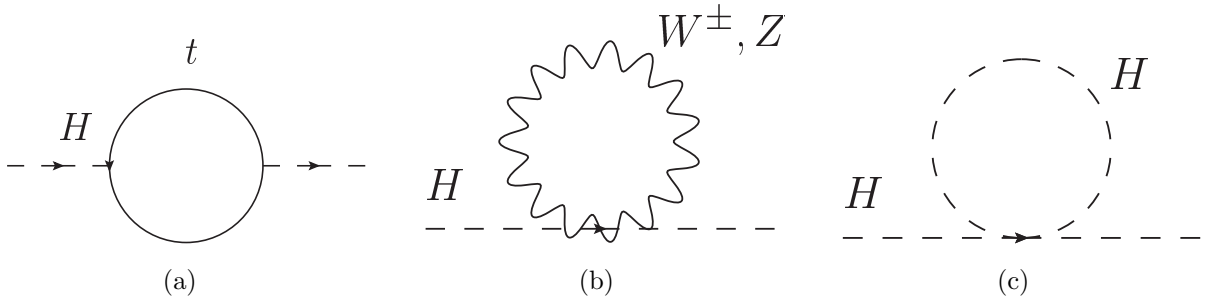

Figure 2.11: The three main contributions to the Higgs mass correction. These contributions give the quadratic divergence in the Higgs mass.

The SM Lagrangian gives the Higgs mass correction like:

$$\begin{aligned} m_H^2 &= (m_H^2)_0 + \delta m_H^2 \\ &= (m_H^2)_0 + \frac{3\Lambda^2}{64\pi^2}(-8y_t^2 + 3g^2 + g'^2 + 8\lambda + \dots), \end{aligned} \tag{2.14}$$

where Λ is the cut-off momentum scale up to which the SM is valid and the integral is performed, and $(m_H)_0$ is the bare Higgs mass. Considering $m_H^2 = 2\lambda v^2$, $m_t^2 = \frac{y_t^2 v^2}{2}$, $m_W^2 = \frac{g^2 v^2}{4}$, and $m_Z^2 = \frac{(g^2+g'^2)v^2}{4}$, as discussed in Appendix A.4, the given correction of the Higgs mass is expressed by the following function of the mass of the particles:

$$\delta m_H^2 = \frac{3\Lambda^2}{16\pi^2 v^2}(-4m_t^2 + 2m_W^2 + m_Z^2 + m_H^2 + \dots). \tag{2.15}$$

If the Λ is at the Planck mass scale, which means the SM is valid up to Planck mass scale ($M_{\text{Planck}} \approx \mathcal{O}(10^{19})$ GeV), the correction of the Higgs mass, δm_H, is assumed to be $\mathcal{O}(10^{18})$ GeV. This is much higher than the expected mass scale of the Higgs boson ($\mathcal{O}(100)$ GeV). It is required to be the bare Higgs mass and the correction is finely tuned, to generate the physical Higgs mass of $\mathcal{O}(100)$ GeV. This is called the "fine tuning problem" or "hierarchy problem" of the Higgs mass.

To solve the unnatural cancellation between δm_H and $(m_H)_0$, we introduce the partner to each SM particle which introduces a new loop diagram with an opposite sign which cancels the contribution. It, thus, makes the Higgs mass at $\mathcal{O}(100)$ GeV naturally. To achieve this, the t-quark should have a partner with similar mass, below 1 TeV.

The $\tilde{t}\bar{\tilde{t}}$ production with similar event topology to $t\bar{t}$ production

The t-quark partners may be created at the LHC pp collisions if their mass is below 1 TeV. The same event topology of the new t-quark partner can be the same as that of the SM $t\bar{t}$ events. In the supersymmetric models with R-parity conservation[*5], the t-quark partner is a scalar t quark ($\tilde{t}$) and the $\tilde{t}\bar{\tilde{t}}$ production is expected at pp collisions [16]. As well as the requirement for presence of a light partner of t-quark to solve the hierarchy problem, this supersymmetric model prefers a light t-quark partner as a result of the mixing between right-handed and left-handed scalar partners ($\tilde{t}_R, \tilde{t}_L$), effect of which is proportional to the t-quark mass [17]. The prediction of the light t-quark would motivate the $\tilde{t}$ at the LHC.

In a scenario where the lightest supersymmetric particle (LSP) is a neutralino (χ_0) or a gravitino ($\tilde{G}$), which are unlikely to have interactions with the normal matters, and the $\tilde{t}$ is the next lightest supersymmetric particle, a $\tilde{t}$ decaying into LSP particle and the t-quark, as shown in Figure 2.12, is one of the most probable processes.

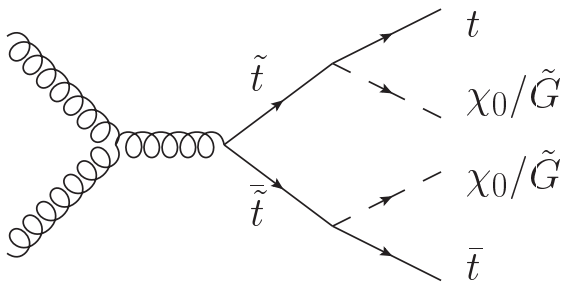

Figure 2.12: An example of the possible extension of the SM by the introduction of supersymmetry.

In the assumption that the mass of scalar partner of t-quark is below 1 TeV, this production process can be accessible at the LHC collision energy and can modify the $t\bar{t}$ production cross-section predicted by the QCD theory. The event topology is very similar to that of the $t\bar{t}$ production events except for the additional presence of the LSP particles, which may modify the kinematic distribution of the $t\bar{t}$ events, especially the E_T^{miss} distribution. These new phenomena can be observed in the comparison of the measured cross-section and kinematic distribution with the QCD prediction, which is one of the important motivations for the measurements of the $t\bar{t}$ production cross-section at the LHC.

[*5]R-parity is defined as: $P_R \equiv (-1)^{2s+2B+L}$, where the s, B, and L stands for spin, baryon number and lepton number. The SM particles have the R-parity of 1 while the supersymmetric new particles have those of -1.

Chapter 3

LHC-ATLAS experiment

In this section, the apparatus used in the analysis is explained. The LHC accelerator and the ATLAS detector are introduced in the following sections.

3.1 LHC accelerator

The LHC accelerator [2] is designed as a proton-proton collider with its center-of-mass energy of $\sqrt{s} = 14$ TeV with high instantaneous luminosity of 10^{34} cm^{-2} s^{-1}. This performance can be achieved with an injector complex and the following 27 km LHC main ring as summarized in Figure 3.1.

The injector system consists of a series of accelerators: the Linac2, the Proton Synchrotron Booster (PSB), the Proton Synchrotron (PS) and the Super Proton Synchrotron (SPS), which boost the protons from 50 MeV (after Linac2) to 450 GeV. The LHC following the injectors is designed so that the protons are accelerated from injection energy up to a maximum of 7 TeV by oscillating radio-frequency (RF) electric fields[*1]. In the LHC main ring, superconducting coils are operated in superfluid helium at 1.9 K in order to generate 8.33 Tesla to bend the 7 TeV proton-beams[*2]. The proton-beams cross in the experiments and provide the pp collisions with $\sqrt{s} = 14$ TeV.

For achieving the high luminosity, the LHC controls the beam trajectory and its spot size, and the proton bunches collide with very high frequency (40.08 MHz). The cross-section of the proton beams are focused in each of crossing points, and at the ATLAS to be $\sigma_x \times \sigma_y = 16.6\ \mu\text{m} \times 16.6\ \mu\text{m}$. These tuned machine parameters contribute the high luminosity, as discussed in the Appendix B.1.

The operation parameters are summarized in Table 3.1, comparing design parameters and those of the 2011 data taking. As of August 2011, the collision energy of 7 TeV and the instantaneous luminosity of the 1.5×10^{33} cm^{-2} s^{-1} have already been obtained in the LHC with the given parameters [*3]. The analysis presented in this thesis is done with data taken in

[*1] The radio-frequency is delivered to all the system, not only to the accelerator apparatus but also to the detector systems, so that the operation coherent to the LHC operation is achieved.

[*2] The LHC consists of eight 2.45km-long arcs, and the 1232 bending magnet is aligned along the LHC beam line.

[*3] The LHC is the highest energy and the most intensive hadron-hadron collider in the world.

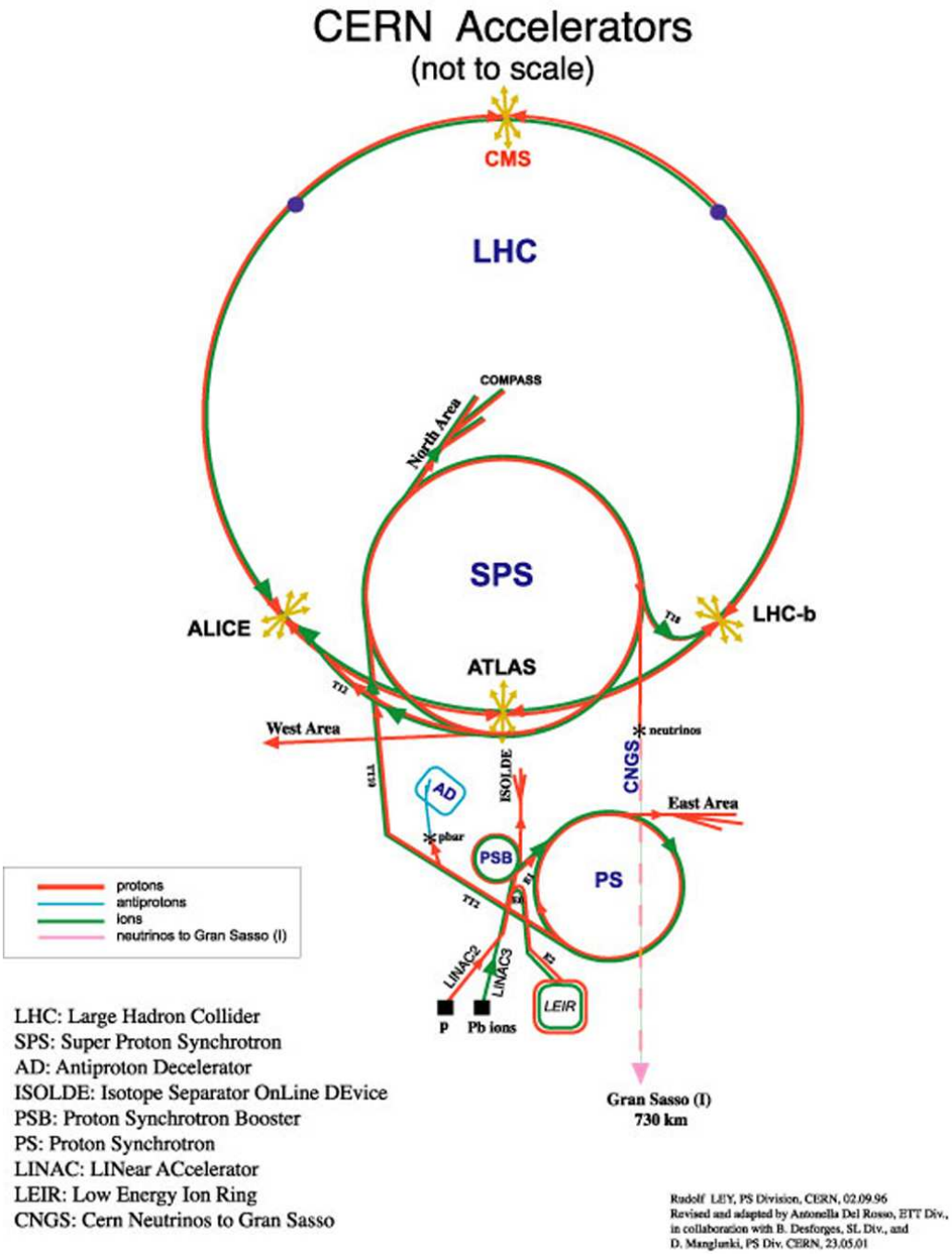

Figure 3.1: The LHC accelerator complex. Protons are accelerated up to 7 TeV in the maximum cases. Four interaction points are in the ring, where the ATLAS, the ALICE, the CMS, and the LHC-b detectors are located respectively.

such machine operation parameters as summarized in the table. The machine parameters are being tuned and they are expected to meet the superior parameters of the collision energy and

the luminosity, as designed.

	Design	2011 (August, 5th)
Length of the rings	26.7 km	-
Number of superconducting dipoles	1232	-
Magnetic field of dipoles	8.33 Tesla	4.16 Tesla
Current	11.85 kA	5.93 kA
Beam energy	7 TeV	3.5 TeV
Luminosity	10^{34} cm^{-2} s^{-1}	1.5×10^{33} cm^{-2} s^{-1}
Number of bunches (N_b)	2808	1318
Number of protons per bunch (n_p)	1.15×10^{11}	1.15×10^{11}
Time between collisions	25 ns	50 ns
Beam radius at IP ($\sigma_{x,y}$)	16.6 μm	$\approx 22\mu$m
Beam length (σ_z)	7.55 mm	≈ 6 mm
Full crossing angle (θ_c)	≈ 0.3 μrad	≈ 0.24 μrad

Table 3.1: LHC beam parameters

During the data taking, the luminosity of the pp collisions at the ATLAS detector is monitored by counting interaction rates with forward detectors [18]. The details of the evaluation are discussed in Appendix B.2.

3.2 ATLAS detector

3.2.1 Overview and coordinate system

The ATLAS detector [1] is a general-purpose detector located 80 m below the ground at one of the pp crossing points of the LHC. It covers almost the whole solid angle around the collision point with layers of tracking detectors, calorimeters, and muon chambers. Figure 3.2 illustrates the ATLAS detector. It has been designed to study a wide range of interest of the Standard Model and the new physics at the LHC energy. The ATLAS detector performs identification of the final state objects such as electrons, photons, muons, hadron-jets, hadronically decaying τ leptons, and b-jets, as well as measurements of energy of each object. Additionally by summing all the calorimeter transverse energy vectorically, the unbalance of detected transverse energy flow is calculated as a signature of a high p_T neutrino, so called missing transverse momentum (E_T^{miss}). The measurements of the $t\bar{t}$ production cross-section make use of electrons, muons, jets, and E_T^{miss} reconstructed with the ATLAS detector.

In the right-handed ATLAS coordinate system, the z coordinate is defined along the beam axis, where the positive direction of the z-axis is defined as the counter clockwise of the LHC ring, and the x coordinate is defined as the horizontal axis pointing towards the center of the LHC ring and the y coordinate is defined as the vertical axis pointing up. In the system pseudo-rapidity $|\eta|$ is defined as $\eta = -\ln(\tan(\theta/2))$, where the polar angle θ is defined with respect to the z-axis. The azimuthal angle ϕ is defined with respect to the x-axis. Transverse momentum and energy are defined as $p_T = p\sin\theta$ and $E_T = E\sin\theta$, respectively. In the analysis, distance between objects are evaluated in the η-ϕ plane with $\Delta R \equiv \sqrt{\Delta\eta^2 + \Delta\phi^2}$.

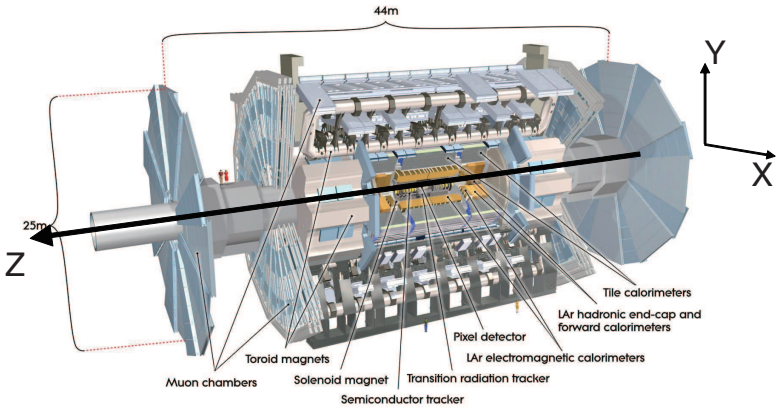

Figure 3.2: The ATLAS detector consists of tracking detectors, calorimeters, and the muon chambers. It is 25 m in height and 44 m in length. The overall weight of the detector is approximately 7000 tons.

Components	Resolution	η coverage	
		Measurements	Trigger
Tracking	$\sigma_{p_T}/p_T = 0.05\% p_T \oplus 1\%$	$\|\eta\| < 2.5$	-
EM calorimetry	$\sigma_E/E = 10\%/\sqrt{E} \oplus 0.7\%$	$\|\eta\| < 3.2$	$\|\eta\| < 2.5$
Hadron calorimetry			
barrel and end-cap	$\sigma_E/E = 50\%/\sqrt{E} \oplus 3\%$	$\|\eta\| < 3.2$	
forward	$\sigma_E/E = 100\%/\sqrt{E} \oplus 10\%$	$3.1 < \|\eta\| < 4.9$	
Muon spectrometer	$\sigma_{p_T}/p_T = 10\%$ at p_T=1 TeV	$\|\eta\| < 2.7$	$\|\eta\| < 2.4$

Table 3.2: Main components of the ATLAS detector.

3.2.2 Tracking

The innermost part of the ATLAS detector is a precise tracking system, so-called the inner detector (ID) system. The ID system surrounds the interaction point of pp collisions. The ID system consists of three independent tracking systems and 2 T magnetic field generated by the central solenoid extending over a length of 5.3 m with a diameter of 2.5 m. This enables to measure the momentum and charge of charged particles. The layout of the ID system is illustrated in Figure 3.3, silicon pixel trackers (Pixel), silicon micro-strip trackers (SCT), and straw tubes of the transition radiation trackers (TRT) are located in order of outgoing. The coverage of these sub-detectors is summarized in Table 3.3 and Figure 3.4.

The silicon pixel tracker (Pixel)

The Pixel detector system consists of semiconducting silicon sensors with the pixel size 50×400 μm^2 with their thickness of 250 μm. Its innermost layer is located at the radius of 51 mm from the beam pipe. The Pixel detector performs space point measurements of charged particle with good resolution even with high luminosity condition owing to the small pixel size of the

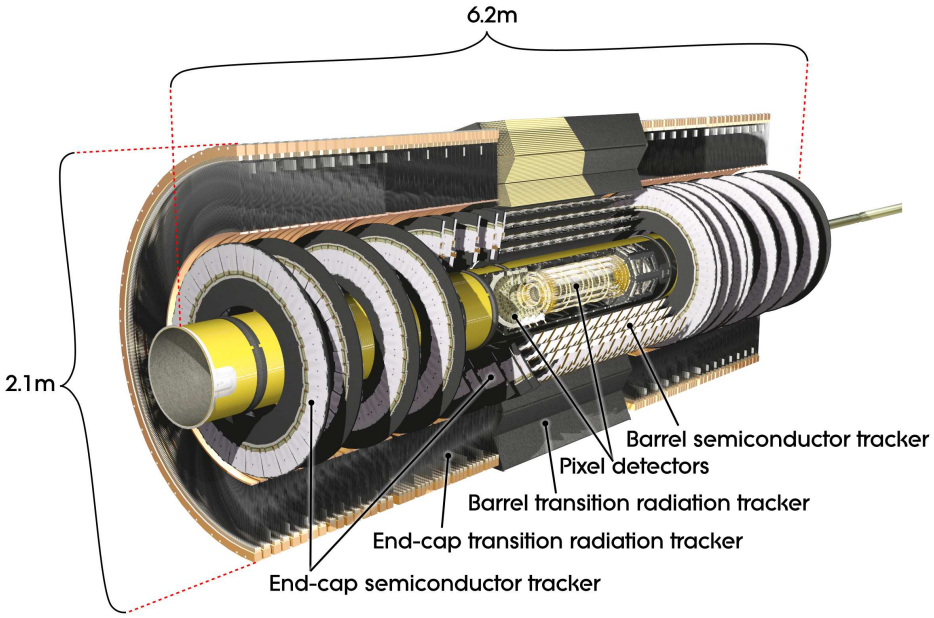

Figure 3.3: The inner detector system of the ATLAS detector.

		Radial extension (R mm)	Length(z mm)
Pixel			
3 cylindrical layers	barrel	$45.5 < R < 242$	$0 < \|z\| < 3092$
2×3 disks	end-caps	$88.8 < R < 149.6$	$495 < \|z\| < 460$
SCT			
4 cylindrical layers	barrel	$299 < R < 514$	$0 < \|z\| < 749$
2×9 disks	end-caps	$275 < R < 560$	$839 < \|z\| < 2735$
TRT			
73 straw planes	barrel	$563 < R < 1066$	$0 < \|z\| < 712$
160 straw planes	end-caps	$644 < R < 1004$	$848 < \|z\| < 2710$

Table 3.3: Table will be here summarizing ID coverage.

sensors. The sensors are operated with a bias voltage of 150 V, and more than 99% hit efficiency is expected in the operation. To complete the large acceptance, the system consists of two parts: 3 cylindrical layers (barrel module) and 3 disks standing vertical to the beam line (end-cap module), as shown in Figure 3.4. In the barrel, the pixel is aligned in order to measure the space points in the z coordinate and in the ϕ azimuthal direction. The intrinsic spacial resolution is 10 μm for the ϕ and 115 μm for z. In the end-cap, it is located to measure ϕ and $R \equiv \sqrt{x^2 + y^2}$. The resolution is 10 μm for ϕ and 115 μm for R. The total number of readout channels in the pixel is approximately 80.4 million.

The silicon micro-strip trackers (SCT)

The SCT detector system consists of semiconducting silicon strip sensors with their thickness of 285 μm. The mean strip pitch is approximately 80 μm and the length is 6.4 cm. They

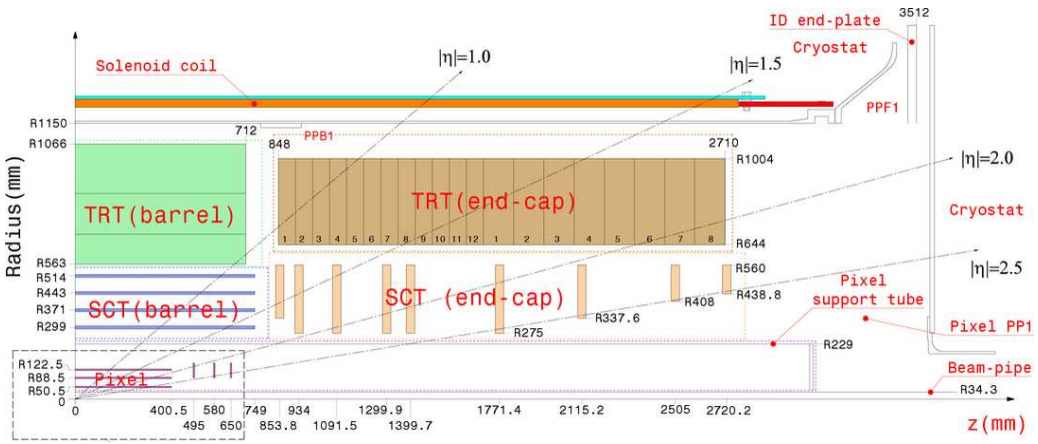

Figure 3.4: R-z cross-section view of the ATLAS inner detectors.

are operated with a bias voltage of 150 V and the hit efficiency is expected to be above 99%. The unit of the SCT module consists of two layers of the strips which have a stereo angle of 40 mrad in order to determine space points of passing charged particles by combining hits on the two layers. The SCT system surrounds the Pixel system with 4 barrel cylindrical layers and 9 end-cap disks, as shown in Figure 3.4, so that a charged track crosses eight strip layers (corresponding to four space points). The intrinsic accuracy is 17 μm (ϕ) and 580 μm (z) in the barrel cylindrical layers, and it is 17 μm (ϕ) and 580 μm (R) in the end-cap disks. The total number of readout channels in the SCT is approximately 6.3 million.

The transition radiation tracker (TRT)

The TRT is trackers covering angle within $|\eta| < 2.0$, providing 30 hits per a track in average and 36 hits per a track at maximum. The TRT is basic drift (straw) tubes filled with gas mixture of Xe(70%), CO_2(27%), and O_2(3%). The diameter is 4 mm and typically 1,530 V is applied between anode and cathode which results in a gain of 2.5×10^4. The maximum drift time is 48 ns in the tubes, and the intrinsic resolution of the drift circle measurements is 130 μm, where the left-right ambiguities in the drift circle measurements can be solved by extrapolating tracks from the Pixel and SCT detectors. The TRT system contributes not only tracking but also the electron identification. The tubes are interleaved with the radiators consisting of polypropylene foils or fibers to produce the transition radiation X-rays. Its energy deposits depend on the Lorentz factor of the passing charged particles. Therefore, high energy deposit in the straw tubes (typically 6 GeV) from the transition radiation is expected especially for electrons, while the typical energy deposit of the minimum ionizing process is 250 MeV. The number of hits with high energy deposit is contributing electron identification to avoid selection of hadron particle as electrons. The threshold to distinguish electrons is set typically at 2 GeV.

The track reconstruction

Combining the three-detector information, the tracking reconstruction is performed. The inner detector track reconstruction consists of following three stages:

- The hits of SCT and Pixels are converted into clusters. A combination of SCT clusters on two neighboring layers are transformed into space-points using stereo angle their information. The TRT hit-timing information is converted into calibrated drift circles.
- The track seeds are formed with three pixel layers and the first SCT layer. These seeds are then extended throughout the SCT to form track candidates. The track candidates are extended into the TRT in order to associate drift circle information in a road around the extrapolation and resolve the left-right ambiguities. Finally the extended tracks are refitted with the full information of all three detectors.
- Vertex reconstruction algorithm will follow the track reconstruction. The primary vertexes reconstruction and photon conversion reconstruction will run after that.

3.2.3 Calorimetry at the electromagnetic calorimeter (LAr) and the electron reconstruction

The ID is surrounded by the electromagnetic (EM) calorimeter in order to measure energies of the electromagnetic showers from electrons and photons. The layout of all the calorimeter, including hadron calorimeter, is illustrated in Figure 3.5(a).

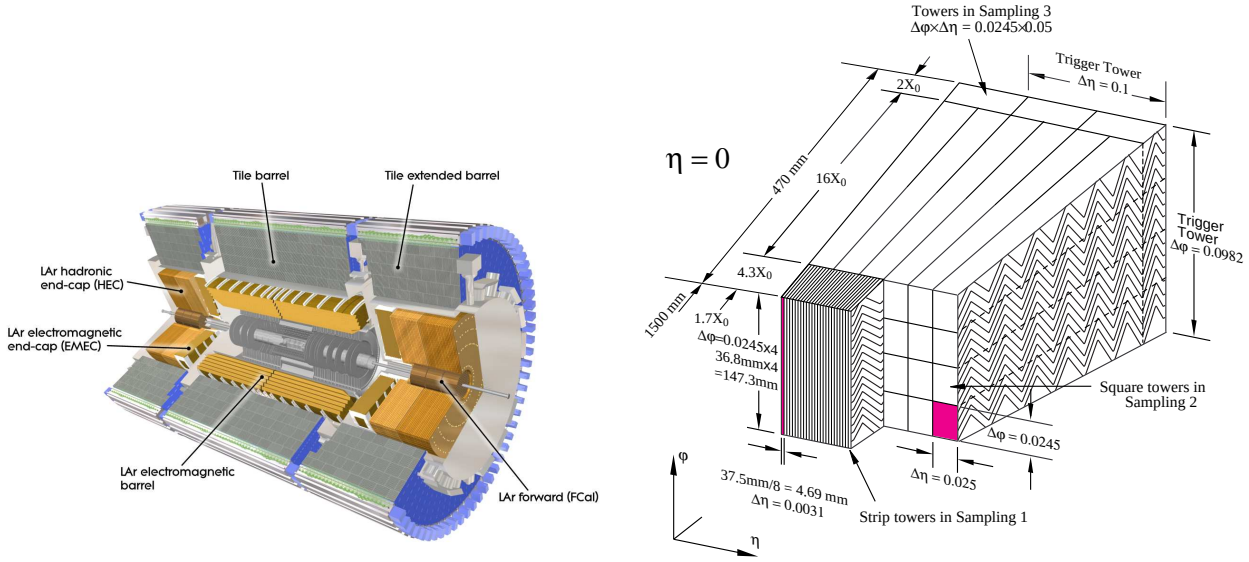

(a) (b)

Figure 3.5: The ATLAS calorimeter system.

The electromagnetic calorimeter (LAr)

The total thickness of the calorimeter is greater than 22 radiation lengths (X_0) in the barrel, and greater than 24 X_0 in the end-caps, which results in a good performance of calorimetry of EM showers. The EM calorimeter consists of lead plates ($\approx$ 1.5 mm) as absorbers and 2.1 mm

gaps filled with the liquid argon, as shown in Figure 3.5(b). The calorimetry is performed by measuring ionization of charged particles in the EM showers inside the liquid argon, so the ATLAS EM calorimeter is called LAr. A high voltage of 2,000 V is applied to the gaps and the maximum drift time of the ionized particles is 450 ns. The LAr calorimeter system consists of barrel part ($0 < |\eta| < 1.475$) and end-cap part ($1.375 < |\eta| < 3.2$)[*4]. The operation parameter is optimized as a function of η. The LAr calorimeter has a fine segmentation in both the lateral ($\eta \times \phi$ space) and longitudinal directions of the showers and the longitudinal segmentation corresponds to three layers of the LAr calorimeter. The properties of the three layers are itemized below:

- The first (innermost) layer consists of finer-grained strips in the η-direction with a coarse granularity in ϕ ($\Delta\eta \times \Delta\phi = 0.025/8 \times 0.098$). This offers excellent $\gamma - \pi^0$ discrimination. The typical radiation length of the first layer is 4.3 X_0.
- The second layer introduces 16 X_0 of the thickness, and the most of the EM shower energy is collected in this layer. This layer has a lateral granularity of 0.025×0.025. This layer provides seeds of the electron and photon reconstruction.
- The third layer has a granularity of $\Delta\eta \times \Delta\phi = 0.050 \times 0.025$. This layer enables a correction for the tail of very highly energetic EM showers.

Adding to the three layers, the layers are complemented by a presampler layer placed in front with coarse granularity. The layer covers the range $|\eta| < 1.8$ in order to correct energy lost in the material before the calorimeter.

Electron reconstruction

Electron reconstruction begins with the creation of a preliminary set of seed clusters. Seed clusters with energies above 2.5 GeV are formed with a cluster size of 0.075×0.125 ($\Delta\eta \times \Delta\phi$) in the second layer. An electron is defined by the existence of one or more reconstructed tracks matching to a seed cluster. Matching between reconstructed tracks and seed clusters is performed by extrapolating the ID tracks to the second layer of the calorimeter. Additional identification conditions follow the track-cluster matching in order to reject background electrons, such as electrons from photon conversions and mis-identification of jets. The conditions are defined with respect to parameters listed below, and the threshold values for these parameters are optimized, depending on the pseudo-rapidity (η) and cluster energy (E_T).

- $|\eta| < 2.47$
- Hadronic leakage with respect to ratio between hadron calorimeter and EM calorimeter
- Shower shape (width and lateral energy deposit distribution) reconstructed from response at the second layer and the first layer of EM calorimeter
- Tracking quality cuts with respect to the hit multiplicity in the inner detector, including hit requirement at the most inner layer and impact parameters

[*4]The LAr components within $|\eta| < 2.5$ contribute to the electron identification.

- Track-cluster matching quality ($\Delta\eta < 0.005$ and $\Delta\phi < 0.02$)
- Ratio of the TRT high threshold (2 GeV) hits to total number of the TRT hits

Also electrons matching reconstructed photon conversion vertexes are vetoed. Figure 3.6 shows two of the variables used in the electron identification for electrons from W decays and other possible background electrons[*5]. Figure 3.7 shows the expectation of the identification efficiency as a function of η and p_T, and the electron reconstruction and identification efficiency is expected to be 75% for the electrons with $E_T > 25$ GeV from W decays in $t\bar{t}$ events, where 25 GeV is E_T cut used in the analysis. The efficiency is confirmed by efficiency measurements.

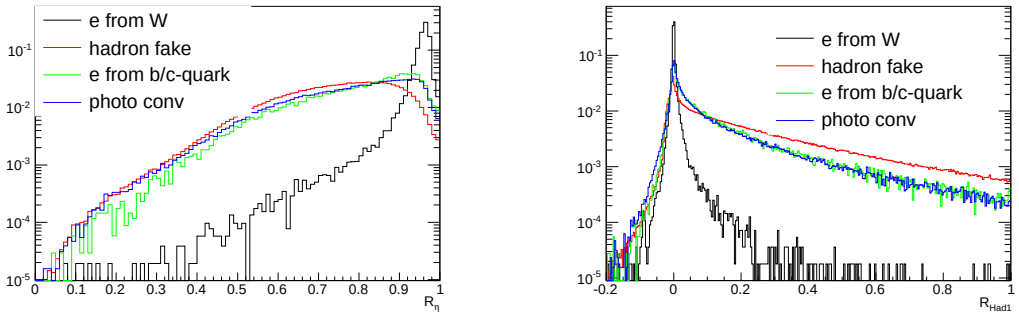

(a) (b)

Figure 3.6: Two parameters used in the electron identification in the simulation data for non isolated electron from heavy flavor decay, mis-identification of hadrons, and electrons from photon conversion, respectively. (a) Ratio of energy deposit in cells of 3×7 ($\eta \times \phi$) cells over 7×7 in the second compartment of the electromagnetic calorimeter. (b) Energy leakage into the first layer of the hadronic calorimeter over cluster E_T.

3.2.4 Calorimetry at the hadron calorimeter and the jet reconstruction

The ATLAS employs hadron calorimeter system with very large angle coverage up to $|\eta| = 4.9$ in order to measure energies of hadron objects. This plays a main role in calculating E_T^{miss}, which is defined as imbalance of the transverse energy flow.

The hadron calorimeter

Adding to the electromagnetic calorimeters that is introduced in section 3.2.3, the ATLAS detector is equipped with the hadron calorimeter surrounding the electromagnetic calorimeter components. The granularity and material vary as a function of η, and the cell size is typically $\Delta\eta \times \Delta\phi = 0.1 \times 0.1$ with three longitudinal segments at least. The hadronic calorimeters

[*5]They are categorized into non isolated electron from heavy flavor decay, mis-identification of hadrons, and electrons from photon conversion, respectively.

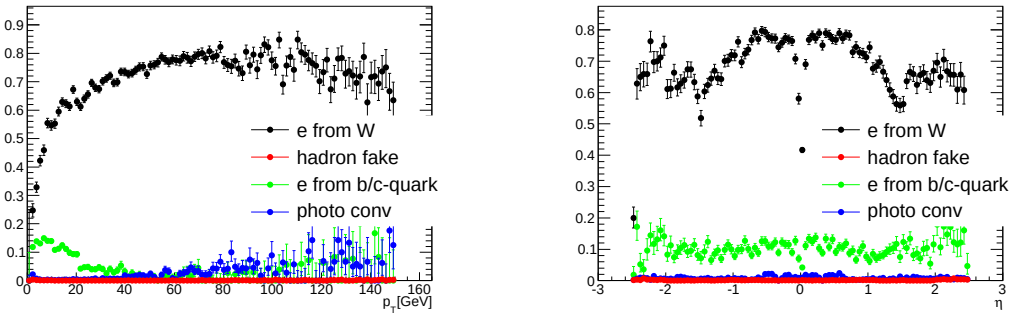

(a) (b)

Figure 3.7: Electron identification efficiency evaluated with simulation samples as functions of η, and p_T.

use plastic scintillator and steel for the barrel and extended barrels covering $0 < |\eta| < 0.8$ and $0.8 < |\eta| < 1.7$, respectively, and liquid argon and copper for the end-caps ($1.5 < |\eta| < 3.2$). The forward calorimeter is a liquid argon and tungsten/copper detector and extended the calorimetry up to $|\eta| < 4.9$. The total thickness of the hadron calorimeter is at least 10 interaction lengths over the whole acceptance region. The ATLAS calorimeter system is illustrated in Figure 3.5(a).

Jet reconstruction

The jet reconstruction is performed with the so-called anti-k_t algorithm [19] with inputs of the calorimeter clusters.

The calorimeter clusters are reconstructed by the topological cell cluster algorithm [20]. The clustering starts with seed cells which have high energy deposits above a particular threshold (a signal-to-noise ratio S/N above 4.0). All neighboring cells of these seeds, in all three dimensions, are collected into the cluster. Neighboring cells of neighbors will be added if the S/N is greater than 2.0. Finally the surrounding cells are added to the clusters if they have the energy reconstructed to be > 0 GeV. A four-momentum (E, p_x, p_y, p_z) of a cluster is evaluated with assumption of $m_{\rm cluster} = 0$.

The topologically-reconstructed clusters are fed into the jet reconstruction of the anti-k_t algorithm. In the algorithm, d_{ij} is defined like following:

$$d_{ij} \equiv \min({p_T}_i^{-2}, {p_T}_j^{-2}) \frac{\Delta R_{ij}^2}{R^2} = \min({p_T}_i^{-2}, {p_T}_j^{-2}) \frac{\Delta\eta_{ij}^2 + \Delta\phi_{ij}^2}{R^2} \ (i \neq j) \tag{3.1}$$

$$d_{ij} \equiv {p_T}_i^{-2} \ (i = j) \tag{3.2}$$

where the R is the distance parameter used in the jet reconstruction, and $R = 0.4$ is chosen in the analysis. All the clusters are ordered with ${p_T}^{-1}$ and listed as jet candidates. For the i-th cluster, the d_{ij} is evaluated to all the listed clusters in order to find the minimum (d_{min}) of all d_{ij} that includes $d_{ii} \equiv {p_T}_i^{-2}$. If the d_{min} is a ${p_T}_i^{-2}$, the corresponding object i is considered to be a jet, and removed from the list. If the d_{min} is a d_{ij} $(i \neq j)$, the corresponding objects i

and j are combined into a new object k using a recombination of their four-momentum values. This procedure is repeated until all the objects are removed from the list. Then the set of jets are reconstructed without any overlap of the clusters between reconstructed jets. This reconstruction algorithm is so-called "anti-k_T".

The energy of calorimeter clusters is calibrated at the so-called electromagnetic scale, which is appropriate for the energy deposited by electrons or photons. Additionally, the energy is calibrated according to the response function tuned for the jets. The response function to evaluate the jet energy is established with simulation studies and beam-test results in order to reproduce the total momentum of particles belonging to the jets in particular distance parameter of dR. This full calibration is applied to jets satisfying its $p_T > 20$ GeV to avoid an additional large uncertainty of the calibration for low p_T jets.

3.2.5 The muon spectroscopy and the muon reconstruction

The muon spectrometers

The ATLAS detector is equipped with a Muon Spectrometer (MS) optimized to provide a momentum measurement with a relative resolution designed to be better than 3% over a wide p_T range (from 3 GeV up to 1 TeV) and 10% at $p_T = 1$ TeV. They are installed in the ATLAS detector, as shown in Figure 3.8. The momentum in the MS is measured from the deflection of the muon trajectory in the magnetic field generated by a system of air-core toroid coils. The MS track is reconstructed using three layers of precision drift tubes (MDT) in the pseudo-rapidity range $|\eta| < 2.0$ and two layers of MDT chambers behind one layer of cathode strip chambers (CSC) for $2.0 \leq |\eta| \leq 2.7$. Large and small MDT and CSC detectors alternate to cover the full angle in the transverse plane, following the azimuthal segmentation of the toroid magnet system. The spacial resolution of the MDT and CSC is typically better than 100 μm in each layer. Three layers of resistive plate chambers (RPC) in the barrel region ($|\eta| < 1.05$) and three layers of thin gap chambers (TGC) in the end-caps ($1.05 < |\eta| < 2.4$) provide fast response to select events with muons in the final state in every 25 ns, forming the ATLAS level-1 muon trigger as described in section 3.2.6. The trigger chambers also measure the muon trajectory in ϕ-coordinate.

The muon reconstruction

The muon reconstruction is performed by matching tracks found by the muon spectrometer and the inner detectors. Owing to the large absorption lengths (more than 10 absorption lengths) introduced by the ATLAS calorimeter, the reconstruction with the matching requirement suppress the mis-identification of jets as muons significantly and select the muons with a high efficiency. The reconstruction consists of following three steps:

- Reconstruct the muons by a combination of track segments in each of the three muon stations (MS standalone muon tracks). The MS standalone muon is extrapolated to the beam line, and track parameters which are expressed at the closest point to beam line are reconstructed. The track parameters consist of ϕ, θ, q/p, d_0, and z_0.

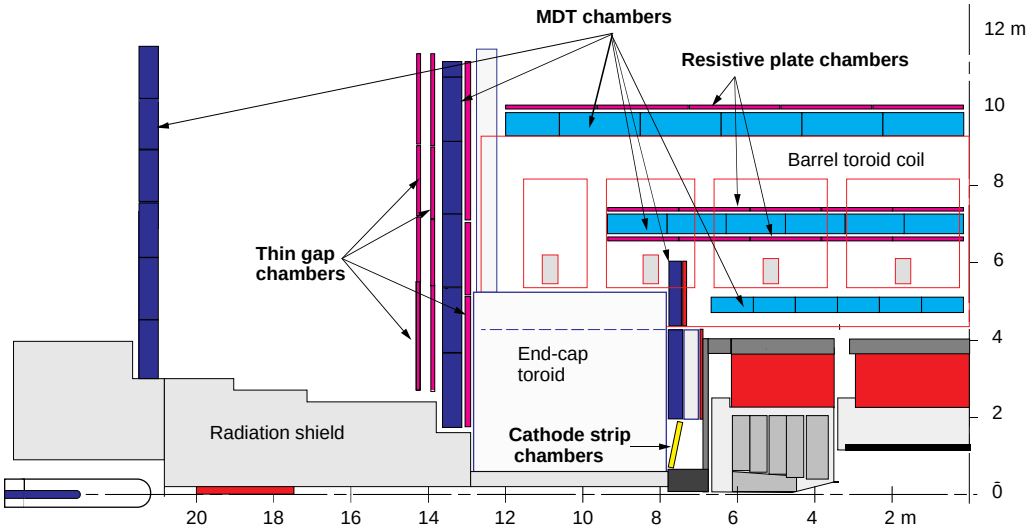

Figure 3.8: The ATLAS muon spectrometer.

- Reconstruct the muons with space points reconstructed from Pixel hits, SCT hits, and drift circles on TRT straw tubes (ID tracks). The ID tracks are required to satisfy quality conditions determined with number of hits in the inner detectors.

- Combine the MS standalone muon and ID trackers by interpolating the MS standalone muon track to the interaction points. The matching χ^2 is used in the combination to decide pairs with the best matching, and to measure the quality of the combination. It is defined as the difference between outer and inner track vectors weighted by their combined covariance matrix:

$$\chi^2 = (\mathbf{T_{MS}} - \mathbf{T_{MS}})^T(\mathbf{C_{ID}} + \mathbf{C_{MS}})^{-1}(\mathbf{T_{MS}} - \mathbf{T_{MS}}), \tag{3.3}$$

  where $\mathbf{T}$ denotes a vector of five track parameters and $\mathbf{C}$ denotes its covariance matrix. The subscript ID refers the inner detector and MS to the muon spectrometer.

3.2.6 Trigger

The ATLAS employs an excellent trigger system. The trigger system is designed to select pp collision events containing interesting physics objects before recording data so that the only interesting data are recorded. In particular, a rate of soft pp inelastic scattering via strong interactions is expected to be much higher than that of interesting physics processes. For example, it is higher than that of the interesting $t\bar{t}$ events by a factor of $\approx 10^9$, as shown in Figure 3.9. These less interesting events should be rejected effectively by the trigger system, and therefore, the trigger is an unique and highly important technique employed by the ATLAS experiment to achieve the most effective use of resources of the computer systems.

The ATLAS trigger and data acquisition system is based on three levels of event selection designed to capture interesting physics events with high efficiency from an initial bunch crossing rate of 40 MHz:

- Level-1 (L1) is hardware-based and running on the electronics implemented on the detectors or in the underground counting room
- Level-2 (L2) runs software-based algorithms on computing farms after the L1 trigger decisions using data only in the region of interest, which is called "RoI", indicated by the L1
- Event Filter (EF) provides more precise trigger decisions using data selected by the L1 and L2 with complete event information recorded by all the sub-detector systems.

The trigger algorithms can measure the energy and the multiplicity so that the tightness of the trigger conditions can be optimized according to the luminosity evolution.

The $t\bar{t}$ cross-section measurements use the single lepton triggers in the data taking. The single electron and single muon trigger algorithms are introduced in the following sections.

Single electron trigger

The single electron trigger is designed to record events containing high p_T electrons within $|\eta| < 2.5$ selectively. At the L1, e/γ-clusters are triggered using calorimeter information with granularity of $\Delta\eta \times \Delta\phi \approx 0.1 \times 0.1$, which is called "trigger tower", and the energy deposits in hadron calorimeter and electromagnetic calorimeter are summed. The L1 electron trigger is fired if a cluster of 2×2 trigger towers contains one pair of neighboring trigger towers with a combined energy above the required threshold (14 GeV). At the L2, and the EF, the electron trigger makes additional use of the ATLAS inner detector to perform better electron identifications. Seeded by the position of L1-cluster, the L2 electron trigger performs a fast calorimeter and track reconstruction algorithms. In the L2 the clustering is performed using the 3×7 cells in η-ϕ plane with unit of $\Delta\eta \times \Delta\phi \approx 0.025 \times 0.025$. The EF following the L2 decision introduces more precise reconstruction than the L2 algorithm. Tight identification conditions are applied to the reconstructed clusters and tracks at L2 and EF in order to identify good electron candidates with respect of discriminant variables listed in Section 3.2.3. The E_T threshold required in EF and L2 algorithms is 20 GeV.

Single muon trigger

The single muon trigger is designed to record events containing high p_T muons within $|\eta| < 2.4$ selectively. At the L1, the muon trigger makes use of RPC in the barrel and TGC in the end-caps. The L1 algorithm require a coincidence between hits on the several layers of the RPC and the TGC. The logic requires that the pattern of the hits should meet a small curvature in the magnetic field. Based on the hit pattern, the L1 algorithm estimates the p_T of muons, and 10 GeV threshold is applied for L1 algorithm. At the L2 and EF, the MDT chambers, and the ID trackers are used to measure the momentum of muons more precisely than L1. The L2 starts by seeding the RoI given by the L1 and performs fast tracking algorithms. Furthermore, The EF employs a precise extrapolation algorithm between the ID and MS, simulating energy deposit and scattering in the calorimeters. It enables the EF algorithm to perform more precise muon reconstruction and momentum decisions than L2. The p_T threshold required in EF and L2 algorithms is 18 GeV for the $t\bar{t}$ cross-section analysis.

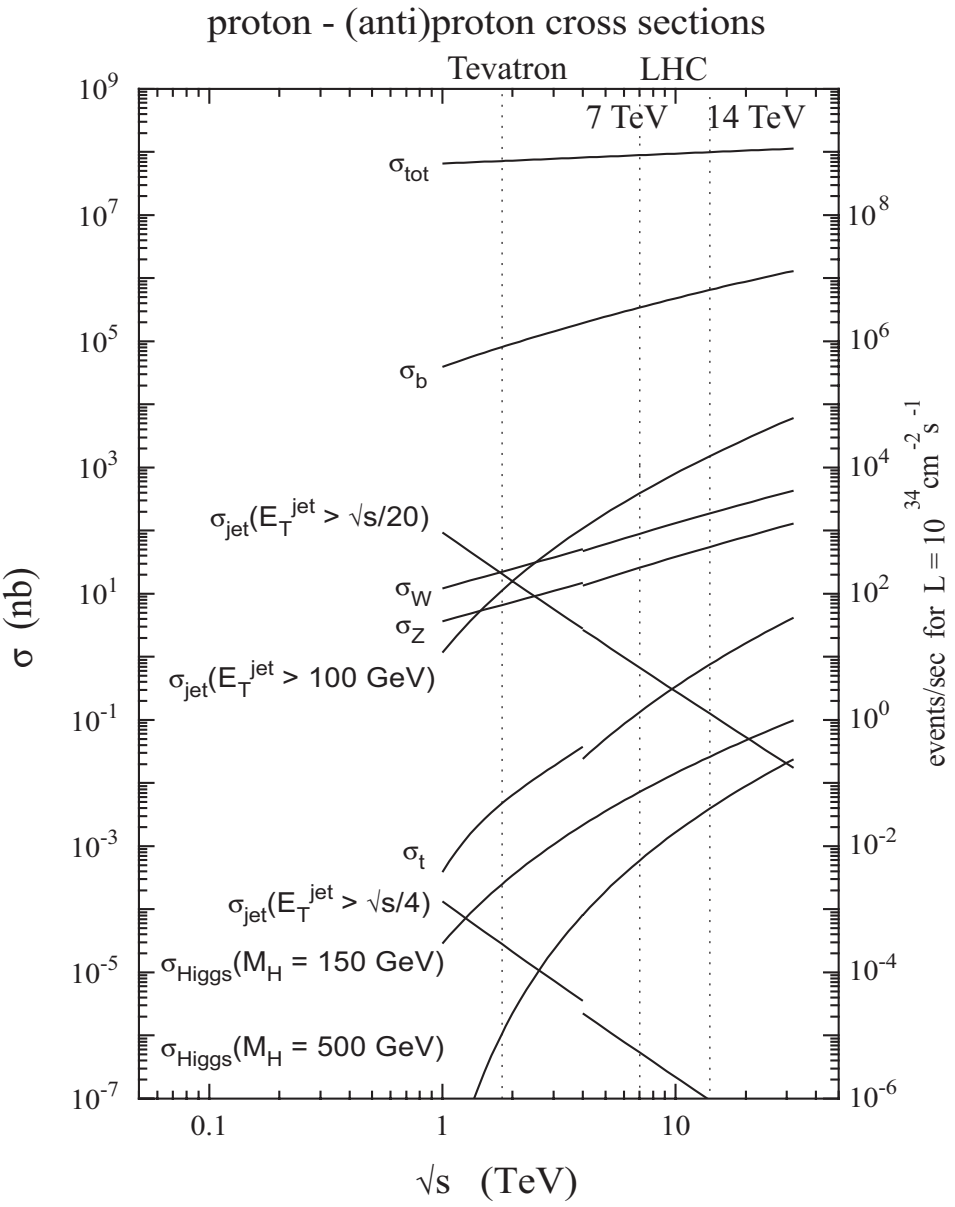

Figure 3.9: Expected event rates for several physics processes at the LHC design luminosity as a function of $\sqrt{s}$ of pp collisions (or $p\bar{p}$ collisions for $\sqrt{s} < 4$ TeV) [21]. The rates of interesting physics processes are much smaller than the total cross-section of the pp inelastic scattering. Trigger enables to record data containing interesting events effectively and efficiently.

Chapter 4

Commissioning of the Level-1 end-cap muon trigger system

4.1 Introduction

I have been leading the commissioning and the calibrations of the ATLAS Level-1 end-cap muon trigger system. In this section, these achievements are summarized.

The muon is an important signature in my $t\bar{t}$ analysis owing to its several properties as:

- A muon is a decay product from t-quarks and W bosons
- The technique to identify muons is simple, and its efficiency is high
- Soft pp inelastic scattering via strong interactions (soft QCD interactions), which is less interesting to the $t\bar{t}$ analysis, has the largest cross-section ($\approx 10^9$ times larger than that of $t\bar{t}$) and is suppressed by requiring high-p_T muons, since muons are not created in such soft QCD interactions directly. Muon trigger is designed so that it selects interesting events that contain muons with its rate about 70 Hz out of 10^9 Hz soft QCD events.

The $t\bar{t}$ samples in $e\mu$ and $\mu\mu$ final states are characterized by muon signals, and they are collected by the ATLAS muon trigger system. The muon trigger system selects events containing high-p_T muons before recording data so that the most effective use of the computing system can be achieved, as discussed in the previous section. Once the muon trigger system is fired, the ATLAS system records the complete data from all the detector subsystems that are used to identify the $t\bar{t}$ events. Since the stable data taking cannot be achieved without establishing a high performance of the muon trigger system, the successful calibration of the trigger is essential to the $t\bar{t}$ analysis. In particular, since the Level-1 muon trigger system performs its trigger calculation on the electronics implemented in the underground laboratory of the ATLAS experiment, the calibrations and the commissioning at the start-up of the LHC experiments are required. I have achieved the following tasks toward a superior performance of the Level-1 muon trigger system:

- Install all the electronics to the underground laboratory, and test them in order to avoid initial failures

- Develop control systems of all the trigger electronics in order to establish stable operations with a correct configuration
- Keep monitoring status of individual detector components and optimizing the electronics configuration in order to avoid inefficiency of the muon trigger system
- Adjust the signal timing in order to establish the highest efficiency

In particular, adjustment of the signal timing is discussed in the following sections.

4.2 Bunch Crossing Identification and the ATLAS trigger system

It is a unique point for the ATLAS trigger system to identify exact one bunch crossing by the trigger algorithm. It is mandatory in order to achieve the most effective data taking, considering the high collision rate of the LHC (more than 10 pp pairs may collide at a bunch crossing). It is so-called "Bunch Crossing Identification (BCID)". The BCID decisions are provided to all the ATLAS detector components to record data and build the complete event information of the interesting bunch crossing. The Level-1 trigger system performs the BCID so that the Level-2 trigger and Event Filter trigger can run their precise algorithm using data of only selected bunch crossings as well as muon reconstruction algorithms running on recorded data.

4.3 The ATLAS Level-1 muon trigger and the requirements

The ATLAS Level-1 end-cap muon trigger systems consists of 7 layers of Thin Gap Chambers (TGCs) and covers phase space corresponding to $1.04 < |\eta| < 2.4$. The TGC is a type of gas chambers to measure passing charged particles by amplifying the ionized electron signals with a good time resolution of ≈ 25 ns. They are located at $Z = 13$ m (1st, 2nd, and 3rd layers; TGC-1), 14 m (4th and 5th layers; TGC-2), and 15 m (6th and 7th layers; TGC-3), as shown in Figure 4.1.

TGC can measure positions of passing muons with two types of readout which are anode wires (so-called "wire") and pickup strips (so-called "strip"). The wire and strip readouts are orthogonal to each other in order to perform two-dimensional position measurements. A troid-magnet equipped in front of the TGCs bends muons, and therefore, an angle measurement of the muon trajectory enables measurements of the p_T since the curvature on the magnetic field is proportional to the p_T. The essence of the trigger logic can be summarized as follows:

- Output signals of the TGCs beyond a particular threshold are digitized as hits, and all the individual hits are labeled with correct BCIDs (hit BCID)
- Estimate p_T of muons with respect to a hit pattern of the 7 layers of the TGCs for all the individual bunch crossings (hit coincidence).

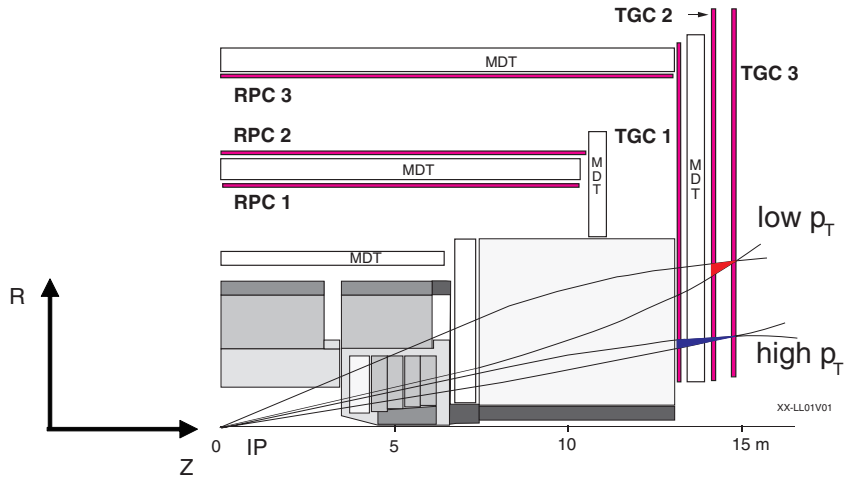

(a)

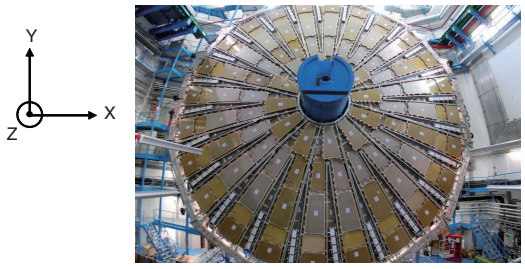

(b)

Figure 4.1: (a) The cross-section diagram of the muon detectors looking at one fourth R-z plane. (b) Structure of the TGC chambers at x-y plane

Technically, the hit BCID can be achieved by shaping asynchronous TGC hit signals into synchronized signals to the pp bunch crossings. Figure 4.2(a) shows a block diagram of the circuit that performs the hit BCID. It is implemented for all the individual channels of the TGCs (320k channels in total). Asynchronous TGC signals are latched by a clock signal given by the 40 MHz LHC radio-frequency (25 ns period), and synchronized to the pp bunch crossings in the ATLAS detector, as shown in Figure 4.2(b). Timing adjustments of the clock signals and TGC hit signals should be done coherently in all the TGC readout channels in order to label all TGC hits with a correct BCID. The following timing adjustments are required:

- Alignment of the timing of the clock signals (clock-phase) (see Section 4.4)
- Alignment of the input timing of the TGC hit signal (see Section 4.5)
- Tune of the relative timing between the clocks and the TGC hit signals (see Section 4.6).

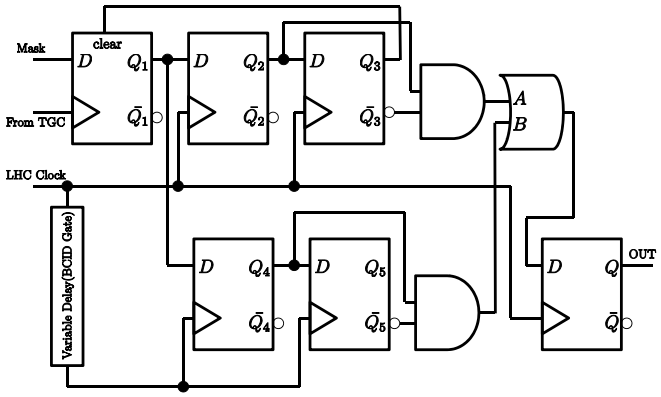

(a)

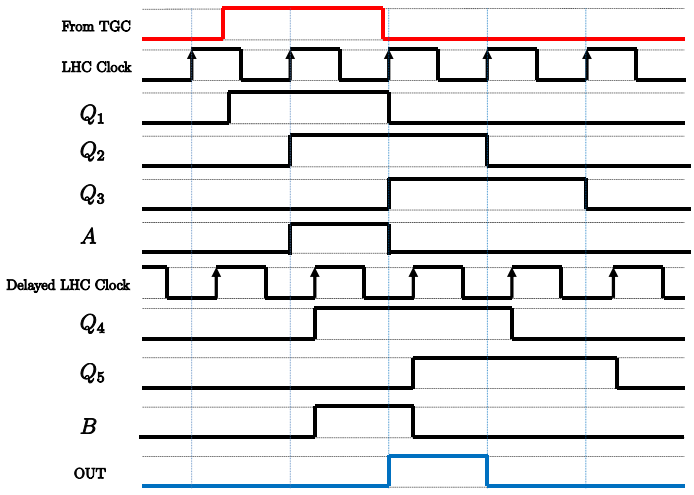

(b)

Figure 4.2: (a) The schematics of the BCID circuit consisting of the D-type flip-flop circuits. (b) The timing chart of the BCID functionality, where an asynchronous hit signal from TGC (red line) is shaped into a synchronous signal with its width equal to 25 ns (blue line), the boundaries of which are determined by the given LHC clocks and illustrated by blue vertical lines. The notations in the schematics above are used in the timing chart. The delayed clock is used to enlarge the BCID gate, as discussed in Appendix C.1.

4.4 Alignment of the timing of the clock signals (clock-phase)

The clock signal is distributed by the central system to all the individual electronics mounted on the TGC detectors via $\approx$ 100 optical fiber links. Receiver modules employ a variable delay

circuits to align the clock-phase so that the fiber length difference, which is varying from 50 m to 100 m, is absorbed there. The minimum size of the variable delays is 100 ps. The relative length of all the fibers has been measured with reference to that of the longest fiber link by the following measurement:

- A pulse signal with its width of 25 ns is sent to all the receiver modules
- Measure the relative timing of the pulse's arrival between a particular receiver module and the reference receiver module with a 100 ps precision with an oscilloscope.

The 100 ps precision is corresponding to precision of ≈ 2 cm out of 100 m. The configuration of the timing parameter is determined by the results for all the individual optical-fiber links.

4.5 Alignment of the input timing of the TGC hit signals

The arrival timing of the hits signals from the TGC detectors varies for all the channels, which is proportional to the following:

- Time of flight that is proportional to the flight path length of the muon between the interaction point (detector center) to the detector surface, which varies from 13.5 m to 19 m (see Figure 4.1(a))
- Time of propagation that is proportional to the cable length between the detectors and the electronics, which varies from 2 m to 14.5 m.

The difference of the hit signal timing is absorbed by a variable delay functionality employed in the receiver module with the minimum size of delay equal to 1 ns.

Time of flight can be estimated from the light velocity and the detector positions for each channel. For the time of propagation, a test-pulse functionality is implemented in the TGC system, which is shown in Figure 4.3, to measure the length of all the individual cables. The test-pulse trigger can be delayed by $n_{\text{testpulse delay}} \times 1$ ns, where n can be set to be from 0 to 31. The readout timing with respect to the test-pulse timing can be controlled with a step of 25 ns ($N \times 25$ ns). Then, the time of propagation in all the individual cables can be determined by a scan of the (n, N). Propagation delay time of all the cables has been measured with a ≈ 1 ns precision. The results has been cross-checked with a predicted propagation time given by the designed value of the cable length and the well-known propagation velocity of the signal in copper cables (0.2 m/ns) and found to be in good agreement with the prediction, which convinces of the measurements.

4.6 Tune of the relative timing between the clocks and the TGC hit signals

The TGC detector system has a typical intrinsic time spread (time jitter) of ≈ 25 ns. Figure 4.4 shows a typical hit timing distribution of a TGC chamber for particles with their incident

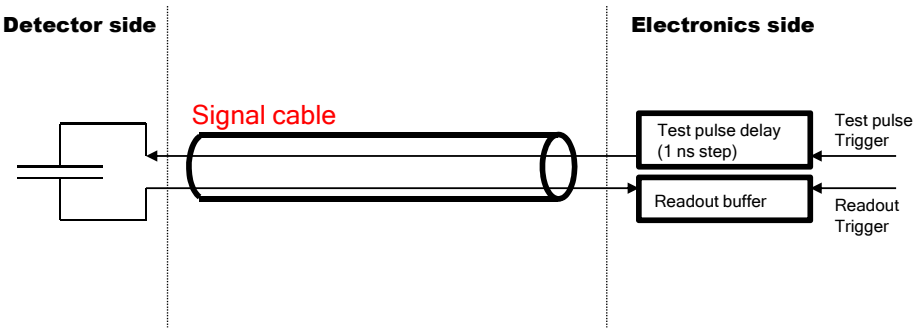

Figure 4.3: The test-pulse functionality that is equipped in order to measure the propagation time in the signal cables with a 1 ns precision.

angle of 30 degree, and the width of distribution is about 20 ns. Furthermore, the signal propagation delay in the TGC chamber depends on the incident position (i.e. how far from readout electronics) and it results in an additional jitter of from ≈ 5 ns to ≈ 10 ns. Considering the intrinsic time jitter, the clock phase should be tuned to achieve the best efficiency, as shown in Figure 4.5. Owing to adjustments of the clock-phase and the hit signal timing, as discussed in the previous sections, the adjustment of the relative timing can be achieved by an application of an appropriate offset for the clock signals, which is common for all the channels.

Since the wrong relative timing configuration may result in the higher probability of failures in BCID, so-called mis-BCID rate, the optimization can be done by a mis-BCID rate measurement with several configurations of the clock phase offset parameter. The measurements have been done with following special conditions of data taking:

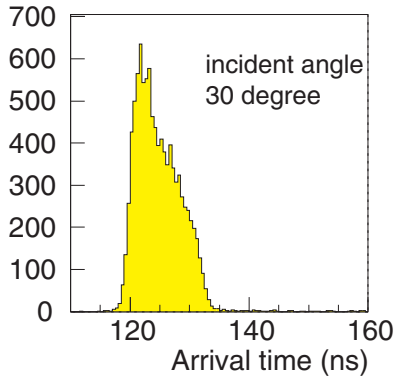

Figure 4.4: The intrinsic time jitter of the TGC wire signals for charged particles with their incident angle equal 30 degree [22].

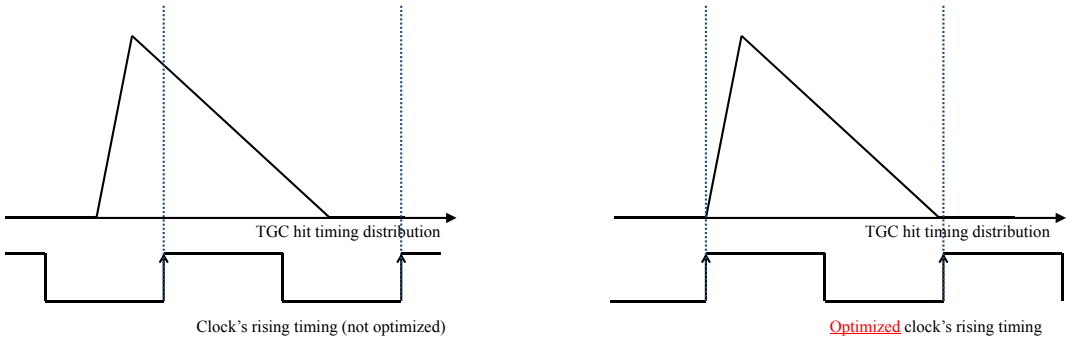

(a) (b)

Figure 4.5: The top figures show hit signal timing distributions and the bottom figures show the relative timing of the clock's rising. The timing of the clock's rising should meet the fastest edge of hit signal distribution, as shown in (b), so that the correct BCID can be applied to the fastest signal as well.

- Only 25 bunches are filled by protons out of 2808 bunches (i.e. only a bunch per ≈ 100 bunches are filled, and the others are empty) so that exact BCID can be defined for each of triggers and hits
- Even if the trigger is identified to an empty neighboring bunch crossing, which corresponds to the wrong BCID of the trigger decisions, the event reconstruction is done as if the trigger is fired in the correct bunch crossing so that all muons can be reconstructed correctly even the trigger timing is wrong
- All BCID labeled to the individual trigger decisions are recorded in data so that the wrong BC-identified trigger decisions can be recognized in the analysis.

These special configurations enable to measure the mis-BCID rate with respect to good muons reconstructed with the ID and MS (see Section 3.2.5). Muons that are reconstructed with their $p_T > 5$ GeV and triggered by the Level-1 TGC trigger system are selected from the data sample, where reconstructed muons that are close to the RoI (see Section 3.2.6) given by the TGC trigger system within $dR < 0.5$ are considered to be triggered. It is expected that the wrong clock phase configuration may label the trigger signals especially with the previous BCID. Therefore, the mis-BCID rate (R) that can be used in the clock phase optimization is measured with the following definition:

$$R = \frac{\text{collected muons belonging to the previous BC}}{\text{all collected muons}}. \tag{4.1}$$

Figure 4.8 shows the mis-BCID rates as a function of the clock offset parameters, where the parameter corresponding to -2 ns in the figure is found to be optimal. Finally an offset parameter corresponding to the -4 ns is chosen, considering the fluctuation of the distributed LHC clock phase[*1].

[*1] It is known that the phase can vary by a level of 2 ns due to the temperature difference.

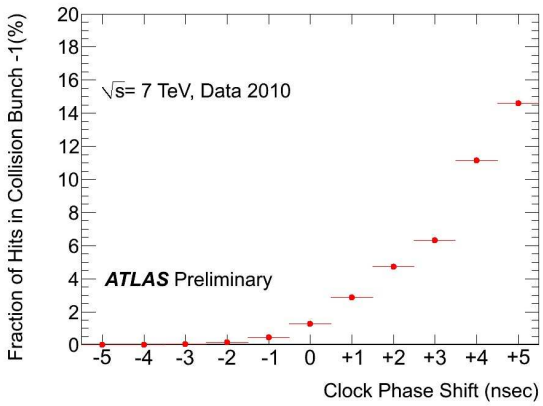

Figure 4.6: The mis-BCID rates as a function of the clock offset parameters. The optimal configuration has been determined to be −4 ns with respect to a value that corresponds to the default setting of the electronics.

4.7 BCID gate width optimization

An additional parameter remained in the timing calibration is so-called "BCID gate width", which is determined additional delay for the LHC clock signals illustrated in Figure 4.2(a) and 4.2(b). A gate width that is longer than 25 ns allows a TGC hit to be labeled with two neighboring BCIDs, as discussed in Appendix C.1, to avoid inefficiency in the 7-layer coincidence due to late signals in the intrinsic time jitter. Therefore, the gate width should be long enough to cover all the signals, depending on the intrinsic time jitter, as shown in Figure 4.7, while the longer BCID gates results in a higher mis-BCID rate. Therefore, it should be optimized so that

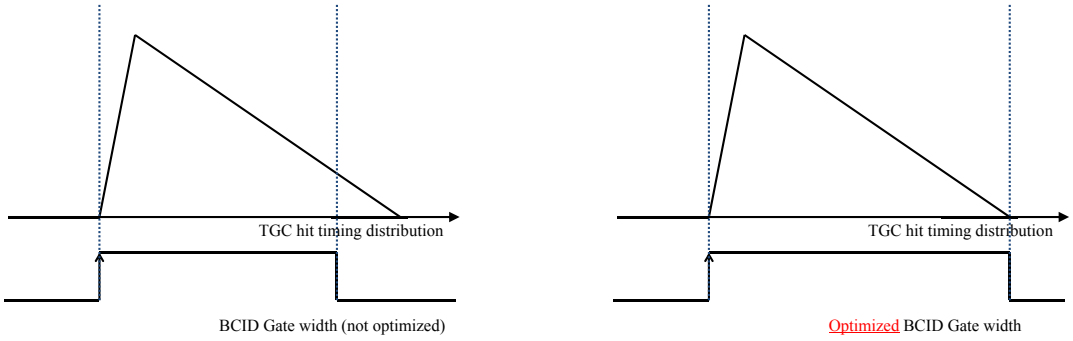

(a) (b)

Figure 4.7: The top figures show hit signal timing distributions and the bottom figures show the gate signal in the BCID circuit. The timing of closing edge of the gate should be aligned so that the gate includes the tails of the timing distributions, as shown in (b).

the mis-BCID rate due to the longer BCID gates is minimized. The efficiency of the correct BCID has been measured in order to choose an optimal BCID gate width, which is as short as

possible while minimizing the inefficiency. 28.6 ns and 41.1 ns are chosen as the optimal BCID gate width for wire and strip readout channels, respectively, depending on their intrinsic time jitter.

4.8 Trigger efficiency measurements

The calibrations have been validated by a measurement of the trigger efficiency of the Level-1 muon trigger system. Muons in a data sample recorded by a jet trigger can be considered to be free from the bias of the muon trigger and can be used for the muon trigger efficiency measurement. The trigger efficiency of a Level-1 trigger algorithm with a p_T threshold of 6 GeV has been measured with respect to good muons reconstructed by the MS and ID. Figure 4.8 shows the turn-on-curve of the trigger efficiency of the Level-1 muon trigger as a function of p_T. The plateau efficiency is measured to be 93.6% by a fit with the Fermi function, which is as a superior performance as designed. Thus, it convinces of the success in the timing calibrations.

These achievements are significant contributions toward the $t\bar{t}$ cross-section measurements as well as the other all physics analysis with muons in their final state. Owing to these achievements, uncertainties related to the muon trigger on $t\bar{t}$ cross-section measurements are limited small enough to neglect them, which is discussed in the next chapter.

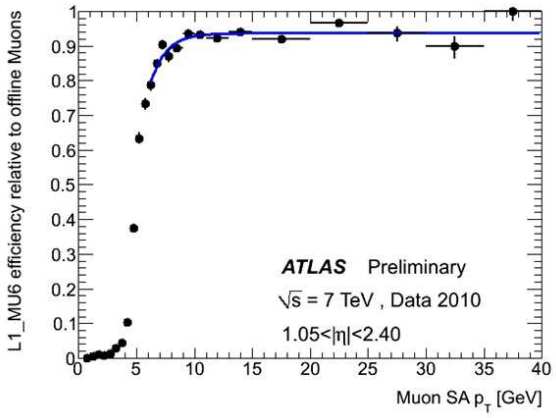

Figure 4.8: The measured trigger efficiency of the L1 Muon algorithm which requires $p_T >$ 6 GeV as function of offline reconstructed p_T. A efficiency at the plateau is measured to be 93.6 % by a fit with Fermi function.

Chapter 5

Measurements of $t\bar{t}$ production cross-section

5.1 Introduction

In the SM, a t-quark decays into a W boson and a b-quark 100% of the time. Therefore, the final state of the $t\bar{t}$ events can be categorized with decay products of two W bosons, as discussed in Section 2.3. In this analysis, the $t\bar{t}$ events are extracted using the dilepton final states which is characterized by a pair of leptons (electrons or muons) with high p_T from decays of two W bosons.

The decay modes treated as the signal in the analysis are listed below:

- $t\bar{t} \to W(\to e\nu)b + W(\to e\nu)b$
- $t\bar{t} \to W(\to \tau(\to e\nu\nu)\nu)b + W(\to e\nu)b$
- $t\bar{t} \to W(\to \tau(\to e\nu\nu)\nu)b + W(\to \tau(\to e\nu\nu)\nu)b$
- $t\bar{t} \to W(\to \mu\nu)b + W(\to \mu\nu)b$
- $t\bar{t} \to W(\to \tau(\to \mu\nu\nu)\nu)b + W(\to \mu\nu)b$
- $t\bar{t} \to W(\to \tau(\to \mu\nu\nu)\nu)b + W(\to \tau(\to \mu\nu\nu)\nu)b$
- $t\bar{t} \to W(\to \mu\nu)b + W(\to e\nu)b$
- $t\bar{t} \to W(\to \tau(\to \mu\nu\nu)\nu)b + W(\to e\nu)b$
- $t\bar{t} \to W(\to \tau(\to e\nu\nu)\nu)b + W(\to \mu\nu)b$
- $t\bar{t} \to W(\to \tau(\to e\nu\nu)\nu)b + W(\to \tau(\to \mu\nu\nu)\nu)b$

The first three decay modes are categorized into the ee final state, the second three decay modes are categorized into the $\mu\mu$ final state, and the last four decay modes are categorized into the $e\mu$ final state. As listed above, electrons and muons in decays of the τ leptons are included in the signal definition. The total branching fraction of these modes is 6.5%.

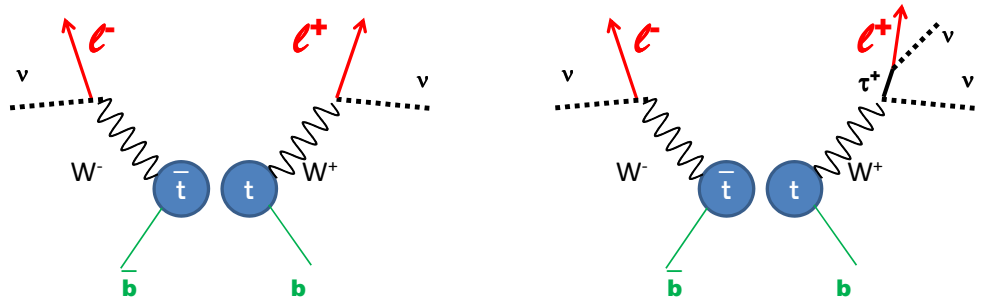

(a) (b)

Figure 5.1: The event topology of the $t\bar{t}$ signal events in the dilepton final states. $\ell^{\pm}$ denotes the either of an electron or a muon. (b) shows a topology including a leptonic τ-lepton decay.

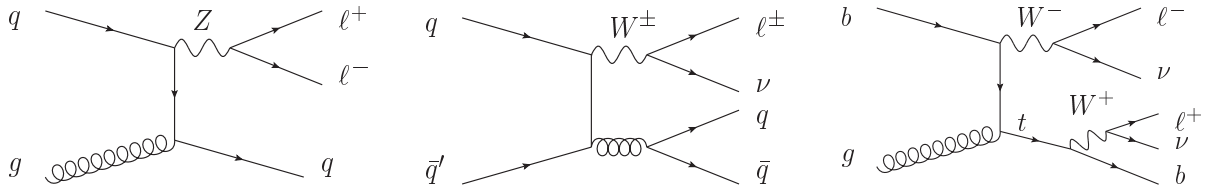

Figure 5.2: Background candidates: (a) Z/γ^*+jets, (b) W+jets, and (c) single t-quark (Wt) production events.

Adding to the pair of two leptons, the dilepton channel is characterized by the large missing transverse energy (E_T^{miss}) corresponding to undetected neutrinos from leptonic W decays, and two jets with large p_T corresponding to two b-quark from a $t\bar{t}$ decay. The event topology of the signal is illustrated in Figure 5.1. Other processes that have similar event topologies, such as multi-jets, W+jets, Z/γ^*+jets, di-boson (WW, WZ, ZZ), and single top (Wt) processes, can pollute the signal samples. Figure 5.2 shows diagrams of the background candidate processes.

The cross-section of the $t\bar{t}$ production is measured with following equation:

$$\sigma_{t\bar{t}}^{\text{measurement}} = \frac{N_{\text{observed}} - N_{\text{background}}}{\mathcal{A} \times \mathcal{L}} = \frac{N_{\text{observed}} - N_{\text{background}}}{N_{\text{signal expectation}}^{\text{SM}}} \times \sigma_{t\bar{t}}^{SM}, \tag{5.1}$$

where:

- $\mathcal{L}$ denotes the integrated luminosity of the pp collisions used in the analysis (see Section 5.2.1)
- N_{observed} denotes number of events selected by an application of event selection criteria to extract the $t\bar{t}$ production events effectively (see Section 5.5)

- $\mathcal{A}$ denotes the acceptance for the $t\bar{t}$ signals (see Section 5.5), which includes the phase-space acceptance, the selection efficiency and the sub-decay branching fractions
- $N_{\text{background}}$ denotes expected number of background contamination (see Section 5.6)
- $\sigma_{t\bar{t}}^{SM}$ denotes the reference cross-section ($164.6\ ^{+11.5}_{-15.8}$ pb) predicted by the SM theory (see Section 2.2)
- $N^{\text{SM}}_{\text{signal expectation}}$ denotes the expectation number of selected $t\bar{t}$ signals according to the theoretical cross-section of the $t\bar{t}$ production and the estimated $\mathcal{A}$, which is given by the simulation of the $t\bar{t}$ productions and decays (see Section 2.2 and Section 2.3).

The properties of the extracted $t\bar{t}$ samples and the results of the $t\bar{t}$ cross-section measurement are examined from several aspects in Section 5.7, 5.8 and 5.9.

5.2 Data-set and data taking

5.2.1 Collision data

This analysis uses the collision data recorded in 2011 (from March to July) with $\sqrt{s} = 7$ TeV. The evaluated integrated luminosity is shown as a function of time in Figure 5.3. The instantaneous luminosity of pp collisions is estimated with the following equation:

$$\mathcal{L} = \frac{\mu n_{\text{b}} f_{\text{r}}}{\sigma_{\text{inel}}}, \tag{5.2}$$

where μ is an average number of inelastic interactions per a bunch crossing, n_{b} is the number of colliding bunch pairs, f_{r} is the machine revolution frequency (11.2 kHz), and σ_{inel} is the pp inelastic cross-section. The total inelastic scattering cross-section of pp collisions has been measured in the Van der Meer scan [24] precisely, and the μ is measured by a combination of several measurements of the forward detectors. The instantaneous luminosity was measured with its maximum of $\approx 10^{33}$ cm^{-2}s^{-1} during the data taking. Then the integrated luminosity ($\mathcal{L}$) for used data sample is estimated with an uncertainty of 3.7%[*1], details of which are discussed in Appendix B.2.

From the total integrated luminosity, only data for which all subsystems described in section 3.2.1 are fully operational in stable beam conditions are used in this analysis. A good quality of the data taking is required for muon reconstruction, electron reconstruction, tracking, E_T^{miss} calculation, beam operation, and luminosity measurements. The application of these requirements results in a data sample of 0.70 fb^{-1}.

Data taking is performed with the single lepton trigger for the analysis since all the final states contain two high p_T leptons. An electron trigger with p_T threshold of 20 GeV and a muon trigger with p_T threshold of 18 GeV are used to collect the $t\bar{t}$ samples (see Section 3.2.6). The data recording rates with an instantaneous luminosity of $\approx 10^{33}$ cm^{-2}s^{-1} are about 60 Hz and 40 Hz for the electron and muon triggers, respectively [25]. The number of all the events recorded by the two triggers, corresponding to the total luminosity of 0.70 fb^{-1}, is about 6.5×10^7.

[*1] it is dominated by the beam current uncertainty (3.0%) in the VDM scan.

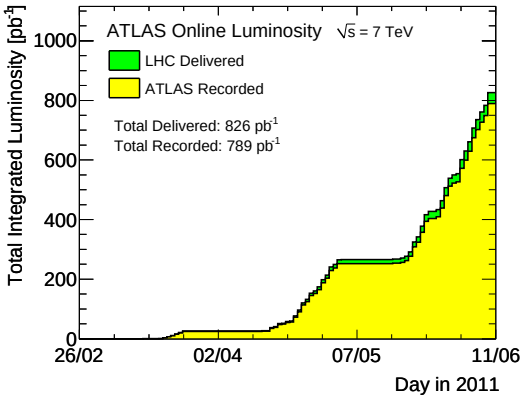

Figure 5.3: The integrated luminosity as a function of time. This recorded luminosity is before the application of data quality requirements. By application of the requirement, the available luminosity is 0.70 fb^{-1}.

5.2.2 The Monte Carlo simulation samples

The $t\bar{t}$ production events in pp collisions can be modeled by the SM theory, as reviewed in Chapter 2, and their details can be simulated by the Monte Carlo method (MC), which computes the particular physics events by the SM theory with assistance of repeated random sampling. The MC samples have been used to develop and validate the analysis procedures, calculate the acceptance of the $t\bar{t}$ events, and evaluate the contributions from some background processes. The MC events are generated by either NLO or LO approximation of the p-QCD. All simulated events are hadronized using the HERWIG shower model [26] supplemented by the JIMMY additional pp collision model [27]. After event generation, all samples have been processed with the GEANT4 [28] simulation of the ATLAS detector [29], reconstructed and passed through the same analysis chain as the data. The used MC generators and set of Parton Distribution Function (PDF) are summarized in Table 5.1. The different choice of the MC simulator and sets of PDF may cause difference in results, and such uncertainties are estimated by using different simulators (see Section 5.4).

Physics Process	Event Generation		PDF
	generator	approximation	
$t\bar{t}$ signal	MC@NLO [11]	NLO	CTEQ6.6 [10]
single top (Wt)	MC@NLO	NLO	CTEQ6.6
diboson (WW, WZ, ZZ)	ALPGEN [33]	LO	CTEQ6L1 [34]
Z+jets/W+jets	ALPGEN	LO	CTEQ6L1

Table 5.1: Summary of the simulation for all the simulated physics processes.

While the $t\bar{t}$ production and the single top production (the Wt production) events are simulated with the NLO QCD, they are normalized with the cross-sections estimated by the NNLO perturbative QCD calculation [30, 31]. The cross-sections of the diboson production

and Z/W+jets are normalized to match the total cross-section from NLO QCD predictions using calculations with the MCFM program [32].

In the following text, samples simulated by the MC are referred to as "MC" to distinguish them from the pp collision data that are referred to as "data".

5.2.3 Additional pp interactions

With the high instantaneous luminosity of the LHC equal to $\approx 10^{33}$ cm^{-2}s^{-1}, more than 5 interactions may occur per a pp bunch crossing. This means that the $t\bar{t}$ events are polluted by several uninteresting additional interactions. They are so-called pileup events. For estimating their efficiencies, the MC samples include the simulation of additional interactions. This is achieved by adding simulated pp inelastic scattering events to the main process randomly. The number of additional events to each simulated event is chosen according to a Poisson distribution with a given average of number of interaction $\langle\mu\rangle$, where $\langle\mu\rangle$ in the MC varies from 0 to 18 to describe the various conditions of the luminosity. The integrated luminosity is measured for approximately every one minute, which is a minimum unit of data taking called a luminosity block. The average number of interactions in the collision data is estimated for each luminosity block with the following equation:

$$\langle\mu\rangle = \frac{L_{\text{inst}} \times \sigma_{\text{inel}}}{N_{\text{bunches}} \times f_{\text{r}}}, \tag{5.3}$$

where L_{inst} is the integrated luminosity measured in the luminosity block, N_{bunches} is the number of colliding bunches, f_{r} is the revolution frequency and σ_{inel}=71.5 mb^{-1} is the total inelastic cross-section. The $\langle\mu\rangle$ distribution for data and the MC is shown in Figure 5.4.

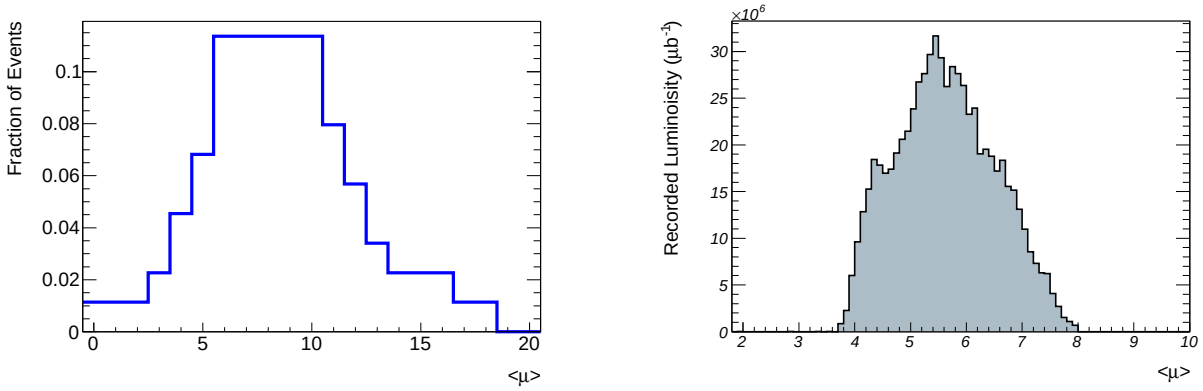

Figure 5.4: $\langle\mu\rangle$ distributions in the simulation (a) and in data taken in 2011 (b). The MC events are weighted to match this $\langle\mu\rangle$ distribution between data and the MC. The larger $\langle\mu\rangle$ parameter of the MC is corrected according to the measured $\langle\mu\rangle$.

The MC samples are weighted such that their $\langle\mu\rangle$ distributions match those measured in the collision data, which is so called a "pileup reweighting technique". The pileup events can affect the jet multiplicity distribution and the E_T^{miss} distribution, especially in Z boson events, where the small number of reconstructed jets and small E_T^{miss} are expected. It is

checked that it is mandatory to apply this additional weight to describe the pileup effect on E_T^{miss} distribution, lepton isolation efficiency, jet multiplicity distribution using control regions dominated by Z+jets events, as shown in Figure 5.5, and 5.6. The application of pileup reweighting is found to improve the agreement between the data and and the MC. All the analyses using MC are done with the application of the pileup reweighting method so that the effect of the pileup events can be reproduced correctly in the simulated samples.

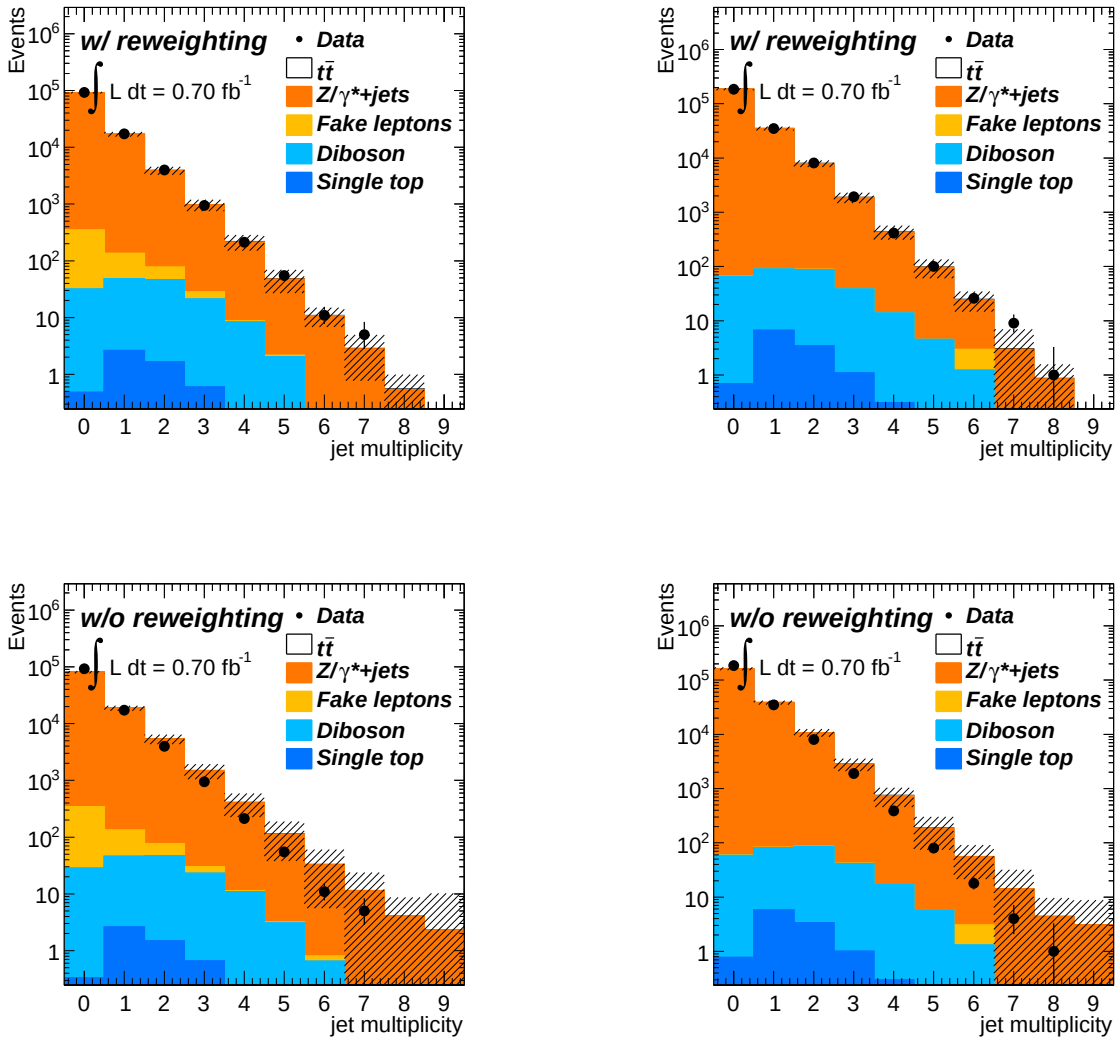

Figure 5.5: Jet multiplicity distribution in $Z \to ee$ (left figure), and $Z \to \mu\mu$ (right figure). The Pileup reweighting is applied for the top two figures, and not for the bottom two. The distribution of jet multiplicity distributions in the MC becomes softer by applying pileup correction, and the better matching between data and the MC is obtained.

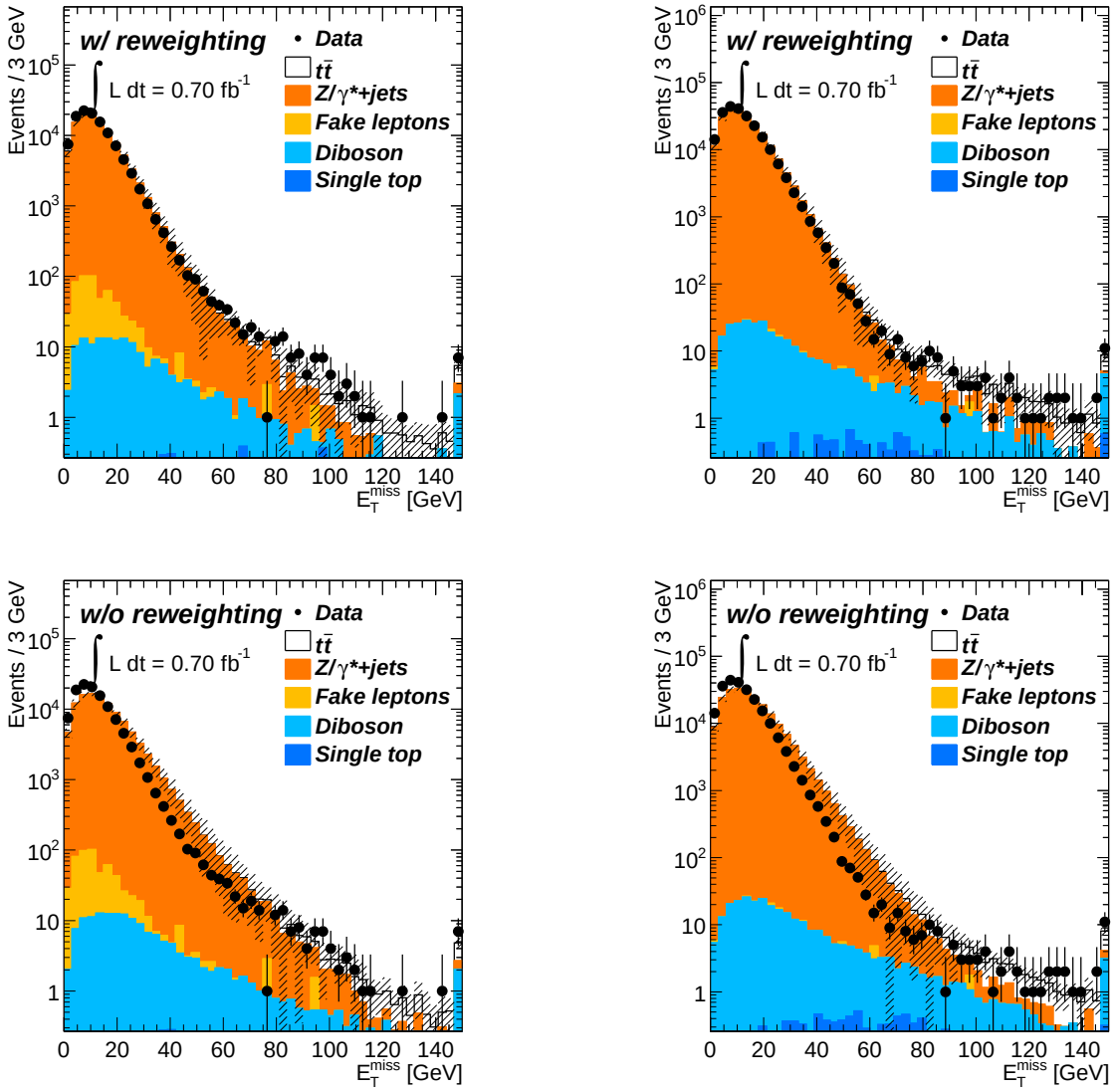

Figure 5.6: E_T^{miss} distribution in $Z \to ee$ (left figure), and $Z \to \mu\mu$ (right figure). The Pileup reweighting is applied for the top two figures, and not for the bottom two. The distribution of E_T^{miss} in the MC becomes softer by applying pileup correction, and the better matching between data and the MC is obtained.

5.3 Object definition and evaluation of detector performances

The reconstruction and identification of $t\bar{t}$ dilepton events make use of electrons, muons, jets, and missing transverse energy, which is a signature of undetected neutrinos. This section will describe the definitions of these objects in the analysis and the valuation of the corresponding detector performances.

5.3.1 Object definition

Electron identification

Adding to the standard electron reconstruction summarized in Section 3.2.3, phase space and isolation cuts are applied in the electron selection to collect the well-controlled electrons and to suppress backgrounds from the photon conversions, electrons from decays of heavy flavor (b-, c-quarks) hadrons, and jets mis-identified as electrons[*2]. They are required to satisfy the transverse momentum $p_T > 25$ GeV[*3] (Figure 5.7(a)) and $|\eta| < 2.47$. Candidates in the barrel to end-cap calorimeter transition region in $1.37 < |\eta| < 1.52$ are excluded due to the poor performance there. The electron candidates are required to be isolated from other hadron activities. The isolation is defined with energy deposited in the calorimeter cells within $\Delta R < 0.2$ around the electron, referred to as "*etcone*" hereafter (Figure 5.7(b)). The *etcone* is required to be less than 3.5 GeV after correction of the leakage of the electron energy. The typical efficiency value of the electron identification is about 75%, depending on the E_T and η of reconstructed electrons.

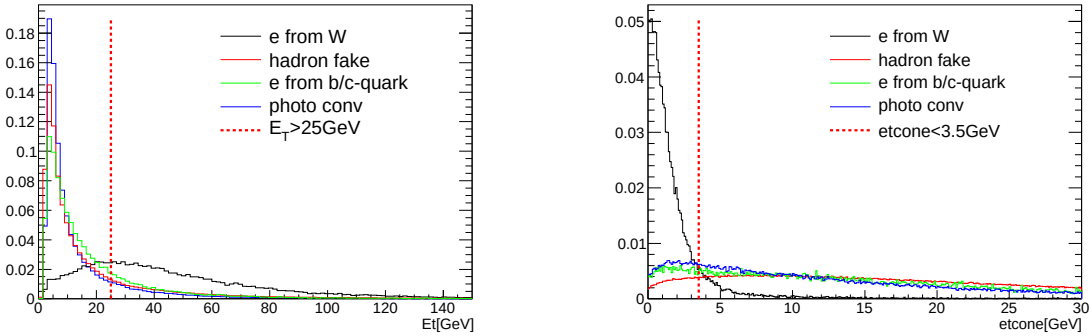

(a) (b)

Figure 5.7: (a) The p_T and (b) the *etcone* distributions for the reconstructed electrons for signals and backgrounds, respectively. The backgrounds are categorized into those from the photon conversions, electrons from decays of the heavy flavor hadrons, and the mis-identified jets as electrons. They are evaluated using signal and background electrons contained by the simulation sample of $t\bar{t}$ events.

Muon identification

For obtaining well-controlled muon samples and avoiding selecting background muons from decays of heavy flavor hadrons and decay-in-flight of light mesons, phase space and isolation cuts are applied in the muon selection as well as electrons. The muons are required to satisfy

[*2]Approximately 50% of the backgrounds electron originates the photon conversion. Others are from the heavy flavor or light flavor jets.

[*3]The transverse momentum selection is defined so that the turn-on curve of electron trigger reaches a plateau at the offline selection point.

$p_T > 20$ GeV[*4] and $|\eta| < 2.5$ (see Figure 5.8(a)). The isolation condition of muons is defined with the following three parameters: E_T deposited in the calorimeter cells within $\Delta R < 0.3$ around the muon (*etcone*) (see Figure 5.8(b)), sum of p_T of tracks with $p_T > 1$ GeV within $\Delta R < 0.3$ around the muon, referred to as "*ptcone*" hereafter, and the distance between the muon and the closest reconstructed jet with $p_T > 20$ GeV ($\Delta R(\mu, \text{jet})$). The requirements are: *etcone* < 4 GeV, *ptcone* < 4 GeV, and $\Delta R(\mu, \text{jet}) > 0.4$.

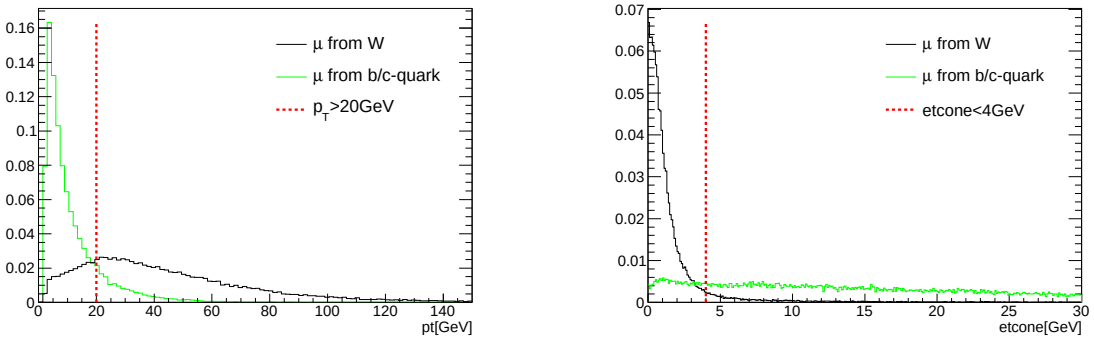

(a) (b)

Figure 5.8: The p_T and *etcone* distributions of reconstructed muons for signals and backgrounds, respectively. They are evaluated using signal and background muons contained by the simulation sample of $t\bar{t}$ events.

Jet identification

Jets are reconstructed with distance parameter $\Delta R = 0.4$ with the "anti-k_t algorithm", as shown in Section 3.2.4. The full calibration of the four momentum of the jets are used by default in the jet selection. Jets satisfying $p_T > 25$ GeV and $|\eta| < 2.5$ are considered to be high-p_T jets in the analysis. To avoid the double counting of the calorimeter clusters, if a jet is overlapped with a selected electron, the jet is discarded in the analysis.

Missing transverse energy (E_T^{miss}) measurement

The missing transverse energy E_T^{miss} is used as a signature of the undetected neutrino with high p_T. The missing transverse energy is constructed from the vector sum of transverse momentum of reconstructed jets, muons, and electrons, as well as calorimeter energy deposits not associated with reconstructed objects. For the jets with $p_T > 20$ GeV, the transverse momentum is fully calibrated, as described in Section 3.2.4, while the jets with $p_T < 20$ GeV are calibrated with the electromagnetic scale. The components of jets with the low p_T are called "softjets" term.

[*4]The transverse momentum selection is defined so that the turn-on curve of muon trigger reaches a plateau at the offline selection point.

The missing transverse energy is described numerically with the following equations:

$$E_{Tx}^{miss} = -(\sum_{\text{electrons}} p_x + \sum_{\text{muons}} p_x + \sum_{\text{jets}} p_x + \sum_{\text{softjets}} p_x + \sum_{\text{cellout}} p_x) \tag{5.4}$$

$$E_{Ty}^{miss} = -(\sum_{\text{electrons}} p_y + \sum_{\text{muons}} p_y + \sum_{\text{jets}} p_y + \sum_{\text{softjets}} p_y + \sum_{\text{cellout}} p_y) \tag{5.5}$$

$$E_{T}^{miss} = \sqrt{(E_{Tx}^{miss})^2 + (E_{Ty}^{miss})^2}. \tag{5.6}$$

In the equations, the "cellout" means calorimeter energy deposits not associated with reconstructed objects.

5.3.2 Detector performances evaluation

Measurements of detector performances related to the $t\bar{t}$ cross-section analysis are discussed in this section. They enable to estimate the signal acceptance and the backgrounds with consideration of the real detector performances. In particular, the measured performances are compared with those of MC simulation and the MC simulation is corrected to reproduce the real detector performance.

Performance evaluation for the electron objects

Efficiency of the electron measurements The efficiency of the electron detection can be measured in the $Z \to ee$ physics process, which includes two isolated electrons with high p_T. The efficiencies for the trigger, the reconstruction, the identification, and the isolation cut for the electron selection are measured with a common technique, which is so-called "tag-and-probe" method[*5]. Its concept is to select the $Z \to ee$ events with the following conditions:

- Require one electron with tight conditions[*6]
- Require one electron with loose conditions
- Require the invariant mass of the electron pairs in the Z mass window.

The first electrons are called "tag electrons", and the second electrons are called "probe electrons". The definition of the "tag" and "probe" electrons is defined so that the probe electrons are free from the selection bias in the efficiency measurements. Therefore, the tag and probe definitions are different for each of efficiency measurements as summarized in Table 5.2. The probe electrons are used to measure the efficiencies of the selections.

The measurements are performed both for the collision data ($Z \to ee$ enhanced samples) and the $Z \to ee$ simulation samples to compare the performance between data and simulation. The correction factors to match the simulated performance to the real situation are produced as scale factors $SF \equiv \frac{\epsilon_{\text{data}}}{\epsilon_{\text{MC}}}$ by the comparison between data and MC, where ϵ_{data} and ϵ_{MC}

[*5]The reconstruction and isolation conditions are summarized in Section 3.2.3, and the isolation selections are summarized in Section 5.3.

[*6]All the identification and isolation selection is included.

Measurements	Requirement for tag	Requirement for probe
Trigger	All the electron selections Trigger matching	All the electron selections
Reconstruction	Same above	The condition in the seed selection in the reconstruction (Only for the EM clusters)
Identification	Same above	Track and EM cluster matching Loose track quality cuts
Isolation	Same above	All the electron selections except for isolation cuts

Table 5.2: Definition of the tag and probe electrons for the efficiency measurements. The "Trigger matching" denotes a condition that the selected objects are associated with the determination given by the trigger system.

represent measured efficiency with the collision data and the simulation data respectively. The details of the application of the scale factors to the analysis are discussed in Appendix D.1.

The trigger efficiency measurement makes use of a definition with respect to the electrons that pass all the selections. The measured trigger efficiency in the collisions are shown in Figure 5.9. The measured trigger efficiency at the plateau is $\approx 98\%$ and in good agreement with the simulated efficiency. The scale factors are evaluated in 18 bins for η of the electrons. The measured SF is varying from 0.97 to 1.00 depending on the η, with a typical uncertainty of 0.5%.

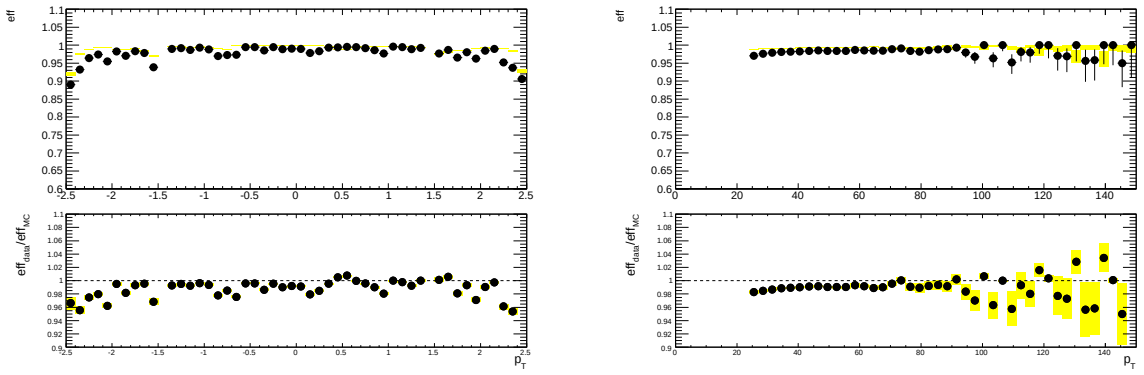

(a) (b)

Figure 5.9: The measured trigger efficiency in the collision data as a function of (a) η and (b) p_T of reconstructed electrons. The top figures show the measured trigger efficiencies in MC samples (yellow bands) and in collision data sample (closed circles). The bottom figures show the SFs and the yellow bands show a level of uncertainties in the SF determination.

The reconstruction, identification, and isolation efficiencies are measured and compared with the simulation respectively. The reconstruction efficiency is evaluated with 3 bins for η of the probe EM clusters, and the identification and the isolation efficiencies are evaluated with 90 bins for η and E_T of the reconstructed electrons ($\eta \times E_T = 18 \times 5$). In total, the scale factors are evaluated to be consistent to 1.0 with a typical uncertainty of 3%. The identification

and isolation efficiencies are found to be robust for the pileup difference, and the effect on the efficiency of the pileup is confirmed to be less than 0.1%.

Electron energy calibration Measurements of the electron energy scale and resolution, in a kinematic range comparable to that of electrons in the $t\bar{t}$ events, are derived from the measurement of the $Z \to ee$ invariant mass distribution. The energy scale is corrected in data as a function of the electron η (26 central and 6 forward bins) and systematic uncertainties are within $\pm 1.5\%$ for the $|\eta| < 2.5$ range, dominated by uncertainties from the detector material and the presampler energy scale. Uncertainties originating from the choice of event selections for Z samples, pileup effects, and hardware modeling are also taken into account as source of systematic uncertainties. To reproduce the $Z \to ee$ invariant mass distribution observed in data, the additional smearing factors to MC are applied, which varies typically from 1.0% to 2.0% with an uncertainty of 0.5%. depending the η of electrons.

Performance evaluation for the muon objects

Efficiency of the muon measurements The muon trigger, reconstruction, and isolation selection efficiencies are measured with "tag-and-probe" method, which is introduced for the electron efficiency measurements. The trigger, reconstruction, and isolation efficiencies are evaluated respectively for muons and the definitions of the tag muons and probe muons are summarized in Table 5.3.

Measurements	Requirement for tag	Requirement for probe
Trigger	All the muon selections Trigger matching	All the muon selections
Reconstruction	Same above	Isolated ID tracks with track quality cuts.
Isolation	Same above	All the muon selections except for isolation cuts

Table 5.3: Definition of the tag and probe muons for the efficiency measurements.

The trigger efficiency is evaluated with respect to well-reconstructed muons, where more than 99% probe muons originate from $Z \to \mu\mu$ decays. The trigger efficiency is measured for muons with $p_T > 20$ GeV, with which the trigger turn on curve reaches a plateau. The efficiency is measured with 70 bins in η and ϕ of the reconstructed muons with a typical uncertainty of 1%. The measured efficiency is shown in Figure 5.10.

It is found that the muon trigger simulator does not work correctly. Therefore, the results of the muon trigger simulation are not used in the MC. The simulation samples are corrected directly by the measured trigger efficiency but not by the scale factors.

The reconstruction and isolation efficiency measurements are performed with respect to the probe muons defined in Table 5.3 respectively.

The reconstruction efficiency is measured with 20 bins in η and ϕ according to the structure of the muon detectors. The measured reconstruction efficiency is about 96% in total, and the scale factor is evaluated to be consistent to 1.0 with a typical uncertainty of 0.3% in each of the bins.

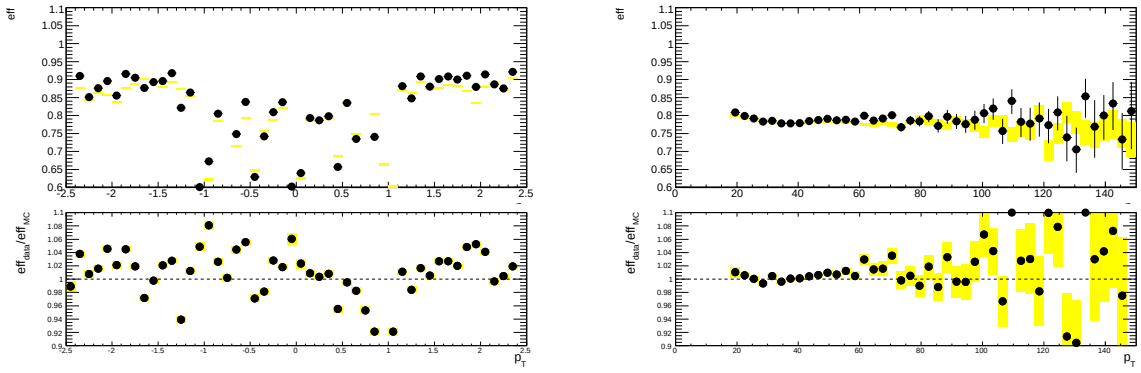

(a) (b)

Figure 5.10: The measured trigger efficiency in the collision data as a function of (a) η and (b) p_T of reconstructed muons. The top figures show the measured trigger efficiencies in MC samples (yellow bands) and in collision data sample (closed circles). The bottom figures show the SFs and the yellow bands show a level of uncertainties in the SF determination.

For the measurement of the isolation efficiency, it is found that the measured isolation efficiency is in good agreement with the simulated isolation efficiency regardless of the phase space of the reconstructed muons (p_T, η, ϕ) and the number of reconstructed jets. This means that the isolation efficiency measured in the Z control samples can be propagated into the $t\bar{t}$ events without binning, and the scale factor is evaluated to be consistent to 1.0 with an uncertainty of 0.03%. To check the pileup effect on that, the efficiency dependence on the number of reconstructed vertexes are shown in Figure 5.11. The ratio between data and simulation is constant for all the number of reconstructed vertexes, while the efficiency itself depends on the number of reconstructed vertexes. The results confirm that the isolation efficiency measured can be predicted correctly in the simulation as long as the pileup effect is properly corrected in MC simulations (see Section 5.2.3).

Muon momentum calibration The muon energy scaling and resolution is obtained by fitting $Z \rightarrow \mu\mu$ resonance at 91 GeV with liner combination of Breit-Wigner term (weak component), QED term, and the interference term. The energy scale ratio between data and MC is evaluated to be very close to 1.0 within a typical uncertainty of 1.0% for the entire detector region.

The Z peak of the two muon invariant mass is sensitive to possible shifts in the momentum scale, and the mass resolution can be used to determine the muon momentum resolution. The resolution is parametrized with the effect of (1) multiple-scatterings in calorimeter material, (2) spacial resolution of the individual track points, and (3) internal alignment of the inner detector system and muon spectrometer system. The first term is proportional to ${p_T}^{-1}$, the second term does not depend on p_T, and the third term is proportional to p_T, and then the three components could be separated by checking the resolution as a function of p_T of reconstructed muons. These values are estimated for both data and MC, and resolution a bit worse in the collision data than the MC is found. To reproduce the real resolution of the muon spectrometer

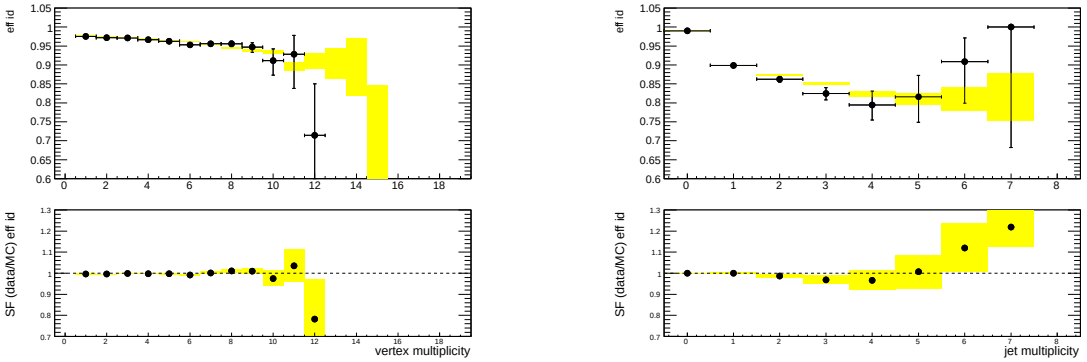

(a) (b)

Figure 5.11: The isolation efficiency comparison between real detector performance and prediction in the simulation as a function of (a) number of vertexes, which corresponds to number of pileup interaction, and (b) number of jets. The measured efficiency in collision data is shown with closed circle, and the simulated efficiency is shown with yellow band in the figures.

in the MC, the muon p_T is smeared by 1% - 3%, depending on the muon p_T and η with a typical uncertainty of $\approx 0.5\%$.

Performance evaluation for the jet objects

Efficiency of jet measurements The reconstruction efficiency of the calorimeter jets is derived using the "tag-and-probe" technique in 2-jets control samples. The probe jets to be used in the efficiency measurement are found as clusters of the charged tracks reconstructed by the ID system (i.e. not using the calorimeter clusters) so-called "track-jets". The measured jet reconstruction efficiency are in good agreement between the collision data and the MC. The efficiency is found to be consistent to 1.0 within an uncertainty of $\approx 2\%$. Therefore, no correction of the jet efficiency is applied to simulation studies in the $t\bar{t}$ cross-section analysis.

Jet energy reconstruction The jet energy resolution is measured with a p_T balance in di-jet systems, and those of the data and the MC agree with each other within 10%. Therefore, no additional correction is applied for the jet energy resolution in the MC simulation study.

For the energy scale of the jets, since no simple control sample to evaluate the jet energy scale can be defined, the jet energy scale evaluated by the simulation is used in the analysis without additional correction, and a large uncertainty is applied to the jet energy scale. The uncertainties are estimated from the following inputs: in-situ and single pion test-beam measurements, uncertainties on the material budget of the ATLAS detector, the description of the electronic noise, and the simulation modeling used in the event generation [35]. The uncertainties vary, depending on E_T and η of the jets. For jets reconstructed in central region ($|\eta| < 0.8$) with high $p_T(> 80$ GeV), the uncertainty is less than 2.5%, while the uncertainty is about 14% for jets reconstructed in forward region ($|\eta| > 3.2$) with low $p_T(< 30$ GeV). The uncertainties are shown as function of p_T of reconstructed jets in Figure 5.12. Adding to this, we estimated additional jet energy scale uncertainties related to the pileup effect. The pileup uncertainty in

the central region $0 < \eta < 2.1$ is 5% for jets within $20 < p_T < 50$ GeV and 2% in the range $50 < p_T < 100$ GeV. For forwards jets within $2.1 < \eta < 4.5$ the estimated pileup uncertainty is 7% for jets within $20 < p_T < 50$ GeV and 3% in the range $50 < p_T < 100$ GeV.

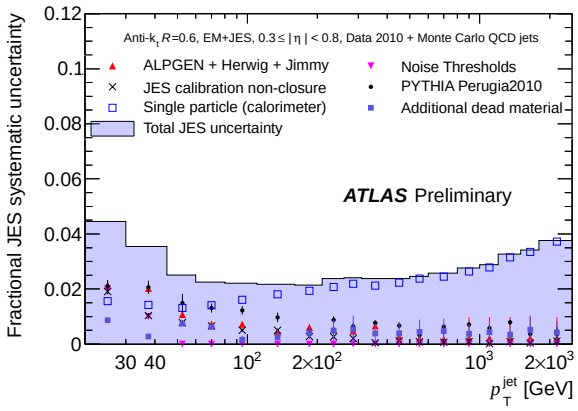

Figure 5.12: Fractional jet energy scale systematic uncertainty as a function of jet p_T in the region with $0.3 < |\eta| < 0.8$, where the uncertainty is smallest in the angle. The total uncertainty is shown as the solid light blue area. The individual sources are also shown [35].

5.4 Systematic uncertainties

Systematic uncertainties considered in the cross-section measurements are described in this section. The following sources are taken into account in the analysis:

- Uncertainty of the luminosity evaluation (3.7%)
- Uncertainty related to the simulation samples (the simulation statistics and models in the simulation)
- Uncertainty of the detector performances
- Uncertainty in the background estimation.

These systematic uncertainties taken into account in the analysis are explained in the following sections and summarized in Table 5.4.

5.4.1 Simulation-related uncertainties

Statistical uncertainties of the simulation samples The statistical uncertainty of the simulation samples is evaluated by the Poisson errors according to the number of events after applying all the criteria.

Uncertainty of the Monte Carlo generator The uncertainty from a choice of the $t\bar{t}$ MC generator has been estimated by comparing the acceptance estimations between different two $t\bar{t}$ event generators: the nominal MC@NLO and the POWHEG [36, 37, 38]. Both MC generator employ the NLO approximation of the p-QCD (see Section 2.2.2 and 5.2.2).

Uncertainty of parton shower simulation The uncertainty from a choice of the parton shower simulation for the $t\bar{t}$ MC has been estimated by comparing the acceptance estimations between different two parton shower simulators: the nominal HERWIG and the PYTHIA [39] (see Section 2.3.3 and 5.2.2).

Uncertainty of the ISR and FSR effect The uncertainty due to ISR/FSR is evaluated using the ACERMC generator [40] interfaced to the PYTHIA shower model. For the ISR/FSR variation samples, the parameters introduced in the QCD calculation (see Section 2.2), such as the Λ_{QCD} scale and the p_T cut-off in the final state radiation, are varied so that the variations of parameters result in increased or decreased ISR / FSR, where its range is compatible to the past experimental results: hadronic Z decays in e^+e^- collisions, minimum bias collisions at $p\bar{p}$ collisions, and Drell-Yan production in $p\bar{p}$ collisions [41].

Uncertainty due to the PDF The uncertainty from a choice of a set of PDF in the $t\bar{t}$ acceptance estimation has been estimated by comparing the following sets of the PDF: CTEQ6.6 [10] (nominal), NNPDF2.0 [43], and MSTW2008 [44]. They are the most recent tuned PDF sets with the NLO approximation. Additionally parameters employed in the PDF calculations are varied with a range compatible to their uncertainty of 1σ, and the residuals are taken into account as the systematic uncertainty related to the PDF.

Uncertainty due to Z p_T distribution uncertainties For the Z+jets samples, distributions of the p_T of Z bosons is varied in a range which is consistent with experiments, and the variation of the estimation is taken into account as the systematic uncertainties.

Uncertainty from the theoretical MC cross-section The overall normalization uncertainties on the backgrounds from the single t-quark and the diboson production are taken to be 8.6% [31] and 5% [45], respectively.

5.4.2 Detector-performance-related uncertainties

The uncertainties of detector performance estimations are discussed in Section 5.3.2. It is possible to emulate the $\pm 1\sigma$ shift with respect to the nominal performance except for the uncertainties for the jet reconstruction efficiency (JEF) and the jet energy resolution (JER). The residuals of the cross-section measurements according to the shift are treated as systematic uncertainties. For estimating the uncertainties related to jet reconstruction efficiency in the MC, the small difference ($< 0.4\%$) is applied to the MC by randomly dropping a fraction of jets, and the difference in final results are applied as systematic uncertainties. The uncertainties of the jet energy resolution is evaluated by applying worse resolution by $+1\sigma$ to the simulation

and evaluate the residual as an uncertainty from the error of the jet energy resolution modeling. In these uncertainty evaluations, the modifications of the jet and lepton energies are correctly propagated into E_T^{miss} calculation.

Uncertainties	Notation
LHC	
Uncertainty of the luminosity measurement	Lumi
Monte Carlo Simulation and Signal Modeling	
Statistical uncertainties of the simulation samples	Stat(MC)
Uncertainty of the Monte Carlo generator	Generator
Uncertainty of parton shower simulation	P.Shower
Uncertainty of the ISR and FSR effect (Uncertainty in tuning QCD parameters in the simulation)	ISR/FSR
Uncertainty due to the parton distribution uncertainties	PDF
Uncertainty due to Z p_T distribution uncertainties	Z p_T
Uncertainty from the theoretical MC cross-section	x-sec(Theory)
Detector Modeling	
Uncertainty of the jet energy scale	JES
Uncertainty of the jet resolution	JER
Uncertainty of the jet reconstruction efficiency	JEF
Uncertainty of E_T^{miss} calculation due to pile-up uncertainties	MET(PileUp)
Uncertainty of the softjet and the cellout term of E_T^{miss} calculation	MET(SoftJet)
Uncertainty of the lepton identification efficiency evaluation	SF(Mu./El.ID)
Uncertainty of the lepton trigger efficiency evaluation	SF(Mu./El.Trig)
Uncertainty of the lepton energy scale	Mu.ES/El.ES
Uncertainty of the lepton energy resolution	Mu.ER(MS/ID) El.ER(MS)
Data-driven Background Evaluation	
Uncertainty from the fake evaluation	Fake
Uncertainty from the data-driven Drell-Yan evaluation	DY

Table 5.4: Summary of the uncertainties evaluated in the analysis.

5.5 Event selection

Considering the properties of the final states described in Section 5.1, the $t\bar{t}$ signal events are extracted with signature defined with two leptons, two or more than two jets, and large E_T^{miss}. The event selections and their optimization studies to minimize errors of cross-section measurements are explained in the following sections.

5.5.1 Event quality cut

Before series of event selection criteria dedicated to selecting $t\bar{t}$ events, several unqualified events are discarded to ensure the analysis quality. As discussed in Section 5.2.1, the quality cuts for the detector and the LHC operation are applied first. Adding to them, the following set of event quality cuts to reject bad events is applied:

- Non-collision background rejection
- Jet cleaning.

In order to reject events triggered by cosmic-ray muons, which do not originate from pp collisions, events having reconstructed cosmic-ray muons are rejected. The cosmic-ray muons are identified as muon pairs satisfying following conditions: reconstructed transverse impact parameters d_0 of two muons are oppositely-charged, fulfill $|d_0| > 0.5$ mm[*7], and satisfy $\Delta\phi > 3.10$ rad between the two muon's directions. The impact parameter d_0 is calculated with respect to the primary vertex in the events. Furthermore, we require that events include at least one good vertex, which is defined as a vertex to which at least five tracks belong (Non-collision background rejection). Events are discarded if any jet with $p_T > 20$ GeV fails jet quality cuts that are designed to reject jets arising from the out-of-time activities[*8] or the calorimeter noise backgrounds (Jet cleaning) since such jets are not physical-meaningful and result in the worse resolution of the E_T^{miss}. The out-of-time activities can be identified by the detection timing with respect to the pp crossing (t; $|t| > 25$ ns) and the momentum fraction of the charged particles associated with the jets (F; $F < 0.05$). Further, if the pulse of calorimeter output differs from prediction (i.e. strange pulse shape and fraction of the energy at the cell), it is considered to be from the calorimeter noise backgrounds.

5.5.2 Selection with kinematic variables

Each event is required to contain exactly two reconstructed oppositely-charged lepton candidates: ee, $\mu\mu$, or $e\mu$. The selection of $t\bar{t}$ candidate events in the dilepton final states consists of a series of kinematic requirements on the E_T^{miss}, the invariant mass of $\mu\mu$ and ee ($M_{\ell\ell}$), the scalar sum of the transverse momentum of the selected jets and leptons (H_T), and the number of selected jets (N_{jets}). In order to suppress backgrounds from Z/γ^*+jets and QCD multi-jet events in the ee and $\mu\mu$ channels, E_T^{miss} is required to be larger than 60 GeV, and the invariant mass of the two leptons must be greater than 15 GeV. Furthermore, to reject Z+jets events effectively, the invariant mass of the two leptons is required to differ from the Z-boson mass of 91 GeV by at least 10 GeV. For the $e\mu$ channel, the event H_T must satisfy $H_T >$ 130 GeV. Additionally it is required that there are at least two reconstructed jets for all three channels. Distributions of these kinematic variables are shown in Figure 5.13.

These selection criteria are optimized to minimize the uncertainties on the cross-section measurement, which include the statistical uncertainty of N_{data}, the uncertainty of the acceptance estimation, and the uncertainty of the background estimation. Using the MC samples, the analysis is repeated with several sets of selection criteria, and the best set of selection criteria with which the sum of the uncertainties is minimized has been chosen. The detector performance[*9] and the pileup effect reproduced correctly in the simulation to match those in the collision data so that the real situation of the data taking is taken into account in the optimization results. Figure 5.14 shows the expected uncertainty as a function of the E_T^{miss}

[*7] The d_0 is signed transverse impact parameter, which is obtained by sum of the x, and y components of the impact parameters of the track with respect to the primary vertex.

[*8] They correspond to beam backgrounds or cosmic-ray backgrounds.

[*9] This is discussed in Section 5.3.2.

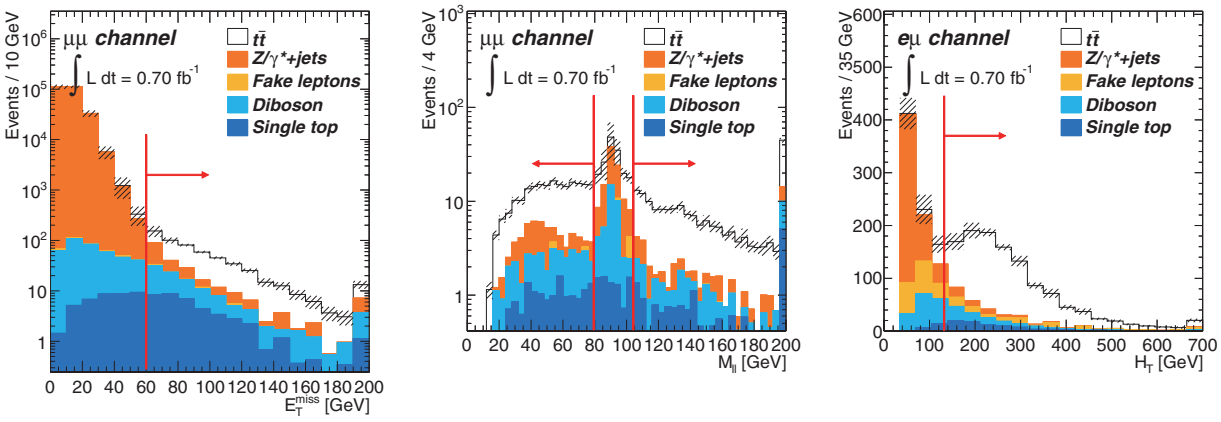

(a) (b) (c)

Figure 5.13: Expected distributions of kinematic variables that are used to extract the $t\bar{t}$ signals. The red lines and arrows correspond to the used cut values in the analyses. (a) E_T^{miss} distribution after applying the $\mu\mu$ requirements. (b) Invariant mass distribution of the two selected muons after the $E_T^{miss} > 60$ GeV cut application. The E_T^{miss} requirements and Z mass veto cuts are applied to ee and $\mu\mu$ channels to reject the large contributions $Z \to \ell\ell$ events. (c) H_T distribution after the $e\mu$ requirement. This cut is applied to reject backgrounds mainly from the $Z/\gamma^* \to \tau\tau$ process.

cut points and the p_T threshold in counting number of jets. The criteria described above have been chosen as optimal selection criteria. By the application of the optimized event selection to the pp collision data, 165 events, 301 events, and 963 events are selected in ee, $\mu\mu$, and $e\mu$ final states, respectively. Table 5.5, Table 5.6, and Table 5.7 summarize the selection flows of the collision data, and the MC expectation of each of the physics processes for ee, $\mu\mu$, and $e\mu$ channels, respectively, except for the "fake leptons" backgrounds which is determined by a data-driven technique (see Section 5.6.2).

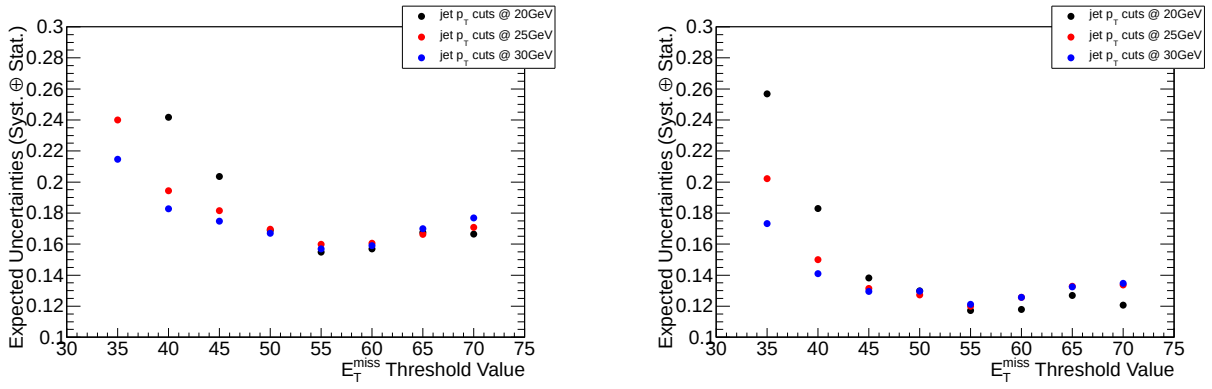

Figure 5.14: Uncertainty dependence on the E_T^{miss} and jet pT threshold. The x-axis correspond to the threshold of the E_T^{miss} cut, and the different color of the points corresponds to the threshold of the jet p_T in counting number of jets. It is found that high E_T^{miss} threshold (more than 55 GeV) enables a significant reduction of the background contamination, and uncertainties from background estimation in the cross-section measurements. Based on these findings, the E_T^{miss} threshold is determined to be 60 GeV for both ee and $\mu\mu$ channels, and the 25 GeV threshold of jet p_T in counting number of jets is chosen.

	$t\bar{t}$	DY (ee, $\mu\mu$)	DY ($\tau\tau$)	Diboson ($\ell\ell$)	$Wt(\ell\ell)$	Total	data
Cross-Section (pb)	1.65×10^2	1.01×10^4	5.06×10^3	7.61	1.01		7.15×10^{10}
Total	1.15×10^5	7.07×10^6	3.53×10^6	5.31×10^3	7.07×10^2		4.99×10^{13}
≥ 2 leptons	362.4	124725.7	103.0	262.3	38.9	125492.2	133297
LAr cleaning	341.6	123059.9	102.0	252.9	37.2	123793.6	131082
$E_T^{miss} > 60$ GeV	180.8	139.8	7.8	39.2	16.5	384.2	462
$N_{\text{jets}} \geq 2$	150.0	37.6	4.9	12.7	8.2	213.4	236
$= 2$ leptons	149.9	37.6	4.9	11.4	8.2	212.0	235
Opposite sign	148.9	36.9	4.9	10.3	8.0	209.0	233
$M_{\ell\ell} > 15$ GeV	147.9	36.8	4.9	10.2	7.9	207.7	229
$\lvert M_{\ell\ell} - M_Z \rvert > 10$ GeV	124.9	4.7	4.9	5.9	6.4	146.8	165
Truth matching	124.0	4.7	4.9	5.9	6.4	145.8	

Table 5.5: Expectation of the selected events in the ee final state. The first cut ("≥ 2 leptons") includes standard selections such as the trigger requirement and the event level cut in this table as well as in Table 5.6 and 5.7. The "truth matching" in the tables are requirement that the selected two leptons in the MC samples should originate from the W/Z decays to avoid the double counting in the "fake lepton background" evaluation (see Section 5.6.2).

5.5.3 Signal acceptance

The signal acceptance is estimated by the MC simulation with MC@NLO generator interfaced by Herwig parton shower simulator. The detector performances, such as electron and muon energy scaling, resolution, and detection efficiency, are calibrated according to the performance

	$t\bar{t}$	DY (ee, $\mu\mu$)	DY ($\tau\tau$)	Diboson ($\ell\ell$)	$Wt(\ell\ell)$	Total	data
Cross-Section (pb)	1.65×10^{2}	1.01×10^{4}	5.06×10^{3}	7.61	1.01		7.15×10^{10}
Total	1.15×10^{5}	7.07×10^{6}	3.53×10^{6}	5.31×10^{3}	7.07×10^{2}		4.99×10^{13}
≥ 2 leptons	660.0	256786.7	601.8	493.1	85.7	258627.3	270485
LAr cleaning	624.5	254527.2	597.1	477.7	82.3	256308.8	267594
$E_T^{miss} > 60$ GeV	345.7	105.5	19.7	82.1	41.7	594.7	627
N_{jets}	286.5	53.8	11.0	22.3	19.3	393.0	403
$= 2$ leptons	286.5	53.8	11.0	19.8	19.3	390.4	401
Opposite sign	286.5	53.2	11.0	18.5	19.3	388.6	400
$M_{\ell\ell} > 15$ GeV	284.1	53.0	11.0	18.4	19.0	385.6	394
$\lvert M_{\ell\ell} - M_Z\rvert > 10$ GeV	241.3	16.3	11.0	8.7	16.0	293.3	301
Truth matching	241.3	16.3	11.0	8.7	16.0	293.3	

Table 5.6: Expectation of the selected events in the $\mu\mu$ final state.

	$t\bar{t}$	DY ($\tau\tau$)	Diboson ($\ell\ell$)	$Wt(\ell\ell)$	Total	data
Cross-Section (pb)	1.65×10^{2}	5.06×10^{3}	7.61	1.01		7.15×10^{10}
Total	1.15×10^{5}	3.53×10^{6}	5.31×10^{3}	7.07×10^{2}		4.99×10^{13}
≥ 2 leptons	977.8	519.1	286.0	107.2	1890.0	2372
LAr cleaning	923.9	515.2	280.4	102.6	1822.1	2289
$H_T > 130$ GeV	888.1	70.2	130.1	85.9	1174.4	1300
N_{jets}	753.2	43.9	43.5	41.5	882.2	990
$= 2$ leptons	753.0	43.9	38.8	41.6	877.3	986
Opposite sign	749.4	43.6	33.1	41.4	867.6	963
Truth matching	745.6	42.5	32.9	41.1	862.1	

Table 5.7: Expectation of the selected events in the $e\mu$ final state.

measurements mainly done in the Z control region. The pileup effect in MC is corrected according by matching the $\langle\mu\rangle$ distribution between data and MC.

The signal acceptance that is normalized with respect to the sub-decay branching fractions is estimated to be 6.6%, 13.0%, and 20.0%, for ee, $\mu\mu$, and $e\mu$ channels, respectively. The acceptance of each channel originates mainly from (1) the lepton selection efficiency, (2) the E_T^{miss} selection efficiency for ee and $\mu\mu$ channel, (3) the H_T selection efficiency for $e\mu$ channel, (4) efficiency of the Z events veto cut ($|M_{\ell\ell} - M_Z| < 10$ GeV in ee, and $\mu\mu$ channels) and (5) the efficiency of the jet multiplicity requirement. The difference between them originate mainly from difference of (1), (2), and (3). Selection efficiencies at the individual criteria are summarized in Appendix D.2. These values of signal acceptance are estimated with relative uncertainties of $\pm13.9\%$, $+6.0\%/-7.4\%$, and $+5.4\%/-5.8\%$ for ee, $\mu\mu$, and $e\mu$ channels, respectively. The details of uncertainties estimation are in Table 5.8.

	ee (%)	$\mu\mu$ (%)	$e\mu$ (%)
$\mathcal{A}/BF$	6.6%	13.0%	20.0%
	$\Delta\mathcal{A}_{ee}/\mathcal{A}_{ee}$	$\Delta\mathcal{A}_{\mu\mu}/\mathcal{A}_{\mu\mu}$	$\Delta\mathcal{A}_{e\mu}/\mathcal{A}_{e\mu}$
Stat(MC)	±1.4	±0.9	±0.6
Z pT	±0.0	±0.0	±0.0
JES	+7.2/-7.4	+4.7/-5.9	+1.9/-2.7
JER	±1.3	±0.4	±0.1
JEF	±0.1	±0.0	±0.0
MET(SoftJet)	-0.3/+0.6	-0.3/+0.2	±0.0
MET(PileUp)	-0.4/+0.4	-0.2/+0.2	±0.0
LAr(JetCleaning)	+0.6/-0.8	+0.5/-1.1	+0.6/-1.0
SF(Mu.ID)	±0.0	+1.1/-1.1	+0.6/-0.6
SF(Mu.Trig)	±0.0	+0.2/-2.2	+0.0/-0.1
SF(El.ID)	+5.2/-5.1	±0.0	+2.6/-2.6
SF(El.Trig)	±0.0	±0.0	±0.0
Mu.ES	±0.0	+0.1/-0.0	±0.0
Mu.ER(MS)	±0.0	-0.1/+0.1	±0.0
Mu.ER(ID)	±0.0	+0.0/-0.1	±0.0
El.ES	+0.7/-0.2	±0.0	+0.2/-0.2
El ER	+0.2/+0.1	±0.0	±0.0
P.Shower	±4.6	±0.8	±2.9
Generator	±2.5	±0.0	±0.9
ISR	+3.3/-3.3	+0.6/-0.6	+1.0/-1.0
FSR	+8.0/-8.0	+2.4/-2.4	+1.3/-1.3
PDF	±2.5	±2.1	±2.4
Syst(total)	+13.9/-13.9	+6.0/-7.4	+5.4/-5.8

Table 5.8: The estimated acceptance values and their uncertainties for the ee, $\mu\mu$, and $e\mu$ channels. Note that the signal acceptance is normalized with respect to the sub-decay branching fractions in order to compare the selection efficiencies between channels.

5.6 Background rate estimation

The background contribution is estimated, by collision data sample whenever possible in order to minimize the reliance on the MC. There are three categories of background sources:

1. Backgrounds from $Z/\gamma^* \to e^+e^-,\ \mu^+\mu^-$ (Drell-Yan (DY) processes) produced with associated jets and with large E_T^{miss} due to resolution effects and measurement errors. $Z/\gamma^* \to e^+e^-,\ \mu^+\mu^-$ is the main background source for the ee and $\mu\mu$ channels.

2. Processes that contain non-prompt leptons and hadrons misidentified as leptons. They are referred as "fake" leptons. Fakes enter the sample in events with W bosons produced in association with jets, and QCD multi-jet events. In case of W+jets events, one lepton is a real prompt lepton from the W decay, and the second is a fake lepton mimicked by one of the jets. In the case of QCD multi-jet events, both leptons are fakes.

3. Other background sources originating from electroweak processes including two leptons and neutrinos in their final states such as $Z/\gamma^* \to \tau^+\tau^- \to \ell^+\ell^- + 4\nu$, single top ($Wt$), and diboson ($WW$, ZZ and WZ) production processes.

The DY and fake lepton backgrounds are determined using control data samples to minimize uncertainties in the modeling of the MC. These methods and results are described in the following sections (see Section 5.6.1 and Section 5.6.2). Control data samples that are used to estimate the backgrounds are orthogonal to those used in the signal extractions. Parameter spaces corresponding to control data samples are referred as "control region", and those corresponding to the signal extraction are referred as "signal region".

For other background sources that are listed the third categories, the contributions are estimated with respect to the cross-section predicted by the SM theory (see Section 5.6.3).

5.6.1 Drell-Yan background

The $Z/\gamma^* \to ee$ and $\mu\mu$ events are significantly suppressed by the E_T^{miss} requirement and Z mass window cuts. However, DY events in the E_T^{miss} tails and the dilepton invariant mass sidebands may be selected. These events are difficult to model properly in the simulation due to the uncertainties in the non-Gaussian nature of the E_T^{miss} tails and the Z+jets cross-section with higher jet multiplicity.

To estimate the $Z/\gamma^* \to \ell\ell$ background in the ee and $\mu\mu$ channels with correct treatment of the E_T^{miss} tails, the scaling factors for the MC prediction is measured in a Z/γ^* control region to match the observed numbers in the collision data in the E_T^{miss} tails. The control region to estimate the normalization factors is formed by events with the invariant dilepton mass satisfying $|M_{\ell\ell} - M_Z| < 10$ GeV, with at least two jets and with $E_T^{miss} > 30$ GeV. Therefore, the control region is orthogonal to the signal region that require $|M_{\ell\ell} - M_Z| > 10$ GeV (see Figure 5.15). In the control region, the purity of the $Z/\gamma^* \to \ell\ell$ events are more than 90%, and the contamination from some non-Z background physics processes is subtracted using a MC prediction. Figure 5.16 shows the comparison of E_T^{miss} measurements between data and MC in the control regions for ee and $\mu\mu$ final states.

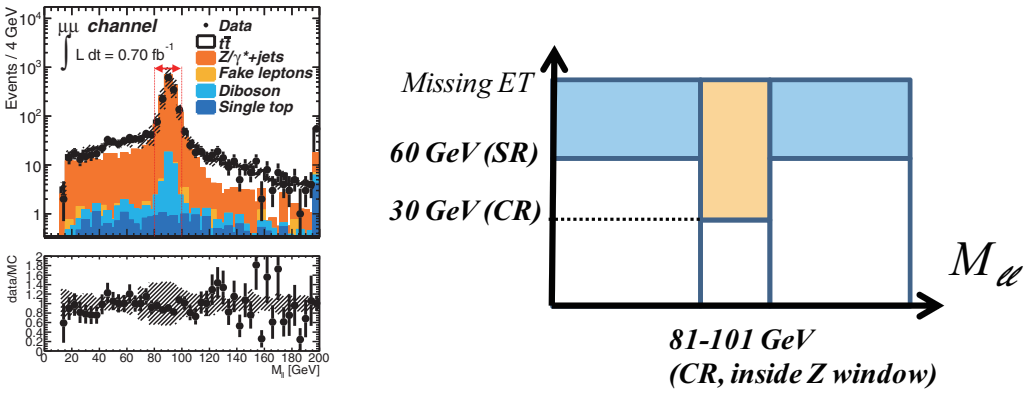

Figure 5.15: The control region definition to extract the scaling factor for DY background. The left figure shows the distribution of the dilepton invariant mass in events with $E_T^{miss} > 30$ GeV, and inside the Z mass window (81 GeV $< M_{\ell\ell} <$ 101 GeV) is defined as control region. The right figure shows the definition of the control region and the signal region. The control region is defined in side Z mass with $E_T^{miss} > 30$ GeV, which is orthogonal to the signal region defined outside Z mass window.

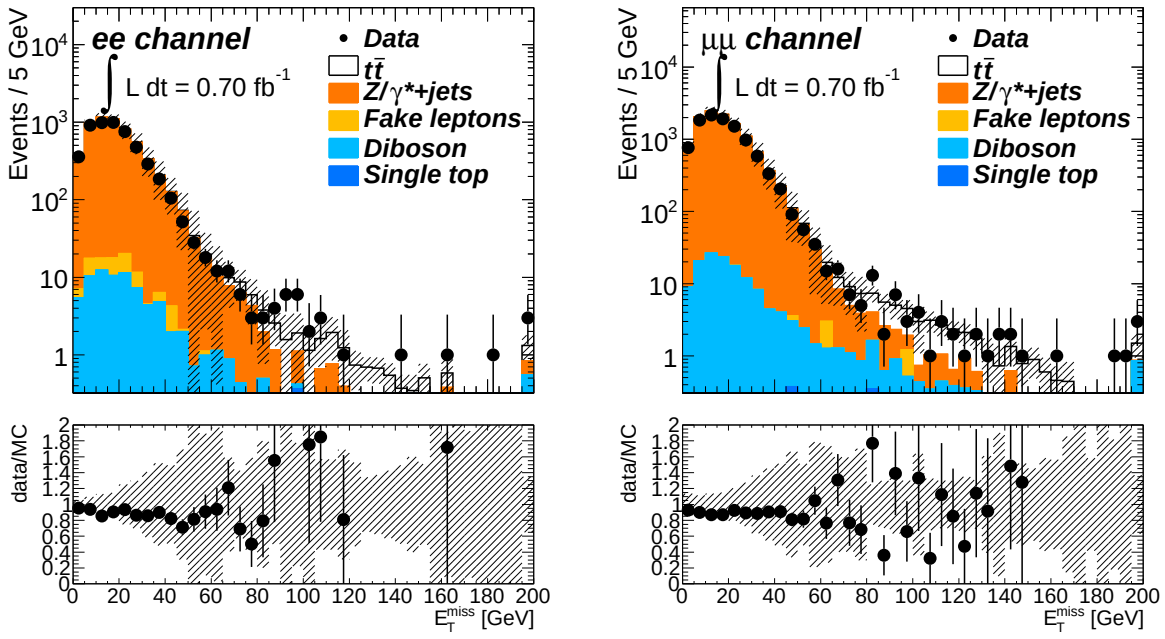

(a) (b)

Figure 5.16: E_T^{miss} distributions after requiring $N_{\text{jets}} \geq 2$ and $|M_{\ell\ell} - M_Z| < 10$ GeV. The tail components of the E_T^{miss} measurements for Z/γ^* are calibrated with respect to the results of comparison between data and MC in the control region samples with Equation 5.7.

According to the scaling factor that are measured in the control region, the MC prediction in the signal region are scaled with the following equation:

$$SR_{\mathrm{DY}} = \frac{CR^{\mathrm{data}} - CR^{\mathrm{MC}}_{\text{non DY}}}{CR^{\mathrm{MC}}_{\mathrm{DY}}} \times SR^{\mathrm{MC}}_{\mathrm{DY}} \tag{5.7}$$

where the $SR^{\mathrm{MC}}_{\mathrm{DY}}$ and $CR^{\mathrm{MC}}_{\mathrm{DY}}$ represents the MC expectation of the number of DY events in the signal and control region, respectively. The $CR^{\mathrm{MC}}_{\text{non DY}}$ is the number of events from non-Z backgrounds that pollute the control region. The CR^{data} represents the observed number of events in the control region in 0.70 fb^{-1} of collision data. The observed and expected numbers in the control and signal regions are summarized in Table 5.9 for the ee and $\mu\mu$ channels.

		DY sources		Other physics processes in the CR					
Channel	CR^{data}	$CR^{\mathrm{MC}}_{\mathrm{DY}}$	$SR^{\mathrm{MC}}_{\mathrm{DY}}$	$t\bar{t}$	$Z\tau\tau$	W/Z fake	diboson	single top	Total
ee	740	798.1	4.7	35.9	0.0	10.7	18.8	2.2	67.6
$\mu\mu$	1397	1459.1	16.3	66.9	0.1	0.0	32.1	4.3	103.4

Table 5.9: Number of observed events in data in the control region, the number of MC events in the signal and control regions and the number of events from other physics background sources contaminating the control region for DY backgrounds estimation in ee and $\mu\mu$ channel. W/Z fake includes contribution from W+jets samples and Z+jets where we do not have matching between offline selected leptons and truth leptons from Z.

The uncertainties on the estimation are summarized in Table 5.10. An additional uncertainty denoted by "Method" is shown in the table as well as the other uncertainties listed in Section 5.4. Dependence on the choice of the cut is tested by shifting the E_T^{miss} threshold in the control region. It has been found that the data-driven technique is very robust for the control region definition. Then variation according to ± 5 GeV shift of the E_T^{miss} threshold for the control region, which corresponds to the E_T^{miss} resolution, is applied as systematic uncertainties of the method. The data-driven technique is found to be able to reduce the uncertainty, comparing with the MC-driven prediction.

Adding to the signal region, the Z/γ^* scale factors are estimated for other parameter spaces. The events are categorized into six classes with reference to jet multiplicity ($N_{\mathrm{jets}} = 0$, $N_{\mathrm{jets}} = 1$, $N_{\mathrm{jets}} \geq 2$) and the E_T^{miss} ($E_T^{miss} < 30$ GeV or $E_T^{miss} > 30$ GeV). For all the 6 classes, the scale of the Z/γ^* is determined inside of Z mass window ($|m_{\ell\ell} - m_Z| < 10$ GeV), and the results are summarized in Table 5.12.

5.6.2 Fake lepton backgrounds

Leptons not from W/Z can be backgrounds also. The candidates are such as:

- Leptons from b- and c-quark decays (non prompt leptons)
- Jets mis-identified as leptons
- Fake electrons originating from photon conversions.

	ee (DD)	ee (MC)	$\mu\mu$ (DD)	$\mu\mu$ (MC)
Yield(events)	4.0	4.7	14.4	16.3
Uncertainty(%)				
Lumi	-0.4/+0.4	+3.7	-0.3/+0.3	+3.7
Stat(Data)	+4.2/-4.0	-	+3.0/-2.9	-
JES	-13.2/+26.4	+98.5/-18.1	-10.7/+28.6	+32.1/-4.4
JER	±5.0	±24.2	±18.5	±1.2
JEF	±0.1	±0.0	±0.1	±0.0
MET(SoftJet)	+34.7/-2.3	+36.1/-1.0	-7.5/-5.0	-5.4/-4.2
MET(PileUp)	+34.0/-1.8	+35.7/-1.0	-8.2/-4.1	-6.5/-4.2
LAr(JetCleaning)	-0.8/+1.6	+0.2/+0.0	-0.6/-0.8	+0.1/-2.5
SF(El.ID)	-0.4/+0.4	+5.4/-5.2	±0.0	±0.0
SF(El.Trig)	-4.1/+4.1	-4.1/+4.1	±0.0	±0.0
SF(Mu.ID)	±0.0	±0.0	±0.0	+1.2/-1.2
SF(Mu.Trig)	±0.0	±0.0	+0.0/+0.4	+0.2/-1.7
x-sec(Theory)	+1.2/-3.2	+33.2/-33.2	+3.4/-6.7	+34.6/-34.6
Stat(MC)	±24.9	±24.9	±13.4	±13.3
Z pT	±3.5	±4.0	±0.1	±0.1
El.ES	-5.9/+13.4	-6.6/+14.3	±0.0	±0.0
El.ER	+5.6/+11.3	+6.1/+11.5	±0.0	±0.0
Mu.ES	±0.0	±0.0	-0.1/+0.1	±0.0
Mu.ER(MS)	±0.0	±0.0	+2.5/-6.1	+2.6/-6.2
Mu.ER(ID)	±0.0	±0.0	+6.7/-3.5	+7.3/-4.0
Method	±0.2	-	±1.3	-
total($syst$+$lumi$+$stat$)	+63.7/-30.4	+122.5/-52.5	+37.6/-29.4	+49.8/-39.3

Table 5.10: Uncertainties in % on the predicted number of DY events in the signal region for dilepton events in $Z/\gamma^* \to ee$, $Z/\gamma^* \to \mu\mu$ channels, respectively. The uncertainties are compared between the data-driven (DD) determination and the determination by the MC (MC).

	ee	$\mu\mu$
DD	$4.0\ ^{+2.5}_{-1.2}$	$14.4\ ^{+5.4}_{-4.2}$
MC	$4.7\ ^{+5.8}_{-2.5}$	$16.3\ ^{+8.1}_{-6.4}$

Table 5.11: Estimates of the contamination from DY processes in the signal region of the $t\bar{t}$ analysis from both the data-driven method and from MC driven methods.

They are strongly suppressed by requirements of the isolation and the good qualities in lepton reconstructions, while they may pass the tight conditions of the lepton identification and are identified as "isolated leptons" with a small probability. The "fake" background rates are determined by a probability of such mis-identification (so-called "fake rate") for a jet or a non-prompt leptons. The background rates are estimated with following method based on the measured fake rate:

- Events containing two leptons are collected with loosened electron and muon selections (see Table 5.13). The samples enhance fraction of the fake lepton background, adding to

	$Z/\gamma^* \to ee$		$Z/\gamma^* \to \mu\mu$	
	$E_T^{miss} < 30$ GeV	$E_T^{miss} > 30$ GeV	$E_T^{miss} < 30$ GeV	$E_T^{miss} > 30$ GeV
$N_{\text{jets}} = 0$	1.08	0.81	1.06	0.77
$N_{\text{jets}} = 1$	1.00	0.89	0.99	0.85
$N_{\text{jets}} \geq 2$	0.89	0.84	0.89	0.89

Table 5.12: Estimated scale-factors for $Z/\gamma^* \to ee$ physics process for each of the parameter spaces defined by E_T^{miss}, and N_{jets} using the control samples inside Z mass. The factors for $Z/\gamma^* \to ee$ and $Z/\gamma^* \to \mu\mu$ are consistent with evaluation for each other within $\approx 3\%$. This is within the systematic uncertainties of electron measurements and muon measurements.

leptons from W/Z, which are referred as "true leptons" in this section.

- For evaluating the contamination of the fake backgrounds after the application of the tight selection, event-by-event weighting is applied to the loosened 2-lepton samples with reference to measured fake rates and measured efficiencies for true leptons.

electron	muon
loosened isolation cut ($etcone < 6$ GeV) loosened identification (condition on TRT etc.)	no isolation cut on *etcone* and *ptcone*

Table 5.13: The loose electrons and muons are defined by loosening the nominal object definition to select true leptons from $t\bar{t}$ decays (see Section 5.3).

Efficiency and fake rate evaluation

The efficiency and the fake rate defined with respect to the loose leptons are measured, using the $Z \to \mu\mu$ or $Z \to ee$ samples and the two jets enhanced control samples.

The efficiency for the true leptons is estimated by the "tag-and-probe" method introduced in Section 5.3.2. The two jets enhanced control samples to estimate the fake rates are selected with following requirements: (1) jets and (2) one loose lepton (the probe lepton) with a large opening angle ($dR > 0.7$)[*10]. For avoiding selecting the true leptons from W+jets events in the control samples, additionally $E_T^{miss} < 20$ GeV is required. Then the selected loose lepton is used to measure the fake rate. Furthermore, to measure fake rates for each of sources of the fake leptons, the probe loose leptons are categorized into following three categories to enhance different kind of fakes: (1) loose leptons to which the closest jet is identify as a jet originating from b-quark (b-tag control region)[*11], (2) loose leptons associated with photon conversion (*pc* control region), and (3) others.

[*10] The distance is defined between the highest p_T jet and the loose leptons.

[*11] A technique to identify b-flavor owing to its long life time is introduced here, so-called b-tagging. The significance of the distance between reconstructed secondary vertex of the b-jet and the primary vertex is calculated, which is the discriminant variable of the used b-tagging algorithm [46]

The measured fake rates are summarized in Figure 5.17. They are measured as a function of η and p_T for each of control samples in the two figures, respectively. Since no fake backgrounds originating from photon conversions are expected for the muons, the fake muon evaluation is performed with b-tag and the other control samples.

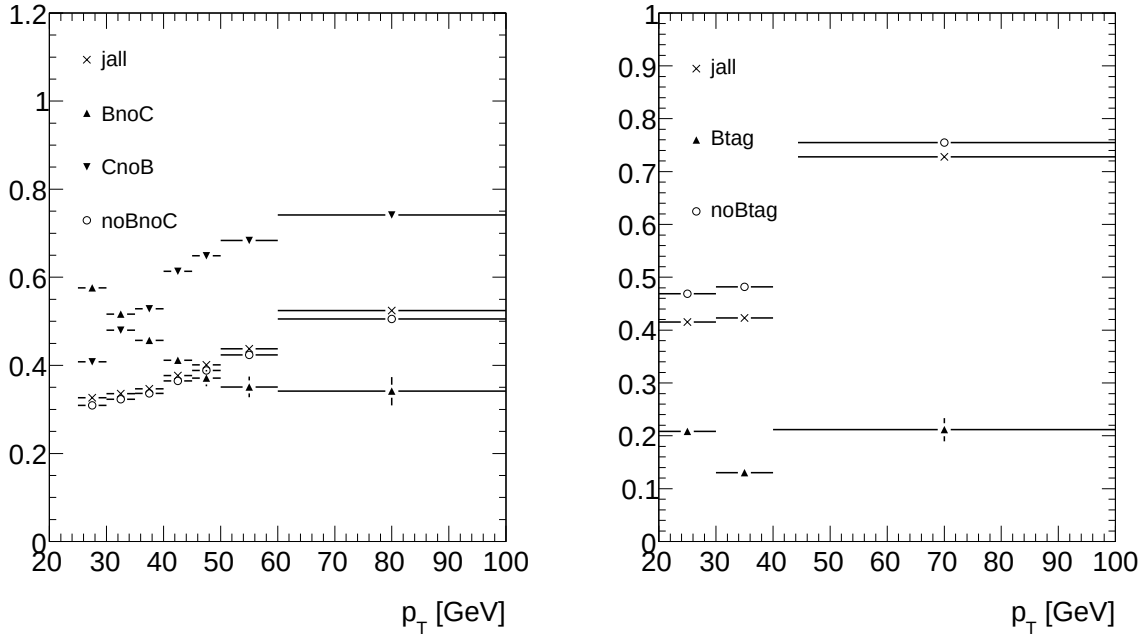

(a) (b)

Figure 5.17: Measured fake rates for (a) electrons and (b) muons. The fake rates are measured with several selection criteria to understand the fake rates for several sources of the fake leptons, such as b-flavor jets, photon conversions, and mis-identification of light-flavor jets. In the figure (a), "jall", "BnoC", "CnoB", and "noBnoC" correspond to measured fake rates in the entire control samples, the b-tag control samples, the PC control samples, and the other control samples, respectively.

For electron's fake rate estimation, the composition of sources of the fake leptons (flavor composition) in each control sample are estimated with assistance of the MC, which are summarized in Table 5.14. The samples have the different flavor composition, and therefore, the fake rates for each source can be estimated with the following matrix in Equation 5.8.

$$\begin{bmatrix} R_b \\ R_c \\ R_{\text{other}} \end{bmatrix} = \begin{bmatrix} HF_b & PC_b & LF_b \\ HF_c & PC_c & LF_c \\ HF_{\text{other}} & PC_{\text{other}} & LF_{\text{other}} \end{bmatrix} \begin{bmatrix} R_{HF} \\ R_{PC} \\ R_{LF} \end{bmatrix}, \tag{5.8}$$

where the R_{HF}, R_{PC}, R_{LF} represent the fake rate for heavy flavor jets (HF), the photon conversion (PC), and the light flavor (LF). The R_b, R_c, R_{other} are the measured fake rate in the three control samples. The element of the matrix is the flavor composition in the three control samples. The HF, PC, and LF represent the fraction of each sources originating from the heavy flavor quarks, the photon conversions, and the light flavor quarks.

pT	control region									signal region		
	b enhanced			PC enhanced			other					
	HF_b	PC_b	LF_b	HF_c	PC_c	LF_c	HF_{other}	PC_{other}	LF_{other}	HF	PC	LF
$25 < p_T < 30$	0.91	0.02	0.07	0	1	0	0.19	0.30	0.51	0.27	0.21	0.52
$30 < p_T < 40$	0.97	0.01	0.02	0	1	0	0.07	0.33	0.60	0.21	0.30	0.49
$40 < p_T$	0.50	0.00	0.50	0	1	0	0.02	0.37	0.61	0.11	0.29	0.60

Table 5.14: Flavor composition of the electron control samples and the signal sample. The notation is the same as that in 5.11.

The signal region fake rate is then given by a liner combination of the R_{HF}, the R_{PC}, and the R_{PC} as:

$$\epsilon_{fake}(p_T, \eta) = HF \times R_{HF}(p_T, \eta) + PC \times R_{PC}(p_T, \eta) + LF \times R_{LF}(p_T, \eta). \tag{5.9}$$

For muons, since the statistics of the loose lepton control samples is limited, simplified approach is taken to derive the fake late in the signal region. The fake rates measured in the b-tag control region R_{btag} and non-b-tag control region R_{nonbtag} are linearly-combined as:

$$\epsilon_{fake}(p_T, \eta) = 0.53 FR_{\text{btag}}(p_T, \eta) + 0.47 FR_{\text{nonbtag}}(p_T, \eta), \tag{5.10}$$

where the factors of the linear combination are chosen and validated in the W+jets control region to match the prediction and measurements.

Event weight determination

The measured efficiency and fake rates are translated into the event weight to estimate the fake contributions after applications of all tight lepton selections. The two loose dilepton samples collected with selections summarized in Table 5.13 are categorized into sub samples as followings: (1) both leptons pass the tight condition (N_{TT}), (2) one of them passes the tight conditions but the other fails (N_{TL}, N_{LT}) and (3) both of them fail (N_{LL}). Equation 5.11 describes the connection between (N_{TT}, N_{TL}, N_{LT}, N_{LL}) and (N_{RR}, N_{RF}, N_{FR}, N_{FF}) with the measured efficiency (r) and the fake rates (f). The (N_{RR}, N_{RF}, N_{FR}, N_{FF}) denotes numbers of followings types of events: (1) both leptons originating from truth electron N_{RR}, (2) one of them originates from true but the other from fake (N_{RF}, N_{FR}), and (3) both from fake (N_{FF}).

$$\begin{bmatrix} N_{TT} \\ N_{TL} \\ N_{LT} \\ N_{LL} \end{bmatrix} = \begin{bmatrix} rr & rf & fr & ff \\ r(1-r) & r(1-f) & f(1-r) & f(1-f) \\ (1-r)r & (1-r)f & (1-f)r & (1-f)f \\ (1-r)(1-r) & (1-r)(1-f) & (1-f)(1-r) & (1-f)(1-f) \end{bmatrix} \begin{bmatrix} N_{RR} \\ N_{RF} \\ N_{FR} \\ N_{FF} \end{bmatrix} \tag{5.11}$$

By solving this equation, the event weight is evaluated for each of loose dilepton samples so that the contamination of the fakes in the tight dilepton signal samples ($r(1-f)N_{RF} + (1-f)rN_{FR} + ffN_{FF}$) can be estimated. The weighting factors are evaluated for all individual events in the loosened dilepton sample according to two leptons' η and p_T in the events. The expectation of yield of fake lepton background are summarized in Table 5.15.

N_{jets}	fake lepton background event yields ± stat. ± syst. uncert. ee	$\mu\mu$	$e\mu$
0	$1.9 \pm 1.2 \pm 1.0$	$-0.07 \pm 0.03 \pm 0.04$	$3.8 \pm 2.3 \pm 1.9$
1	$1.1 \pm 0.9 \pm 0.5$	$-0.01 \pm 0.01 \pm 0.01$	$19.3 \pm 5.6 \pm 9.7$
≥ 2	$2.5 \pm 1.4 \pm 1.2$	$0.3 \pm 0.5 \pm 0.2$	$44.0 \pm 9.5 \pm 22.0$

Table 5.15: Overview of the estimated fake lepton background yields in the signal ($N_{\text{jets}} \geq 2$) and control regions using the matrix method for each channel. Statistical and systematic uncertainties are shown.

5.6.3 MC-based backgrounds

The contributions from other electroweak background processes ($Z/\gamma^* \to \tau\tau$, single top production, and the diboson production) are estimated with respect to the cross-section prediction given by the SM theory. The cross-sections of these processes are 66 pb, 1.0 pb, and 7.6 pb for $Z/\gamma^* \to \tau\tau$, single top production, and the diboson production, respectively[*12], which are much smaller than $Z/\gamma^* \to \ell\ell$ cross-section (1.0 nb) for ee and $\mu\mu$ final states. Owing to their small contributions, the uncertainties of their cross-section prediction are not expected to affect much in the $t\bar{t}$ cross-section measurements. Event yields for these background sources are summarized in Table 5.16 and the details of the uncertainties can be found in the Appendix D.3. The full set of systematic uncertainties is included for the MC-based background estimation (JES, JER, etc.) as well as the uncertainty due to the errors on the theoretical production cross-section. The largest uncertainty for these backgrounds originate from the uncertainty on their production cross-sections.

	Single t	Diboson	$Z/\gamma^* \to \tau\tau$
ee	$6.4\ ^{+1.2}_{-1.1}$	5.9 ± 1.0	4.9 ± 2.6
$\mu\mu$	$16.0\ ^{+1.9}_{-2.2}$	$8.7\ ^{+1.2}_{-1.5}$	11.0 ± 5.0
$e\mu$	41.1 ± 5.5	32.9 ± 4.9	42.5 ± 16.1

Table 5.16: Event yields for single top, diboson, and $Z/\gamma^* \to \tau\tau$ process backgrounds.

The predicted scales of $Z/\gamma^* \to \tau\tau$ and diboson (WW, WZ) is tested in the control samples, and they are found to be consistent with the collision data samples to have confidence in the MC prediction. They are discussed in the following sections.

$Z/\gamma^* \to \tau\tau$ background

In the $e\mu$ final state, the dominating physics processes are the $t\bar{t}$ signal and the $Z/\gamma^* \to \tau\tau$ background. Especially in the data samples with exactly zero jet and one jet, the $Z/\gamma^* \to \tau\tau$ background can be extracted with a good purity. By comparing the MC prediction with the measured distributions in the control samples, the MC is found to accurately describe the scales and the kinematics in the control region in Figure 5.18.

[*12]The branching fractions for dilepton final states are taken into account in the cross-section values here.

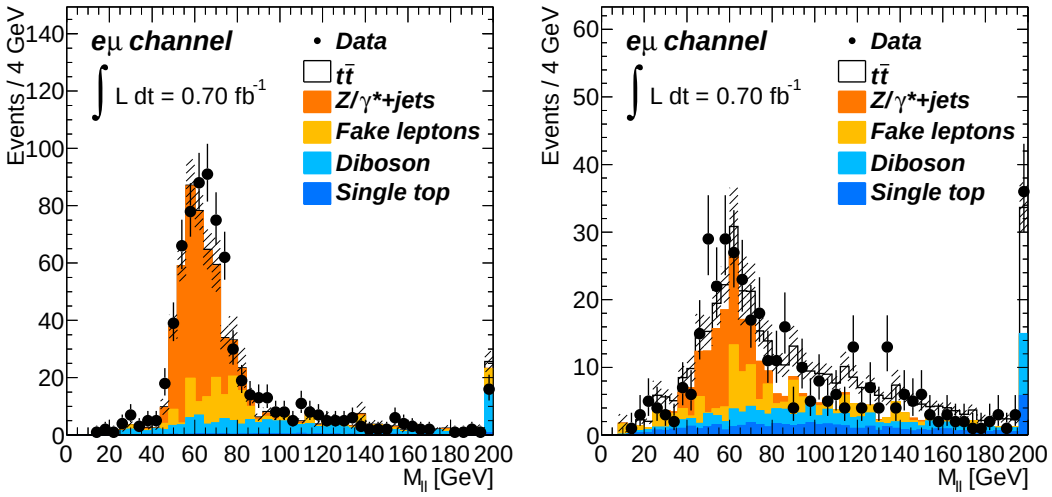

(a) (b)

Figure 5.18: Invariant mass of $e\mu$ in the 0-jet and 1-jet sideband region. It is shown that The MC accurately describe the kinematics in the control region.

Diboson background

The MC normalization of the diboson production (WW, WZ) is checked in $e\mu$ channel in control samples with low jet multiplicity ($= 0, 1$). By requirement of large E_T^{miss}($E_T^{miss} > 40$ GeV), the fraction of the diboson backgrounds can be enhanced while the $Z/\gamma^* \to \tau\tau$ events (main background other from the diboson events in these control sample) are suppressed. Figure 5.19 shows the distribution of the p_T of the dilepton system shows as an example distribution which may separate the diboson production events from the $Z/\gamma^* \to \tau\tau$ events. Especially in the 0 jet control samples, the diboson production is dominating the data samples. It is checked that the MC prediction and the data is consistent within the uncertainties in the control samples. The control samples with $N_{\text{jets}} = 0$ mainly consists of diboson physics process, and the control samples with $N_{\text{jets}} = 1$ consists of diboson, single top, and $t\bar{t}$ productions.

5.6.4 Evaluation of the total number of backgrounds

The evaluation of the total number of backgrounds and its uncertainties are summarized in Table 5.17, combining the evaluation of backgrounds from $Z/\gamma^* \to \ell\ell$, fake lepton identification, $Z/\gamma^* \to \tau\tau$, single top production, and diboson productions. The backgrounds are estimated to be 24.0 $^{+5.3}_{-4.7}$ events, 50.5 $\pm$ 8.6 events, and 157.1 $\pm$ 34.1 events in ee, $\mu\mu$, and $e\mu$ final states, respectively. The precision of $\approx 20\%$ has been achieved for all the three channels, and the uncertainty of theoretical cross-section evaluation and fake estimation are main sources of them.

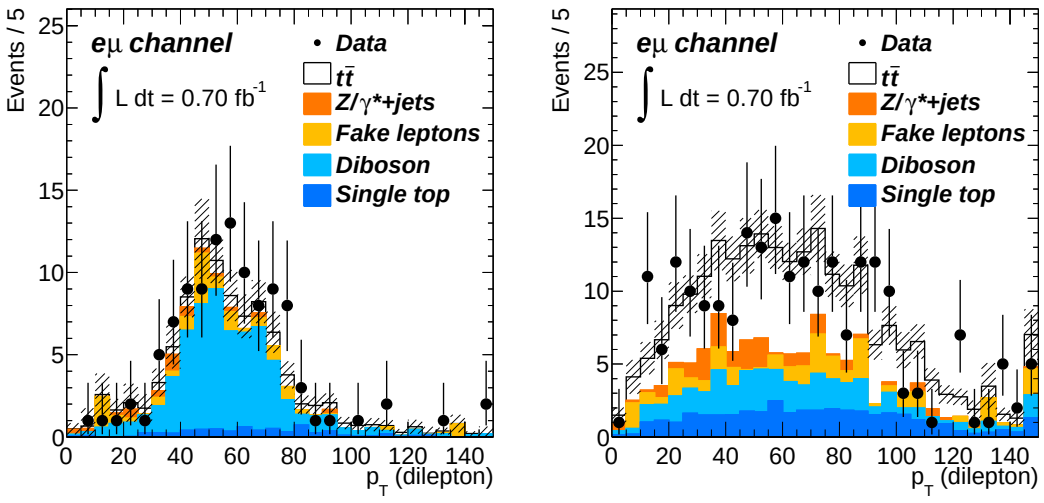

(a) (b)

Figure 5.19: p_T of the two lepton system in the control samples with $E_T^{miss} > 40$ GeV in (a) $N_{\text{jets}} = 0$ and (b) $N_{\text{jets}} = 1$ control samples. The scale is consistent between data and MC within the uncertainties. All the processes except for the fake leptons are estimated with the cross-section predicted by the SM.

5.7 Event yield and discussion on the signal kinematic distributions

5.7.1 Control regions

The detector calibration, the simulation modeling, and the scaling of $Z/\gamma^* \to ee$, $Z/\gamma^* \to \mu\mu$ is validated by comparing MC simulations with data in control regions which are orthogonal to the $t\bar{t}$ signal region but have similar kinematics. In particular, the Z mass region, defined as $|M_{\ell\ell} - M_Z| \leq 10$ GeV is used for ee, and $\mu\mu$ channels. The dilepton mass distributions are shown in Figure 5.20 and Figure 5.21 for ee, and $\mu\mu$ channels, respectively. The shape and scale of distributions are in good agreement in both inside of the Z window ($|M_{\ell\ell} - M_Z| < 10$ GeV) and outside of of the Z window ($|M_{\ell\ell} - M_Z| > 10$ GeV) in both ee and $\mu\mu$ channels. The calibration of for EM calorimeter and muon spectrometer performance are validated by the results. Also, the scaling of $Z/\gamma^* \to ee$, $Z/\gamma^* \to \mu\mu$, which is tuned using data inside Z window, is in good agreement even outside of the Z window.

Additional control regions are defined as events with low jet multiplicity, while the signal region requires equal to or more than two jets. These control samples are used in the validation of the $Z/\gamma^* \to \tau\tau$ and the diboson backgrounds in Section 5.6.3. Furthermore, the E_T^{miss} distributions in the low jet multiplicity control region are shown in Figure 5.22 and Figure 5.23. Good agreement between MC prediction and collision data is shown in E_T^{miss} distribution in

	ee	$\mu\mu$	$e\mu$
Backgrounds	23.6 events	50.5 events	160.5 events
	Δ Background (%)	Δ Background (%)	Δ Background (%)
Luminosity	+2.6/-2.6	+2.5/-2.5	+2.7/-2.7
Stat(Data)	+0.7/-0.7	+0.8/-0.8	-
Stat(MC)	±7.8	±5.6	±2.6
Z pT	±5.2	±3.4	±0.1
Fake	+7.9/-7.9	+1.1/-1.1	+14.9/-14.9
Method(DY)	±0.0	±0.4	-
x-sec(Theory)	+11.0/-11.3	+12.4/-13.3	+12.5/-12.5
JES	+7.1/-3.0	+1.6/+0.2	+6.6/-7.8
JER	±1.2	±7.0	±1.0
JEF	±0.1	±0.0	±0.1
MET(SoftJet)	+4.0/-0.8	-2.2/-0.2	±0.0
MET(PileUp)	+3.7/-0.7	-2.4/-0.9	±0.0
LAr(JetCleaning)	-0.1/-0.4	-0.1/-1.5	+0.3/-0.6
SF(Mu.ID)	±0.0	+0.8/-0.8	+0.4/-0.4
SF(Mu.Trig)	±0.0	+0.2/-1.3	±0.0
SF(El.ID)	+3.8/-3.7	±0.0	+1.9/-1.9
SF(El.Trig)	-0.3/+0.3	±0.0	+0.1/-0.1
Mu.ES	±0.0	±0.0	±0.0
Mu.ER(MS)	±0.0	+0.9/-1.8	±0.0
Mu.ER(ID)	±0.0	+1.8/-1.2	±0.0
El.ES	-1.5/+2.2	±0.0	+0.6/-0.1
El ER	+1.2/+0.9	±0.0	+0.2/+0.4
Syst(total)	+19.3/-17.5	+15.9/-17.0	+20.9/-21.3

Table 5.17: Total background and the uncertainties for ee, $\mu\mu$, and $e\mu$ channels.

the control regions with $N_{\text{jets}} = 1$ in all the three final states. The kinematic properties of the $N_{\text{jets}} = 1$ control samples are expected to be close to the signal region and this validates the MC modeling well. The E_T^{miss} distribution in events with no high p_T jet is slightly different in both ee and $\mu\mu$ channels, which is considered to originate from the mis-modeling of the calorimeter response that is not associated with the high p_T physics objects. The rate of the E_T^{miss} tail originating from the mis-modeling is measured to be negligibly small in the 0-jets sample, comparing with the E_T^{miss} tails originating from mis-measurements of high p_T physics objects in events with $N_{\text{jets}} \geq 1$. Then the effect of this mis-modeling is not expected to affect in the $t\bar{t}$ signal region with $N_{\text{jets}} \geq 2$.

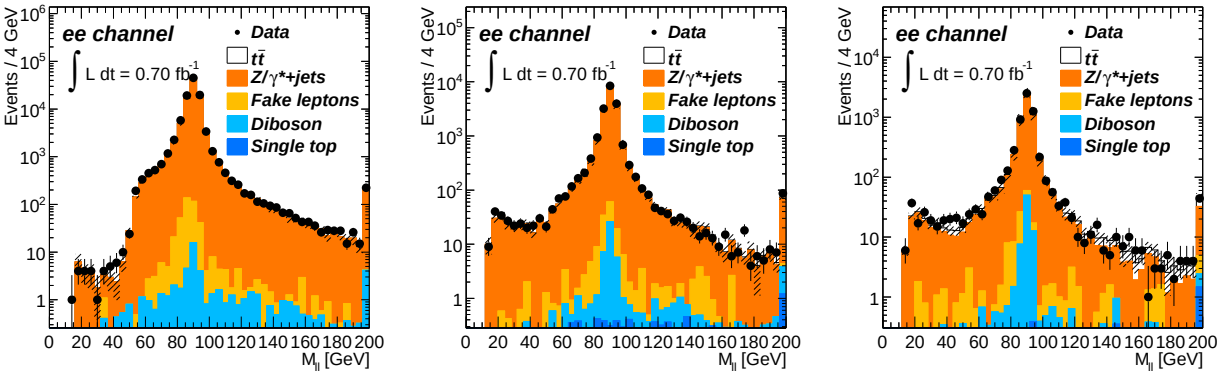

(a) (b) (c)

Figure 5.20: Invariant mass distribution of ee in the control region defined with $E_T^{miss} < 60$ GeV for the events with $N_{\text{jets}} = 0$, $N_{\text{jets}} = 1$, and $N_{\text{jets}} \geq 2$.

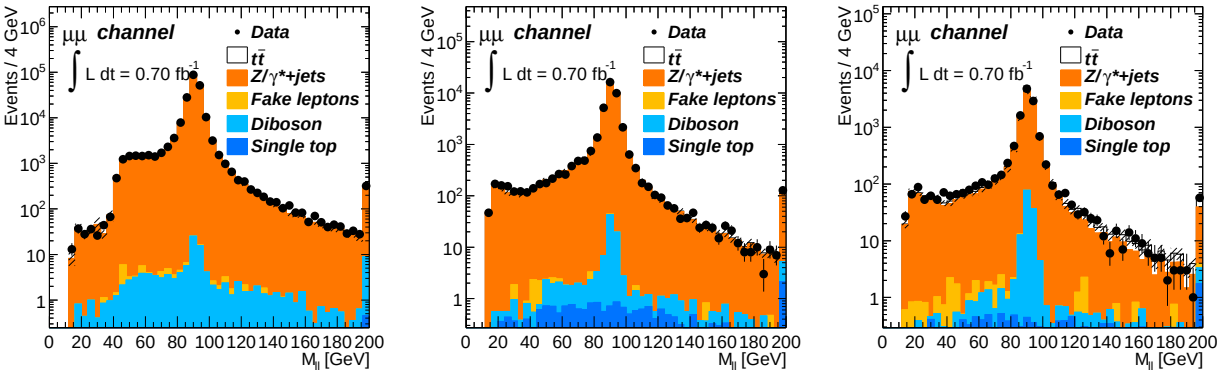

(a) (b) (c)

Figure 5.21: Invariant mass distribution of $\mu\mu$ in the control region defined with $E_T^{miss} < 60$ GeV for the events with $N_{\text{jets}} = 0$, $N_{\text{jets}} = 1$, and $N_{\text{jets}} \geq 2$.

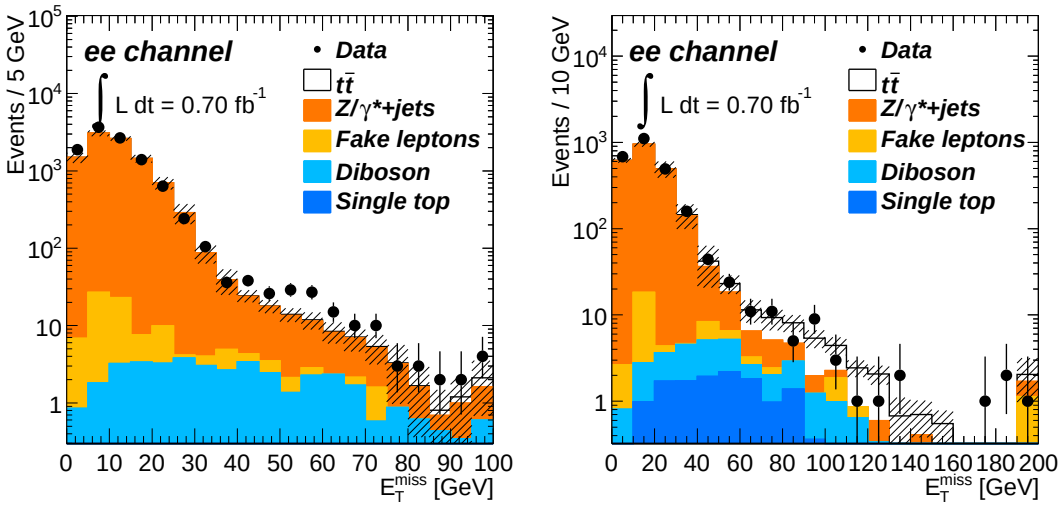

(a) (b)

Figure 5.22: The E_T^{miss} distribution in the 0 jets and 1 jets in ee channel outside of the Z mass region.

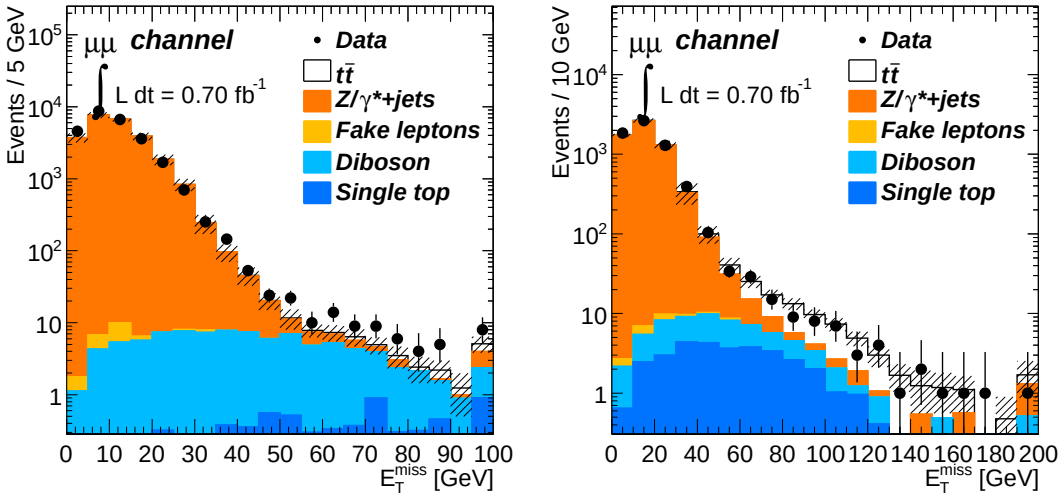

(a) (b)

Figure 5.23: The E_T^{miss} distribution in the 0 jets and 1 jets in $\mu\mu$ channel outside of the Z mass region.

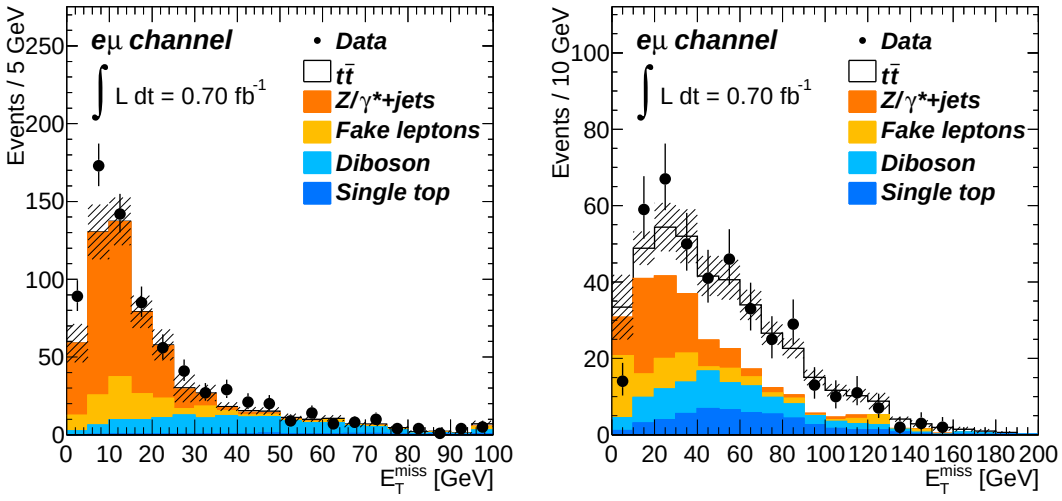

(a) (b)

Figure 5.24: The E_T^{miss} distribution in the 0 jets and 1 jets in $e\mu$ channel.

5.7.2 Signal region

In the data set of 0.70 fb^{-1} the total numbers of candidate events are 165 in the ee-channel, 301 in the $\mu\mu$-channel, and 963 in the $e\mu$-channel. The expectation for backgrounds and $t\bar{t}$ signals are summarized in Table 5.18, where the number of $t\bar{t}$ events are evaluated by the SM cross-section prediction ($\sigma_{t\bar{t}}^{\rm SM} = 164.6\ ^{+11.5}_{-15.8}$ pb). The results indicate the presence of $t\bar{t}$ production clearly as an excess against the background estimation. The distribution could not be explained without contributions of $t\bar{t}$ signal events, and therefore, the presence of t-quark has been confirmed at the pp collisions with $\sqrt{s} = 7$ TeV.

	ee	$\mu\mu$	$e\mu$
Drell-Yan+jets (DD)	$4.0\ ^{+2.5}_{-1.2}$	$14.4\ ^{+5.4}_{-4.2}$	-
Drell-Yan($\rightarrow \tau\tau$)+jets (MC)	4.9 $\pm$ 2.6	11.0 $\pm$ 5.0	42.5 $\pm$ 16.1
Fake leptons (DD)	2.5 $\pm$ 1.9	0.3 $\pm$ 0.6	44.0 $\pm$ 24.0
Single top (MC)	$6.4\ ^{+1.2}_{-1.1}$	$16.0\ ^{+1.9}_{-2.2}$	41.1 $\pm$ 5.5
Diboson (MC)	5.9 $\pm$ 1.0	$8.7\ ^{+1.2}_{-1.5}$	32.9 $\pm$ 4.9
Total (non $t\bar{t}$)	23.6 $\pm$ 4.4	50.5 $\pm$ 8.4	160.5 $\pm$ 34.1
$t\bar{t}$ (MC)	124.0 $\pm$ 17.2	$241.3\ ^{+14.5}_{-17.9}$	745.5 $\pm$ 41.8
Total expected events	147.6 $\pm$ 17.8	$291.8\ ^{+16.6}_{-19.9}$	906.6 $\pm$ 53.9
Observed events	165	301	963

Table 5.18: The full breakdown of the expected $t\bar{t}$-signal and background in the signal region compared to the observed event yields, for each of the dilepton channels (MC is simulation based, DD is data-driven) after all systematic uncertainties are included and the correlations between the different background sources are taken into account.

In Figure 5.25(a), Figure 5.26(a), and Figure 5.27(a), the E_T^{miss} distributions (ee, $\mu\mu$) and H_T distribution ($e\mu$) shown, after application of all the selections except for $E_T^{miss} > 60$ GeV (in ee and $\mu\mu$) or $H_T > 130$ GeV (in $e\mu$) requirements. In Figure 5.25(b), Figure 5.26(b), and Figure 5.27(b), the number of selected jets are shown for ee, $\mu\mu$ and $e\mu$ channels. All the selection is applied except for $N_{\rm jets} \geq 2$ cut. These variables in the signal region are in good agreement with the MC simulation of $t\bar{t}$ scaled with the cross-section predicted by the SM. Figure 5.28(a) and 5.28(b) show combined distribution of the three channels.

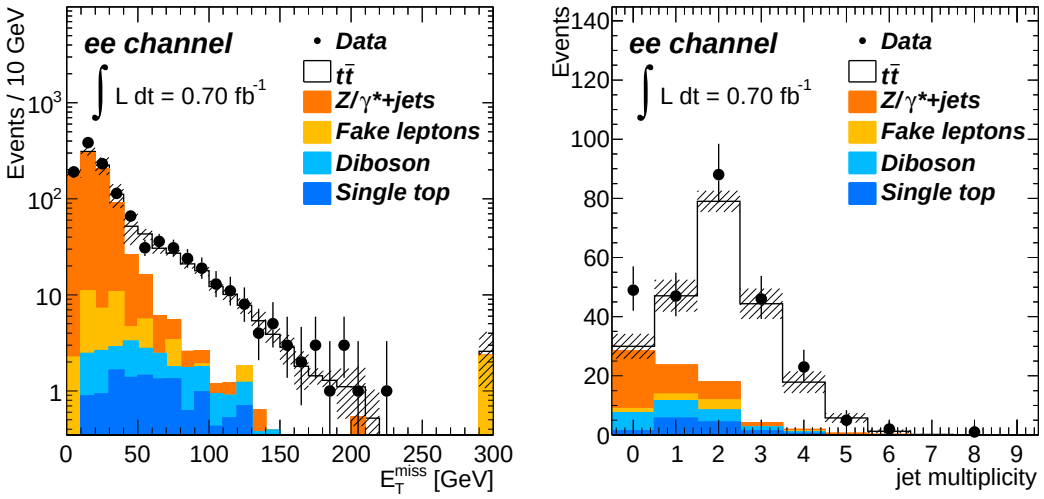

(a) (b)

Figure 5.25: Distributions in the signal region for the ee final state. (a) The E_T^{miss} distribution in the signal region without $E_T^{miss} > 60$ GeV requirement. (b) The number of jets distribution in the signal region without $N_{\text{jets}} \geq 2$ requirement.

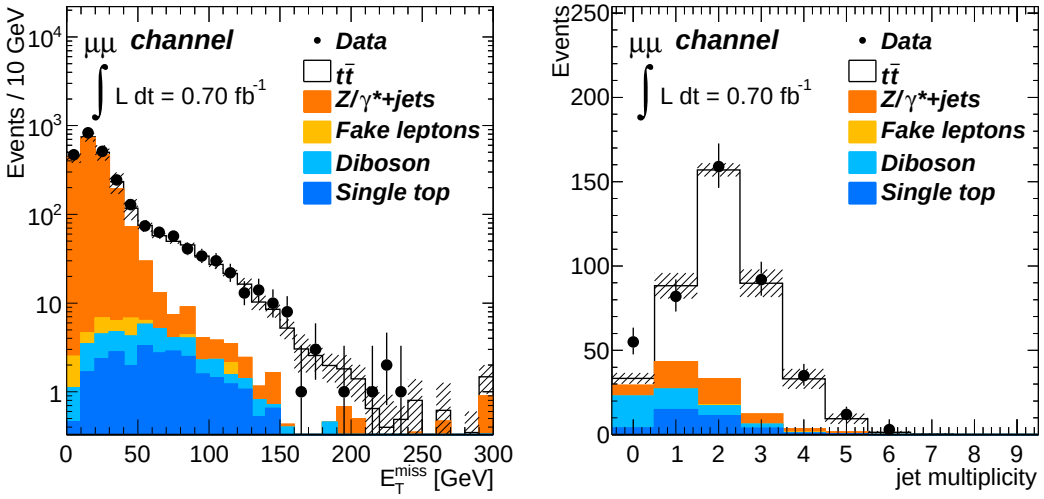

(a) (b)

Figure 5.26: Distributions in the signal region for the $\mu\mu$ final state. (a) The E_T^{miss} distribution in the signal region without $E_T^{miss} > 60$ GeV requirement. (b) The number of jets distribution in the signal region without $N_{\text{jets}} \geq 2$ requirement.

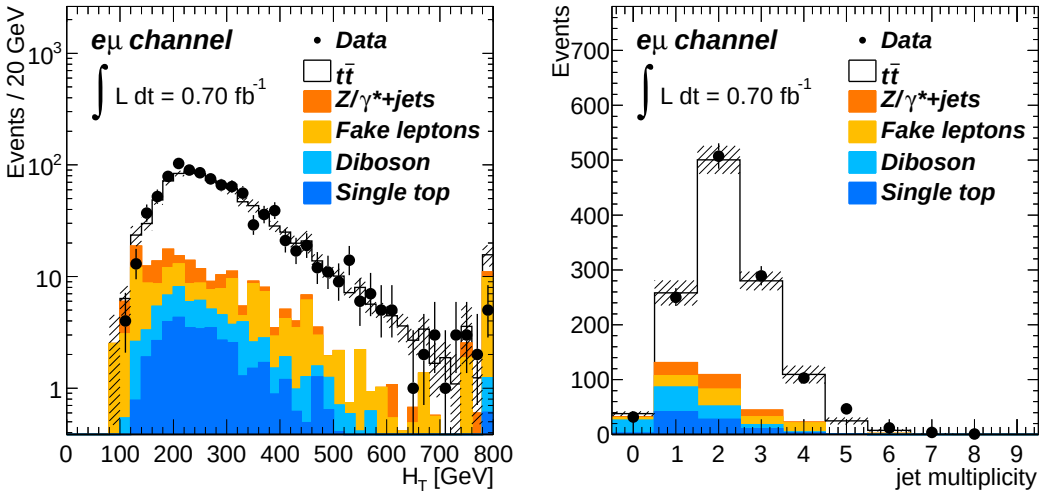

(a) (b)

Figure 5.27: Distributions in the signal region for the $e\mu$ final state. (a) The H_T distribution in the signal region without $H_T > 130$ GeV requirement. (b) The number of jets distribution in the signal region without $N_{\text{jets}} \geq 2$ requirement.

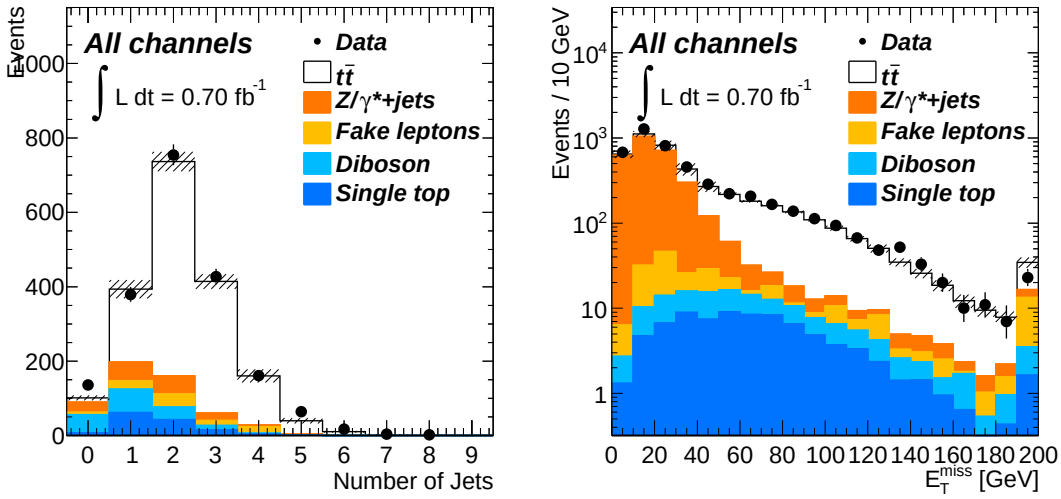

(a) (b)

Figure 5.28: (a) Jet multiplicity in the signal region without the $N_{\text{jets}} \geq 2$ requirement for all the combined three channels. (b) E_T^{miss} distribution in signal region without $E_T^{miss} > 60$ GeV or $H_T > 30$ GeV requirements for all the combined three channels.

5.7.3 Comparison of kinematic distributions in $t\bar{t}$ events between data and QCD prediction

Comparisons of the kinematic variables in $t\bar{t}$ events between data and MC are performed using the selected $t\bar{t}$ candidate events. The purity of $t\bar{t}$ in the samples is expected to be $\approx 83\%$. In Figure 5.29 presents distributions of η of selected electrons, η of selected muons, η of selected jets, and E_T^{miss} distribution after all selections applied to extract the $t\bar{t}$. All three channels are combined in η distributions, while the E_T^{miss} distributions are extracted only in the $e\mu$ final states for which no explicit E_T^{miss} criteria are applied. For these variables, Any clear disagreement between the measurements and the MC prediction can be a good hint for new phenomena (see examples introduced in Section 2.4). As results of the comparison, it is found that the shapes of these kinematic variables are in good agreement with the distribution simulated by the perturbative QCD within the uncertainty, and no big discrepancy is found in $t\bar{t}$ in the distribution.

5.7.4 Comparison of kinematic distributions in $t\bar{t}$ events for the variation of PDF sets

As discussed in Section 2.2.3, the pure $t\bar{t}$ samples enables the validation of the sets of the PDF in the particular parameter space of (Q, x) that permits the $t\bar{t}$ production (see Figure 2.7). Figure 5.30 shows comparisons between $t\bar{t}$ distribution extracted from collision data and the simulated distribution of $t\bar{t}$ events with several sets of parton distribution functions. As variation of the PDF sets, CTEQ6.6 [10], NNPDF2.0 [43], and MSTW2008 [44] are compared and shown in the figures, all of which are calculated with next-leading higher order approximation (NLO PDF). The jet multiplicity distributions and the H_T distributions are shown in the figures, which are expected to be sensitive to the difference of the $\sqrt{\hat{s}}$ according to the choice of the PDF sets. The distributions are in good agreement in the $t\bar{t}$ production events with the collision data as well within their uncertainties. It is confirmed that all the tuned PDF sets model the pp collisions well in interactions with (Q^2, x_1, x_2) corresponding to the $\sqrt{\hat{s}} > 2m_t$ in the pp collisions with $\sqrt{s} = 7$ TeV.

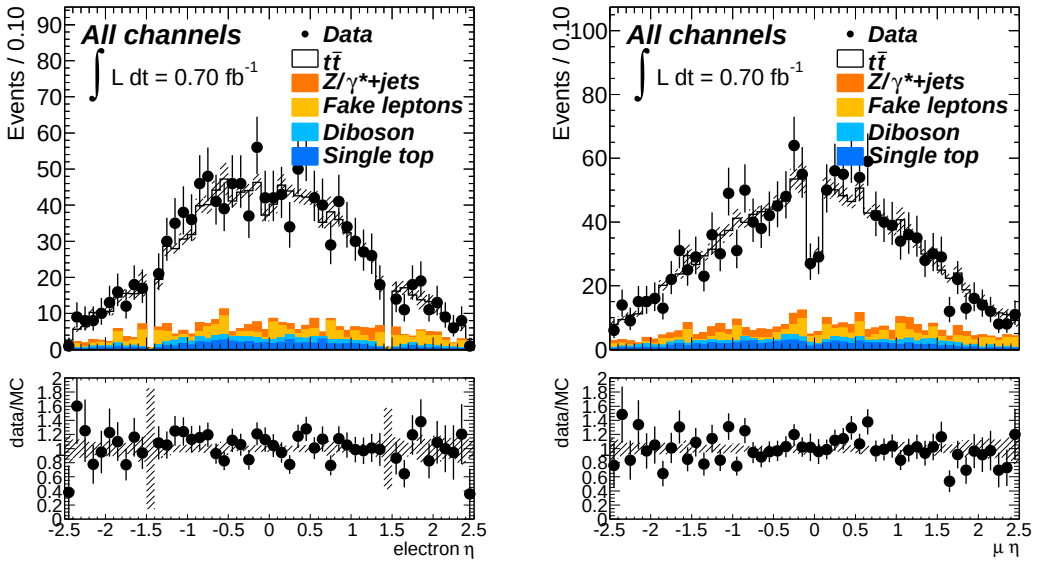

(a)

(b)

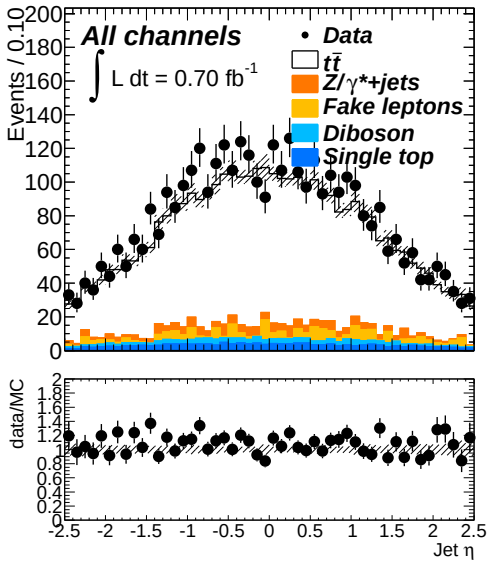

(c)

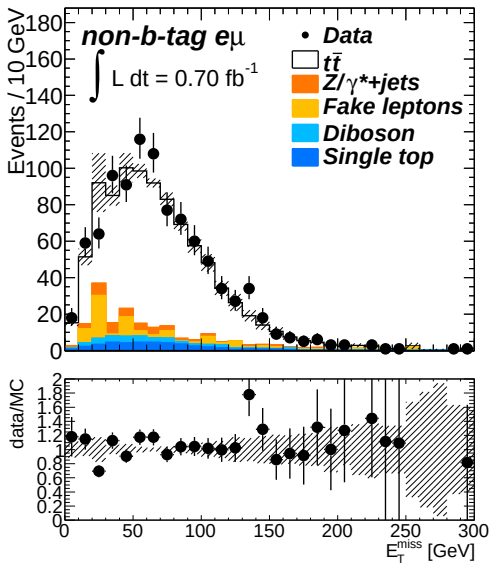

(d)

Figure 5.29: Distributions of the kinematic variables in the $t\bar{t}$ enhanced samples, which include 1,429 events with expected purity of 83%, are shown for the $e\mu$ final states. (a) The reconstructed η of selected electrons, and (b) muons, (c) selected jets, and (d) the E_T^{miss} are shown. The E_T^{miss} distribution is extracted in $e\mu$ final states to which no E_T^{miss} cuts are applied explicitly. All of them are in good agreement with the prediction by the SM, and we have no significant disagreement between data and simulation in the selected $t\bar{t}$ samples.

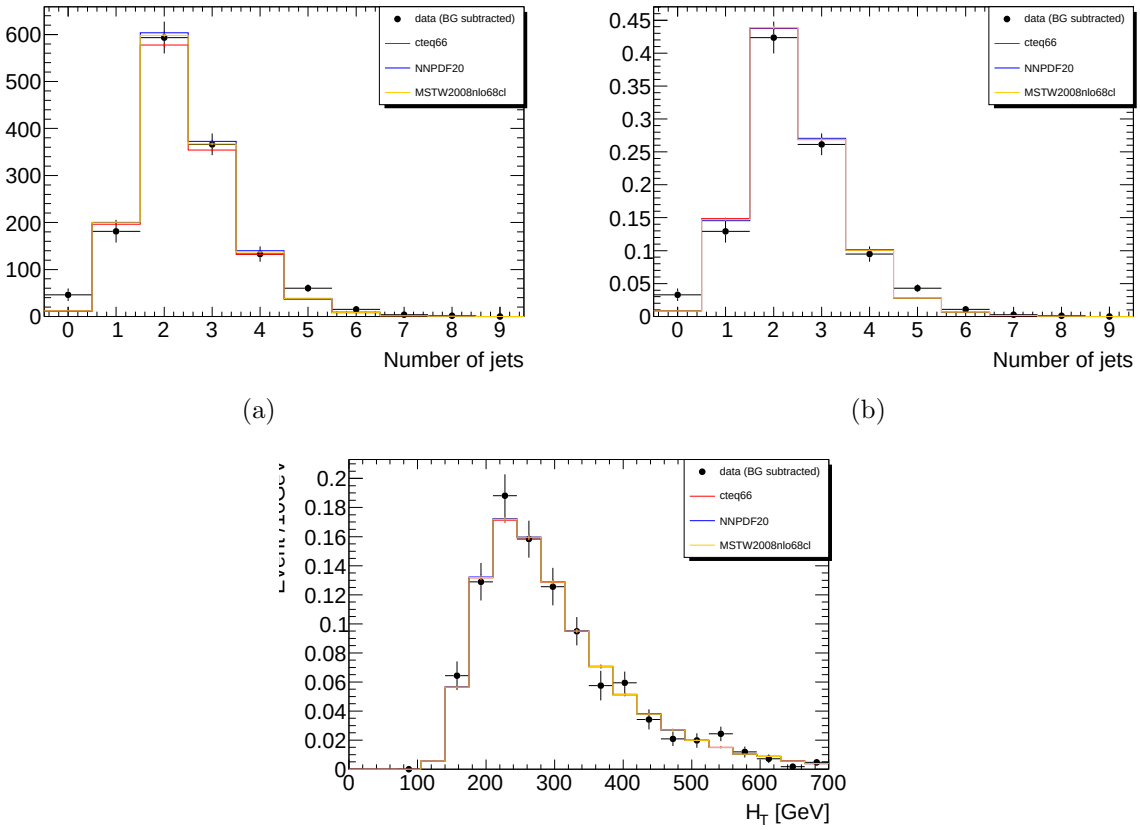

Figure 5.30: Comparison between $t\bar{t}$ samples extracted from the collision data and the simulation samples: (a) jet multiplicity distribution after all selections except for jet multiplicity cuts are applied, (b) jet multiplicity distribution with normalization to get the total integrated entry = 1, and (c) H_T distribution with the application of all selections. The H_T distribution should be sensitive to the difference of the $\hat{s}$ according to the choice of the PDF sets. As the variation of the PDF sets, distributions with CTEQ6.6, NNPDF2.0, and MSTW2008 are shown in the figures. The expected cross-section is slightly different between the three NLO PDF sets, as shown in (a), while the shape of the distributions are very close, as shown in (b) and (c).

5.7.5 Comparison of kinematic distributions in $t\bar{t}$ events for the variation of ISR/FSR parameters

As discussed in Chapter 2, several parameters are introduced in the QCD calculation, such as Λ_{QCD} scale or the p_T cut-off in the final state radiation. The comparison of the distribution focusing on the QCD parameter variation is discussed in this section. For the discussion, the ISR/FSR samples mentioned in Section 5.4 are used. These QCD parameters are varied in the MC samples in range compatible to their errors in the past experimental results [41]. The jet multiplicity, jet p_T, and jet η distributions are considered for the ISR and FSR variation that may modify the properties of the jets in $t\bar{t}$ events, and it is good to compare the distributions with the ISR/FSR variation samples in order to validate the parameter tuning.

Figure 5.31 shows comparisons between the $t\bar{t}$ distribution extracted from collision data and the simulated $t\bar{t}$ distribution with the ISR and FSR variation. The higher ISR results in more jets with high p_T, while the higher FSR results in less jets with high p_T since the parton momentum may be dispersed. It is checked that these distributions are consistent with the nominal distribution within these variations of the QCD parameters. It indicates that these QCD parameters are well chosen.

5.8 Results of cross-section measurements

5.8.1 Results of individual channels

Combining the results discussed in the previous sections (i.e. $\mathcal{L}$, $\mathcal{A}$, N_{observed}, and $N_{\text{background}}$), the $t\bar{t}$ production cross-section is finally extracted with Equation 5.1. The results of all the channels are shown in Table 5.19.

Channel	$\sigma_{t\bar{t}}$ (pb) (stat., syst., lumi.)
ee	$187.6 \pm 17.1(\text{stat.}) \,^{+33.3}_{-25.4}(\text{syst.}) \,^{+8.4}_{-7.2}(\text{lumi.})$ pb
$\mu\mu$	$170.7 \pm 11.8(\text{stat.}) \,^{+16.8}_{-10.6}(\text{syst.}) \,^{+7.8}_{-6.7}(\text{lumi.})$ pb
$e\mu$	$177.1 \pm 6.9(\text{stat.}) \,^{+15.2}_{-11.9}(\text{syst.}) \pm 7.5(\text{lumi.})$ pb

Table 5.19: Measured cross-sections in individual channels.

In the table, three errors are shown that originate from limited data statistics, systematic uncertainties, and uncertainties of the luminosity determination, respectively. For the systematic uncertainty, they are summed up quadratically and Table 5.21 shows contributions of individual systematic sources.

5.8.2 Cross-section extraction by a statistical combination of measurements

The results for the three channels are combined using a profile likelihood technique.

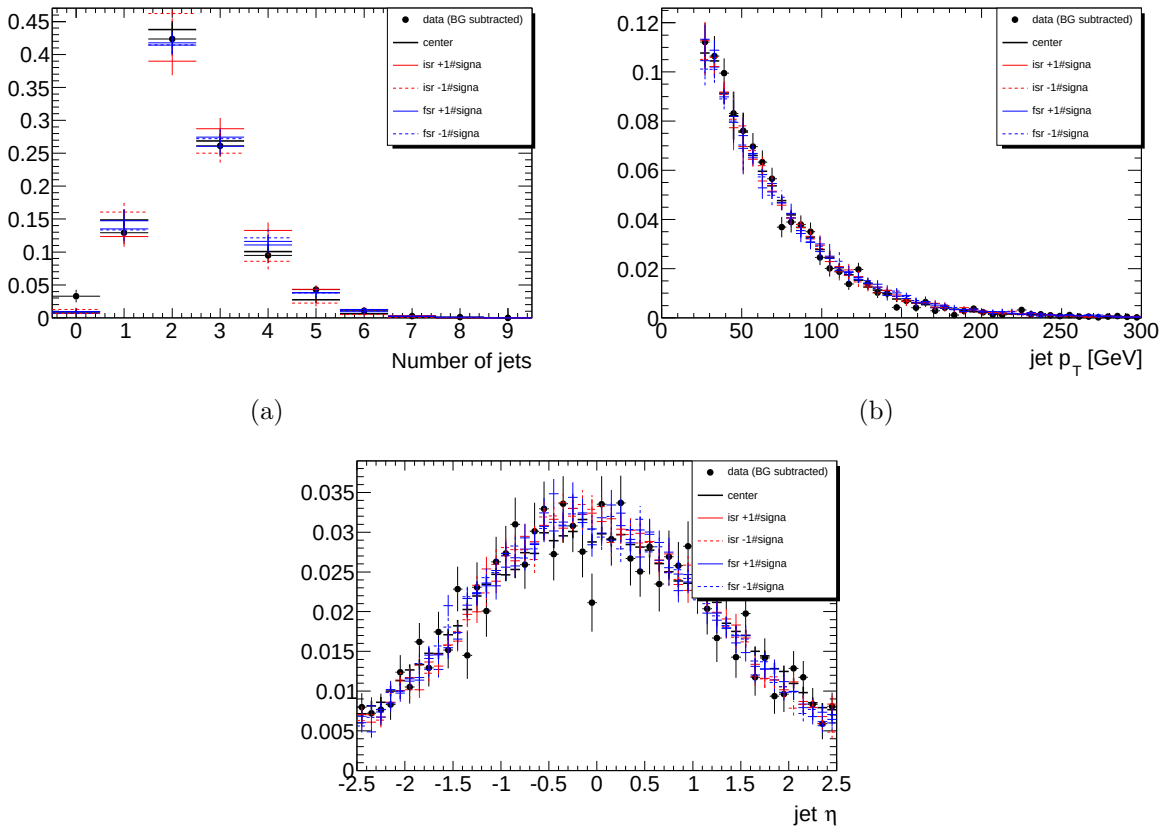

(a) (b)

(c)

Figure 5.31: (a) Jet multiplicity distribution after all selections except for jet multiplicity cuts are applied, and (b) p_T and (c) η distributions of the selected jets in the signal region samples. The distributions with the ISR/FSR parameters varied by $\pm 1\sigma$ of their uncertainty are superimposed in the figures with red and blue lines. The dashed line and solid line correspond to $+1\sigma$ and -1σ respectively. The nominal choice of the parameters are in good agreement with the data, and all the ISR/FSR variation samples are consistent within a few times of their uncertainties.

In the likelihood evaluation, the observed event count for each channel N^{obs} is modeled as being Poisson distributed with its mean value of $N_{\text{tot}}^{\text{exp}}$, which is the sum of several contributions from signal and background processes. The variation in the expected number of events from each process due to systematic uncertainties is parametrized and additional terms are included into a likelihood function that summarizes the uncertainty in the corresponding nuisance parameters. The signal expectation is scaled according to the luminosity, and the signal cross-section $\sigma_{t\bar{t}}$, the parameter of interest, is a free parameter in the fit. The various sources of systematic uncertainties are organized such that they are considered either totally uncorrelated or totally correlated. For each source of systematic (indexed by j) a nuisance parameter α_j is introduced, such that $\alpha_j = 0$ represents the nominal estimate and $\alpha_j = \pm 1$ represents a $\pm 1\sigma$ variation of that source. Next, the sources of the systematic uncertainties are varied (e.g. jet energy scale, trigger efficiencies, etc.) and a piecewise-linear interpolation is used to parametrize the expected

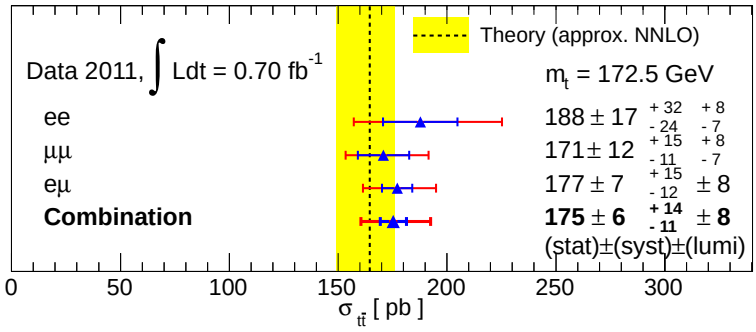

Figure 5.32: The measured $t\bar{t}$ production cross-section for the three individual channels and for the combination of the three channels. The yellow band shows the cross-section predicted by the NNLO p-QCD.

number of events $N_i^{\text{exp}}(\vec{\alpha})$ for each of the signal and background. A change in the source of the j^{th} systematic introduces a totally correlated variation among the contributions (indexed by k). Additional terms are added to the likelihood function to summarize the knowledge of the α_j derived from auxiliary measurements or assumptions about the uncertainty in the Monte Carlo modeling. This leads to the final form of the likelihood function:

$$\mathcal{L}(\sigma_{\text{sig}}, L, \alpha_j) = \prod_{i \in \text{ channel}} \text{Pois}\left(N_i^{\text{obs}} \,|\, N_{i,\text{tot}}^{\text{exp}}(\sigma_{\text{sig}}, \vec{\alpha})\right) \times G(L_0|L, \sigma_L) \times \prod_{j \in \text{syst}} G(0|\alpha_j, 1)\,. \quad (5.12)$$

The cross-section is inferred from the profile likelihood ratio:

$$\lambda(\sigma_{\text{sig}}) = \mathcal{L}(\sigma_{\text{sig}}, \hat{\hat{L}}, \hat{\hat{\alpha}}_j)/\mathcal{L}(\hat{\sigma}_{\text{sig}}, \hat{L}, \hat{\alpha}_j),$$

where a single circumflex represents the maximum likelihood estimate (MLE) of the parameter and the double circumflex represents the conditional MLE with σ_{sig} fixed.

The likelihood minimization are performed by a scan around the minimizing sets of parameters, and then, the cross-section finally is extracted as a results of three-channel combination to be:

$$175 \pm 6 \text{ (stat.)} \, ^{+14}_{-11} \text{ (syst.)} \pm 8 \text{ (lumi.) pb.}$$

These results are summarized in the Figure 5.32 with reference to the theoretical prediction.

Table 5.21 provides the uncertainties for each systematic contribution. The combined results has an improvement in the uncertainties. The statistical uncertainty is below the level of the systematic uncertainties. The total relative uncertainty is evaluated to be $-8.0\%/+10.0\%$.

	ee	$\mu\mu$	$e\mu$	combined
Uncertainties (%)	$\Delta\sigma/\sigma$[%]			
	Data Statistics			
Data Statistics	-8.9 / 9.3	-6.8 / 7.1	-3.8 / 3.9	-3.2 / 3.2
	LHC			
Luminosity	-3.8 / 4.5	-3.9 / 4.6	-4.0 / 4.4	-4.1 / 4.5
	Monte Carlo Simulation and Signal Modeling			
MC Statistics	-1.9 / 2.0	-1.4 / 1.5	-0.8 / 0.8	-0.6 / 0.7
Monte Carlo Generator	-2.3 / 2.7	-0.0 / 0.0	-0.8 / 1.0	-0.8 / 0.9
Parton Shower Simulator	-4.2 / 5.0	-0.7 / 0.8	-2.8 / 3.1	-2.4 / 2.6
ISR	-3.0 / 3.6	-0.5 / 0.6	-0.9 / 1.2	-0.7 / 0.9
FSR	-7.1 / 9.0	-2.2 / 2.6	-1.3 / 1.4	-1.2 / 1.3
PDF	-2.3 / 2.7	-1.9 / 2.3	-2.3 / 2.5	-2.3 / 2.5
Z p_T modeling	-0.0 / 1.2	-0.6 / 0.7	-0.0 / 0.0	-0.0 / 0.2
MC cross-section	-0.9 / 1.6	-1.7 / 1.7	-1.9 / 1.9	-1.8 / 1.8
	Detector Modeling			
Lepton Energy Scale	-0.0 / 0.8	-0.0 / 0.0	-0.0 / 0.3	-0.0 / 0.4
Lepton Energy Resolution	-0.0 / 0.7	-0.5 / 0.5	-0.0 / 0.0	-0.5 / 0.0
Lepton Efficiency	-5.4 / 6.2	-1.1 / 2.9	-2.9 / 3.2	-2.5 / 2.7
Jet Energy Scale	-8.8 / 9.6	-4.4 / 7.6	-0.0 / 5.0	-3.3 / 5.6
Jet Energy Resolution	-1.0 / 1.2	-1.8 / 1.8	-0.0 / 0.5	-0.0 / 0.0
Jet Efficiency	-0.0 / 0.0	-0.0 / 0.0	-0.0 / 0.0	-0.0 / 0.0
E_T^{miss} (CellOut Term)	-0.0 / 0.8	-0.8 / 0.4	-0.0 / 0.0	-0.5 / 0.0
E_T^{miss} (Pileup Effect)	-0.0 / 0.7	-0.5 / 0.6	-0.0 / 0.0	-0.0 / 0.2
LAr Cleaning	-0.6 / 0.9	-0.6 / 1.4	-0.7 / 1.1	-0.7 / 1.3
	Data-driven Background Evaluation			
Fake Evaluation	-0.9 / 1.7	-0.0 / 0.4	-3.0 / 3.0	-1.9 / 1.9
Z/γ^* Evaluation	-0.0 / 0.4	-0.0 / 0.0	-0.0 / 0.0	-0.0 / 0.0
Systematics Total	-14.0 / 18.4	-7.3 / 10.9	-7.8 / 9.7	-7.3 / 9.5
Syst. + Stat.	-16.6 / 20.6	-10.0 / 13.0	-8.7 / 10.4	-8.0 / 10.0

Table 5.20: Summary of the $t\bar{t}$ cross-section uncertainties for each channel and combination of the all channels.

	ee	$\mu\mu$	$e\mu$	combined
Uncertainties (%)	$\Delta\sigma/\sigma$[%]			
Data Statistics	-8.9 / 9.3	-6.8 / 7.1	-3.8 / 3.9	-3.2 / 3.2
Luminosity	-3.8 / 4.5	-3.9 / 4.6	-4.0 / 4.4	-4.1 / 4.5
Simulation	-9.5 / 12.2	-3.9 / 4.3	-4.5 / 5.0	-4.0 / 4.3
Detector modeling	-10.3 / 11.8	-4.9 / 8.7	-4.2 / 6.1	-4.0 / 6.4
Data-driven BG	-0.9 / 1.7	-0.0 / 0.4	-3.0 / 3.0	-1.9 / 1.9
Syst. + Stat.	-16.6 / 20.6	-10.0 / 13.0	-8.7 / 10.4	-8.0 / 10.0

Table 5.21: Summary of the $t\bar{t}$ cross-section uncertainties for each channel after grouping errors.

5.8.3 Mass dependence

The t-quark mass dependence of the $\sigma_{t\bar{t}}$ measurement is discussed in this section. The cross-section measurements are repeated using the simulation samples with the several t-quark mass assumption between 160 GeV and 190 GeV. The kinematic distribution depends on the t-quark mass. Thus the signal acceptance also depends on the t-quark mass, which can modify the results of the measurement. The nominal results, shown in Section 5.8.2, is extracted with an assumption of $m_t = 172.5$ GeV. The central value is modified to 176 pb and 171 pb when the t-quark mass is varied to 170 GeV and 175 GeV, respectively. This means the fluctuation of the cross-section measurement for the t-quark mass uncertainty (173.2 ± 0.9 GeV) is found to be much less than other uncertainties.

Figure 5.33 shows the comparison between the measured cross-section and theoretical prediction given by the NNLO perturbative QCD calculation as a function of the assumed t-quark mass from 160 GeV to 190 GeV. The t-quark mass which is preferred by the comparison between measured and predicted cross-section is consistent with the world average of the mass measurements, shown with blue lines in the figure.

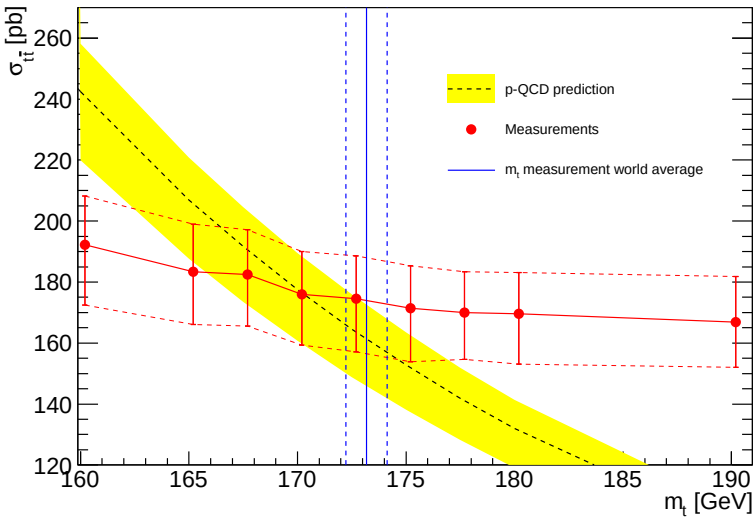

Figure 5.33: The experimentally measured cross-section as a function of the t-quark mass assumption (solid red line), where the 1σ uncertainty is given with the red dashed line. The yellow band shows the cross-section prediction by the NNLO p-QCD calculation.

5.9 Comparison of results with other measurements

The extracted cross-section in the analysis has been compared with following measurements:

- Measurements using b-tagging technique in dilepton final states at pp collisions with $\sqrt{s} = 7$ TeV (see Section 5.9.1)

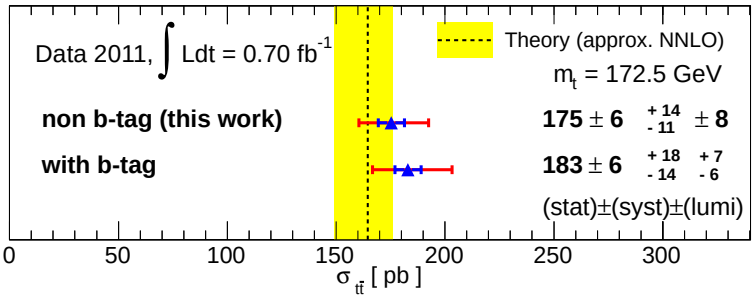

Figure 5.34: Comparison between analyses with and without b-tagging information.

- Measurements in lepton+jets final states at pp collisions with $\sqrt{s} = 7$ TeV (see Section 5.9.2)
- Measurements at $p\bar{p}$ collisions with $\sqrt{s} = 1.96$ TeV (see Section 5.9.3).

5.9.1 Comparison with analysis using b-tagging information

Analysis using b-quark jet tagging (b-tagging)[*13] information is performed in the dilepton final state as well [47]. Assuming 100% branching fraction of $t \to bW$ decay, requiring at least one b-tagged jet reduces backgrounds which do not contain the b-quarks in their final states effectively. The b-tagging requirement enables an effective identification of the $t\bar{t}$ events, and loosen the E_T^{miss} cuts in ee and $\mu\mu$ final states. $E_T^{miss} > 40$ GeV is required after the b-tagging requirement while $E_T^{miss} > 60$ GeV is applied in the main analysis, which does not use the b-tagging. Therefore, the sample collected by the analysis with b-tagging information is not a simple sub-sample of that of the main analysis, and the comparison between the two analyses works as a good cross-check to confirm the accuracy of the measurements. The results of the analyses with the b-tagging technique are summarized in Figure 5.34, comparing them with the results of the main analysis. They are in good agreement with each other and as well as with the SM prediction. The result also suggest that the branching fraction of $t \to bW$ decay is consistent to 100% within the uncertainties of the measurements, which agrees with the current knowledge of the CKM matrix: $|V_{ts}|, |V_{td}| \ll |V_{tb}| \approx 1$ (see Section 2.3).

5.9.2 Comparison with analysis in lepton+jets final states

Analysis using the lepton+jets (ℓ+jets) final states (see Section 2.3.5) is performed as well [48]. The signature of the $t\bar{t}$ events in the ℓ+jets final states is (1) exactly one lepton, (2) more than

[*13] The b-quark jet can be characterized with the long life time of B hadrons. In the analysis, the b-tagging algorithms form likelihood ratio from the life time measurement by the explicit reconstruction of secondary vertexes, the impact parameter measurement of each track, and the other three secondary vertex properties that can give us some separation of b-jet and light jet. In the selection, the threshold corresponding to 80% efficiency for b-jets are used in b-tagging.

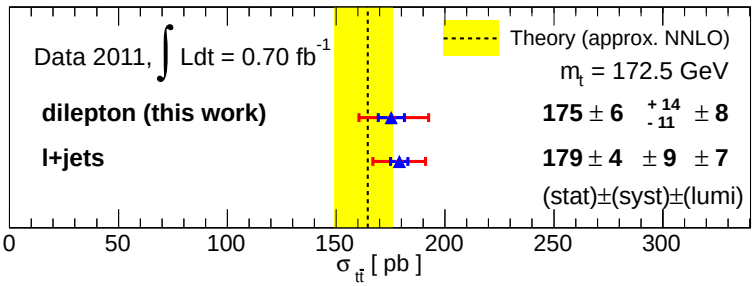

Figure 5.35: Comparison between analyses in dilepton and lepton+jets final states.

three jets, (3) large E_T^{miss}, and (4) large $M_T(W)$ and the ℓ+jets candidate events and dilepton candidate events are disjoint. The extracted cross-section are

$$179 \ \pm \ 4(\text{stat.}) \ \pm \ 9(\text{syst.}) \ \pm \ 7(\text{lumi.}), \tag{5.13}$$

and it is in good agreement with the dilepton result. The results are summarized in Figure 5.35. Furthermore, since the ℓ+jets and dilepton make use of disjoint samples, ℓ+jets enables not only to make good cross-checking but also to extract the greatest results by a combination between these two results. As discussed in Section 5.8, the Maximum Likelihood Estimator is used in the combination, considering correlation of the common uncertainty sources between two analyses, such as detector-related uncertainties. By the combination, the $t\bar{t}$ production cross-section is measured to be:

$$179 \pm 3 \text{ (stat.)} \pm 7 \text{ (syst.)} \pm 7 \text{ (lumi.) pb}. \tag{5.14}$$

The total uncertainties of systematic and statistical errors is 6.0%, and this is the most precise measurement of the $t\bar{t}$ cross-section at the $\sqrt{s} = 7$ TeV pp collisions. The precision is better than the theoretical prediction $164.6\ ^{+11.5}_{-15.8}$ pb, and the result suggests the inclusive $t\bar{t}$ cross-section is well described in the current modeling of the theory.

5.9.3 Comparison with the Tevatron results

The results can be compared with measurements in the $p\bar{p}$ collisions with $\sqrt{s} = 1.96$ TeV at the Tevatron [49]. Figure 5.36 shows a comparison between measurements and the theoretical prediction of the $t\bar{t}$ production cross-section as a function of $\sqrt{s}$ of pp or $p\bar{p}$ collisions. The blue band corresponds to prediction of $\sigma_{t\bar{t}}$ in pp collisions and the yellow band corresponds to that in $p\bar{p}$ collisions, where the parton distribution functions with factorization scale of m_t, strong coupling constant with measured $\alpha_s(m_Z)$, and renormalization scale of m_t are used. The measurements are shown by closed circle (main results at pp collisions with $\sqrt{s} = 7$ TeV (ATLAS)), triangles (at pp collisions with $\sqrt{s} = 7$ TeV (ATLAS) in ℓ+jets final states or in dilepton with b-tagging information), and boxes (at $p\bar{p}$ collisions with $\sqrt{s} = 1.96$ TeV). The results confirms that the current theoretical model of the p-QCD (the SM) can be applied for the broad range of $\sqrt{s}$ from 1.96 TeV up to 7 TeV without any significant modification.

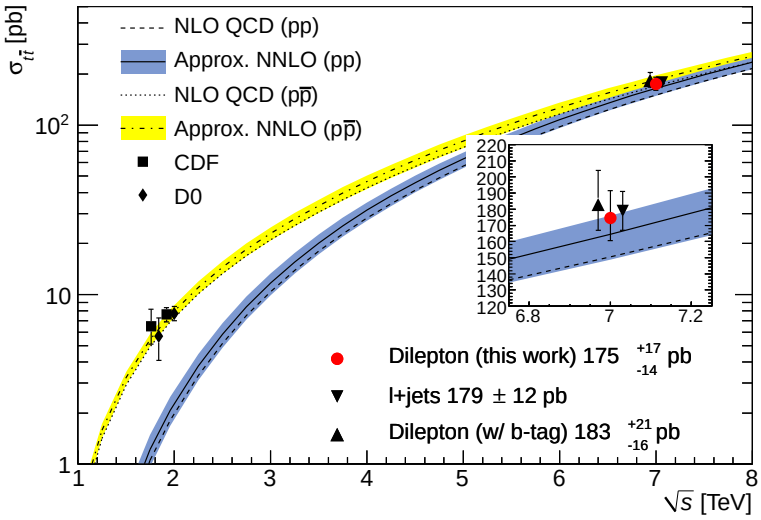

Figure 5.36: The cross-section prediction by p-QCD is shown with blue band for $p\bar{p}$ collisions and pp collisions as function of $\sqrt{s}$. Measurements are consistent to the p-QCD prediction both at the LHC (7 TeV) and the Tevatron (1.96 TeV). The measurements confirm that the p-QCD can predict the $t\bar{t}$ cross-section in both energy scales with the single set of parameters.

Chapter 6

Conclusion

The measurement of the $t\bar{t}$ production cross-section at the LHC experiments is presented. This is the first precise measurement at the pp collisions with $\sqrt{s} = 7$ TeV with the large amount of the collision data ($\mathcal{L} = 0.70$ fb^{-1}).

I have conducted the following studies in the frontier of the LHC-ATLAS data analysis for the achievement of the $t\bar{t}$ cross-section measurement:

- The detection efficiencies and the momentum resolutions are evaluated using the control samples of collision data, in particular for electrons and muons using Z control samples.
- The effect of the multiple pp interactions (the pileup interactions) in the high luminosity environment of the LHC are evaluated, which confirms the correctness of the simulation of effects of the additional interactions.
- The event selection criteria are optimized with reference to the measured detector performance and the pileup effect.
- The methods to evaluate the backgrounds is well-established and performed using collision data sample.

These achievements enabled me to collect the $t\bar{t}$ samples effectively and the expected purity is $\approx 83\%$ in the samples. With them, the cross-section has been measured to be

$$175 \pm 6 \text{ (stat.)} \, ^{+14}_{-11} \text{ (syst.)} \pm 8 \text{ (lumi.) pb},$$

where stat., syst., and lumi. denote the statistical error, the sum of systematic errors, and the uncertainty originating from the luminosity determination, respectively. The result is in good agreement with the theoretical prediction ($164.6 \, ^{+11.5}_{-15.8}$ pb) by the perturbative QCD calculation in the SM. The level of the uncertainty is less than 10% and is compatible to that of the theoretical prediction. The $t\bar{t}$ samples extracted from the collision data were studied in details and compared with the theoretical prediction, and it has been shown that the SM describes the $t\bar{t}$ production well at the 7 TeV pp collisions.

As discussed in this thesis, the analysis includes following achievements:

- Confirmation of the presence of t-quark at the LHC

- Establishment of the method to identify $t\bar{t}$ events at the LHC pp collisions and to evaluate the background contamination
- The first precise measurement of the $t\bar{t}$ production rates in the dilepton final state at the 7 TeV collisions
- First detailed study of the $t\bar{t}$ production kinematic properties in the LHC which confirms the current particle physics SM describes them well.

Furthermore, these achievements are applicable for other physics programs. For new physics search in the $t\bar{t}$ production with such signatures as $t\bar{t} + E_T^{miss}$ or $t\bar{t}$+jets, it is essential to collect the $t\bar{t}$ samples effectively and control the backgrounds well. For analyses in which the $t\bar{t}$ is a dominating background such as the supersymmetry search program, it is important progress that the detailed test of the $t\bar{t}$ kinematic properties has become available with the collision data, and it would improve their sensitivity. These studies focusing on the particular parameter space of $t\bar{t}$ will be conducted on the basis of the achievements presented in this thesis with more collision data samples recorded by the ATLAS detector.

Besides performing the analysis of $t\bar{t}$ cross-section measurements, I have been leading the operation of the muon trigger electronics system. The calibration of the timing parameters in the coincidence logic is successfully done with a $\approx 1\ ns$ precision and as superior and uniform performance as the design has been obtained in the commissioning period of the LHC, which results in the good performance of the $t\bar{t}$ cross-section measurements. This also resulted in the many precise measurements which use muons as event signatures.

More than 10 times statistics of the collision data is expected by the end of the LHC operation with $\sqrt{s} = 7$ TeV in 2012 and gives opportunities to perform precise measurements of effects originating from new phenomenon beyond the SM or the effect of the Higgs boson couplings. Searches for physics beyond the SM in $t\bar{t}$ event topology are built upon excellent understanding of the SM $t\bar{t}$ production, and therefore, the precision measurement of the $t\bar{t}$ cross-section is an important milestone to reach the new developments of the elementary particle physics.

Appendix A

Additions for Chapter 2

A.1 Renormalization and the evolution of the coupling constant

The Q dependence of the α_s is predicted when the theory is re-normalized.

In the QCD calculation, the coupling constant α_s depends on the momentum transfer in the interaction (Q^2). This running coupling constant as a function of Q^2, is described like:

$$\alpha_s(Q^2) = \frac{1}{b_0 \ln \frac{Q^2}{\Lambda^2_{QCD}}} \tag{A.1}$$

where

$$b_0 = \frac{11N_C - 2n_f}{12\pi} \tag{A.2}$$

with n_f beings the number of quark flavors, whose mass is lower than Q, and $N_C = 3$ standing for the number of quark colors. This running coupling constant is quite well measured as function of the Q in several measurements as summarized in Figure 2.3.

To avoid divergence at the hard scattering limit, which is called ultraviolet divergence, is carried out with dimensional regularization where the dimension in integral is changed from 4 into $4 - 2\epsilon$, where the ϵ represents tiny variation of the number of dimensions. Then the renormalization scale, which is denoted as μ_R, is introduced to keep consistent dimensions for quantities. The dependence of cross-section prediction on the μ_R is absorbed in the α_s in the renormalization process to keep the Lagrangian forms in the tree level calculation, and the evolution of α_s is expressed in terms of a renormalization group equation:

$$\frac{d\alpha_s(\mu_R^2)}{d\ln(\mu_R^2)} = \beta(\mu_R^2) \tag{A.3}$$

The perturbative expansion of the β function is calculated to 4-loop approximation is described with following equation,

$$\beta(\alpha_s(Q^2)) = -\beta_0\alpha_s^2(Q^2) - \beta_1\alpha_s^3(Q^2) - \beta_2\alpha_s^4(Q^2) - \beta_3\alpha_s^5(Q^2) + \ldots, \tag{A.4}$$

where

$$\beta_0 = \frac{33 - 2n_f}{12\pi},$$
$$\beta_1 = \frac{153 - 19n_f}{24\pi^2},$$
$$\beta_2 = \frac{77139 - 15099n_f + 325n_f^2}{3456\pi^3},$$
$$\beta_3 \approx \frac{29243 - 6946.3n_f + 405.089n_f^2 + 1.49931n_f^3}{256\pi^4}. \tag{A.5}$$

In Equation A.5, $N_C = 3$ is assigned to the number of quark colors. A solution of the equation in 1-loop approximation, i.e. neglecting β_1 and higher order terms, is

$$\alpha_s(\mu_R^2) = \frac{\alpha_s(M^2)}{1 + \alpha_s(M^2)\beta_0 \ln \frac{\mu_R^2}{M^2}} \tag{A.6}$$

The M is a reference mass scale, which has to be introduced since the QCD does not predict actual value of the α_s. By introducing the $\Lambda(\mu^2) \equiv \frac{\mu^2}{e^{1/\beta_0 \alpha_s(\mu^2)}}$ as dimensional parameter so that the α_s can be written like

$$\alpha_s(\mu_R^2) = \frac{1}{\beta_0 \ln \frac{\mu_R^2}{\Lambda^2}} \tag{A.7}$$

The Λ parameter is representing the energy scale of Q where the $\alpha_s(Q^2)$ diverse to infinity. To give a numerical example, $\Lambda \approx 0.1$ GeV for $\alpha_s(M_{Z^0} = 91.2 \text{ GeV}) = 0.12$ and $n_f = 5$.

The choice of μ_R is arbitrary and generally the momentum transfer Q is set as μ_R in the calculation. In the $t\bar{t}$ cross-section prediction, the $\mu_R = m_t = 172.5$ GeV is chosen by default and the uncertainties are checked with the interval of $[\frac{m_t}{2.}, 2.m_t]$.

A.2 Parton distribution functions

Sum rules that the PDFs follow are summarized in this section. Quantum fluctuations from the vacuum which can either involve gluons or quark and anti-quark pairs, the contribution from the sea quarks has to be symmetric in quarks and anti-quarks. Therefore, if we consider that the proton consists of three valence quarks uud, the expectation values for the signed number of u-quarks and d-quarks inside a proton have to satisfy followings two equations.

$$< N_u >= \int_0^1 dx(f_u(x) - f_{\bar{u}}(x)) = 2 \tag{A.8}$$

$$< N_d >= \int_0^1 dx(f_d(x) - f_{\bar{d}}(x)) = 1 \tag{A.9}$$

The total momentum of the proton has to consist of sum of all parton momentum, and then following equation should be fulfilled.

$$< \sum x_i >= \int_0^1 dx\ x\ \left(\sum_q f_q(x) + \sum_{\bar{q}} f_{\bar{q}}(x) + f_g(x) \right) = 1 \tag{A.10}$$

A.3 Total cross-section evaluation for variation of the m_t assumption

The SM expectation of the cross-section of $t\bar{t}$ are evaluated with several top-mass m_t assumptions. The dependence is summarized in the Figure A.1.

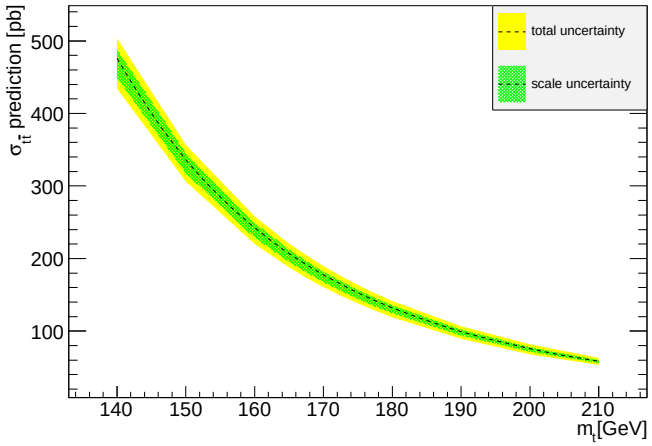

Figure A.1: $\sigma_{t\bar{t}}$ predicted by the SM for various t-quark mass (m_t) assumption. The green band shows the renormalization and factorization scale uncertainties, and the yellow band shows the total uncertainties, including the parton distribution function uncertainties.

A.4 Introduction of the Higgs boson and the spontaneous symmetry breaking

In the Standard Model, interactions between particles are described with the gauge theory of $SU(3)_C \otimes SU(2)_L \oplus U(1)_Y$ group. It corresponds the color triplet (strong interaction), the weak iso-spin doublet, and the hyper charge singlet (electroweak interaction). They are based on the gauge invariance assumption, by which the mass terms of the vector boson and quarks are forbidden. A $SU(2)_L$-doublet scalar field ($\phi(x) \equiv \begin{pmatrix} \phi^+(x) \\ \phi^0(x) \end{pmatrix}$), called the Higgs field, is introduced to break the gauge symmetry spontaneously, and the Lagrangian of the field is given with following equation.

$$\mathcal{L} = (D_\mu \phi)^\dagger D^\mu \phi - V(\phi). \tag{A.11}$$

where,

$$V(\phi) = \mu^2 \phi^\dagger \phi + \lambda (\phi^\dagger \phi)^2. \tag{A.12}$$

The Lagrangian $\mathcal{L}$ is gauge invariance with

$$D_\mu \phi = \left(\partial_\mu + ig\mathbf{W}_\mu \cdot \tau + igY_\phi B^\mu\right) \phi, \tag{A.13}$$

where the $\mathbf{W} \equiv (W_{1\mu}, W_{2\mu}, W_{3\mu})$ and B are gauge fields which are introduced to keep gauge covariance in local $SU(2)_L \otimes U(1)_Y$ transformation, $\tau \equiv \frac{\sigma}{2}$ is the $SU(2)$ generator, and Y_ϕ is the hyper charge of the Higgs field, which is $Y_\phi = Q_\phi - T_3 = \frac{1}{2}$. If the $\mu^2 < 0$, and $\lambda > 0$ are satisfied in equation A.12, the ϕ has vacuum expectation value of

$$|\langle 0|\phi^0|0\rangle| = \sqrt{\frac{-\mu^2}{2\lambda}} \equiv \frac{v}{\sqrt{2}}. \tag{A.14}$$

We could parametrize the field $\phi(x)$ with four real fields of $\theta \equiv (\theta_1, \theta_2, \theta_3)$ and $H(x)$, as shown in Equation A.15. Further, the local $SU(2)_L$ invariance of the Lagrangian allows us to rotate away any dependence of θ, and the gauge is fixed like:

$$\phi(x) = \exp\left(i\frac{\sigma}{2}\cdot\theta\right)\frac{1}{\sqrt{2}}\begin{pmatrix} 0 \\ v + H(x) \end{pmatrix} \rightarrow \frac{1}{\sqrt{2}}\begin{pmatrix} 0 \\ v + H(x) \end{pmatrix}. \tag{A.15}$$

The covariant derivative couples the scalar ϕ with the $\mathbf{W}$ and B. Following Equation A.15, the $D_\mu\phi$ is transformed like:

$$D_\mu\phi = \frac{1}{\sqrt{2}}\begin{pmatrix} 0 \\ \partial_\mu H(x) \end{pmatrix} + ig\frac{1}{2\sqrt{2}}\begin{pmatrix} W_{3\mu} & \sqrt{2}W^+_\mu \\ \sqrt{2}W^-_\mu & -W_{3\mu} \end{pmatrix}\begin{pmatrix} 0 \\ v + H(x) \end{pmatrix} + ig'\frac{1}{2\sqrt{2}}\begin{pmatrix} 0 \\ B_\mu(v + H(x)) \end{pmatrix}, \tag{A.16}$$

where $W^\pm_\mu$ are defined as:

$$W^+_\mu \equiv \frac{W_{1\mu} + iW_{2\mu}}{\sqrt{2}} \tag{A.17}$$

$$W^-_\mu \equiv \frac{W_{1\mu} - iW_{2\mu}}{\sqrt{2}}, \tag{A.18}$$

corresponding to $W^\pm$ bosons, respectively.

$$\begin{aligned}(D_\mu\phi)^\dagger(D_\mu\phi) \quad &= \frac{1}{2}\partial_\mu H(x)\partial^\mu H(x) + \frac{1}{4}g^2 W^-_\mu W^{+\mu}(v + H(x))^2 \\ &+\frac{1}{8}(-gW_{3\mu} + g'B_\mu)(-gW^\mu_3 + g'B^\mu)(v + H(x))^2 \\ &\equiv \frac{1}{2}\partial_\mu H(x)\partial^\mu H(x) + \frac{1}{4}g^2 W^-_\mu W^{+\mu}(v + H(x))^2 \\ &+\frac{1}{8}g^2\frac{1}{\cos^2\theta_W}Z_\mu Z^\mu(v + H(x))^2.\end{aligned} \tag{A.19}$$

Then θ_W is Weinberg angle, which is defined as $cos\theta_W \equiv \frac{g}{\sqrt{g^2+g'^2}}$, and Z_μ is defined as $Z_\mu \equiv \cos\theta_W W_{3\mu} - \sin\theta_W B_\mu$, which corresponds to the Z boson in the Standard Model. Term proportional to $W^-_\mu W^{+\mu}$, and $Z_\mu Z^\mu$ can be in Equation A.20, and these terms are the mass terms of the factor of the terms correspond to mass of the vector bosons. The W and Z boson obtain the mass by spontaneous symmetry breaking introduced by the vacuum expectation value of $\phi(x)$ (v) to be:

$$(m_W)^2 = \quad \frac{g^2v^2}{4} \tag{A.20}$$

$$(m_Z)^2 = \quad \frac{g^2v^2}{4\cos^2\theta_W}, \tag{A.21}$$

where v is expected to be 246 GeV with reference to the m_W and the g.

Under the gauge invariance, fermion mass terms $\mathcal{L} = -m\bar{\psi}\psi = -m(\bar{\psi}_L\psi_R + \bar{\psi}_R\psi_L)$ is not allowed, since the term is not symmetry in the gauge transformation, which is differently defined for right-handed and left-handed fermions. We can also introduce following gauge invariant terms of scalar field in the Lagrangian,

$$\mathcal{L}_Y = -c_1(\bar{u}, \bar{d})_L \begin{pmatrix} \phi^{(+)} \\ \phi^{(0)} \end{pmatrix} d_R - c_2(\bar{u}, \bar{d})_L \begin{pmatrix} \phi^{(0)*} \\ -\phi^{(-)} \end{pmatrix} u_R - c_3(\bar{\nu_e}, \bar{e})_L \begin{pmatrix} \phi^{(+)} \\ \phi^{(0)} \end{pmatrix} e_R + \text{h.c}, \quad \text{(A.22)}$$

where the second term involves charge conjugate of the scalar field $\phi^C \equiv i\sigma_2\phi^*$. In the fixed gauge (unitary gauge), the Lagrangian takes

$$\mathcal{L}_{\text{Yukawa}} = -\frac{1}{\sqrt{2}}(v + H)(c_1\bar{d}d + c_2\bar{u}u + c_3\bar{e}e). \quad \text{(A.23)}$$

Therefore, the Higgs field can introduce the mass term of fermions, and the mass of the fermions is $m_d = c_1\frac{v}{\sqrt{2}}$, $m_u = c_2\frac{v}{\sqrt{2}}$, and $m_e = c_3\frac{v}{\sqrt{2}}$. Then it could be concluded that the coupling constants between the Higgs scalar field and fermion fields are according to the mass of fermions. This representation is expanded to three generations of the quark and leptons. Accordingly, 9 additional constants are introduced to describe the coupling between the Higgs boson and fermions, assuming the mass of neutrino is 0. Corresponding to c_1, c_2, and c_3, Yukawa coupling constant is introduced like y_i and it is proportional to its mass, where i denote the flavor of the fermion.

Appendix B

Additions for Chapter 3

B.1 Luminosity evaluation from the beam parameters

The design of instantaneous luminosity of the LHC is 10^{34} cm^{-2} s^{-1}, and this is achieved with high frequency (40 MHz (every 25 ns) proton-proton crossing), focused beam ($\sigma_{x,y}$ =16 μm), and high intensity of the protons(10^{11}). The luminosity is evaluated with following equation

$$\mathcal{L} = \frac{f \times N_B^2}{4\pi \times \sigma_x \times \sigma_y} \approx \frac{40 \times 10^6 \times (10^{11})^2}{4\pi \times 16\mu\text{m} \times 16\mu\text{m}} \approx 10^{34}\ \text{cm}^{-2}\ \text{s}^{-1}, \tag{B.1}$$

where f, N_B, σ_x, and σ_y are frequency of beam-beam crossing, number of protons per a bunch, and beam width for transverse directions.

B.2 Luminosity evaluation from the monitored interaction rates

The luminosity of a pp collision can be expressed as shown in Equation 5.2. The ATLAS monitors the delivered luminosity by measuring the μ with variety of detectors and using several different algorithms. Taking the efficiency to measure the inelastic scattering in the particular scheme, the luminosity ($\mathcal{L}$) will be evaluated during the pp collision runs [18]. To minimize the uncertainties of the luminosity evaluation, the σ_{inel} is estimated with good precision in the beam position scan [*1] [24]. The scan is done with several configuration of the separation between two proton beams typically from -0.2 mm to +0.2 mm in x and y direction, respectively, where the luminosity is given as:

$$\mathcal{L}_{\text{measured}} = \frac{f_{\text{r}}}{2\pi\Sigma_x\Sigma_y \times n_b n_1 n_2}. \tag{B.2}$$

In the equation, the Σ_x and Σ_y denote the horizontal and vertical profiles of the colliding beams, which is given as configuration beam separation in the scan, and n_1 and n_2 denote the number

[*1] The main motivation of this scan is to find the best condition of pp collisions. This scan is called the Van der Meer scan.

of protons in a bunch, which can be estimated by the measured beam current. Then the total inelastic scattering is expressed like

$$\sigma_{\mathrm{inel}} = \frac{\mu f_{\mathrm{r}}}{\epsilon \mathcal{L}_{\mathrm{measured}}}, \tag{B.3}$$

where the ϵ is the detection efficiency in the particular measurements of μ. Then the extraction of σ_{inel} is performed by a fit of μ with appropriate function as a function of beam separation.

Appendix C

Additions for Chapter 4

C.1 The gate width functionality

The BCID circuits employ an additional delay functionality in the clock line, as shown in Figure 4.2(a), which enables a single TGC hits to be labeled with two neighboring BCID. The timing chart of the BCID circuits is shown in Figure C.1, where an asynchronous hit signal from TGC (red line) is shaped into a synchronous signal and labeled with BCID of "B" and "C" ("OUT", blue line). As shown in the Figure, a TGC signal with its rising edge located after the nominal clock signal's rising (blue) and before the delayed clock signal's rising edge (green) is labeled with two neighboring BCIDs. Then the signal input timing for a particular BCID becomes enlarged by the application of the additional delay in the clock line. The top arrows show time which corresponds to the BCID of "A", "B", "C", and "D", which are superimpose on the blue line, respectively with the delay configuration. The period of the duplication of BCID is determined by the additional delay time in the clock line.

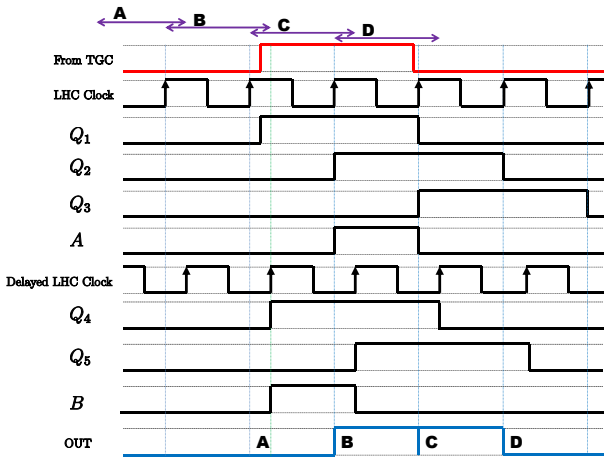

Figure C.1: The BCID gate width functionality. The notations in the schematics of Figure 4.2(a) are used in the timing chart.

Appendix D

Additions for Chapter 5

D.1 The scale factor application to correct the efficiency

In the efficiency measurements of electrons and muons, the measured efficiencies are transformed into the corresponding scale factors. The scale factor is defined to be $SF \equiv \frac{\epsilon_{\rm data}}{\epsilon_{\rm MC}}$ according to the measured efficiencies with collision data and MC ($\epsilon_{\rm data}$ and $\epsilon_{\rm MC}$). The scale factors are transformed into the event weight to correct the detection efficiency in the simulation. In this section, the application of this scale factors to correct the MC are discussed.

D.1.1 The scale factor for the trigger efficiency correction

In the dilepton analyses, two leptons are detected in each of events. Therefore, the trigger requirement is that at least one of the two should pass the trigger. The correction of the event weight is differently applied for the followings two cases: (1) in which both leptons are triggered and (2) only one of them are triggered. In ee final state, $SF(\eta_1) \times SF(\eta_2)$ is applied as event weight in case of (1). In case of (2), $SF(\eta_1) \times \frac{1.-SF(\eta_2)\times\epsilon(\eta_2)}{1.-\epsilon(\eta_2)}$ is applied, where the label of 1 denotes the electrons that pass the trigger, and the label of 2 denotes the electrons that does not pass the trigger [*1]. For the muon, as mentioned in Section 5.3.2, the trigger simulation is not used in the analysis. In $\mu\mu$ final states, the event weight to correct the muon trigger efficiency in the MC can be calculated as $1 - (1 - \epsilon(1))(1 - \epsilon(2))$. In $e\mu$ final sate, the event weight is evaluated to be SF_e if the selected electron passes the trigger requirement. Otherwise $\frac{1-SF_e\times\epsilon_e}{1-epsilon_e} \times \epsilon_\mu$ is used as the event weight.

D.1.2 The scale factor for the selection efficiency correction

The scale factors of the reconstruction, identification, and isolation selection efficiency are transformed into event weight to correct the selection efficiency. The corresponding event weight is evaluated by multiplying the entire scale factors related to the selection.

[*1] $SF(\eta_2)\epsilon(\eta_2)$ represents the measured efficiency in the collision data.

D.2 Signal acceptance

Details of the signal efficiencies at individual selection levels are summarized for ee, $\mu\mu$, and $e\mu$ final states in Table D.1, Table D.2, and Table D.3.

The acceptance is mainly determined by (1) the lepton detection and identification efficiency, (2) the E_T^{miss} selection efficiency for ee and $\mu\mu$ channels, (3) H_T selection efficiency for $e\mu$ channel, (4) efficiency of $|M_{\ell\ell} - M_Z| < 10$ GeV (Z events veto in ee, and $\mu\mu$ channel) and (5) the efficiency of jet multiplicity cuts. The lepton efficiency is determined using data, as discussed in the 5.3.2, and the dilepton selection efficiency is evaluated 19%, 36%, and 26%, ee, $\mu\mu$, and $e\mu$. This corresponds to 43% and 60% efficiency for single electrons and muons, including selection on the phase space ($p_T > 20, 25$ GeV, $|\eta| < 2.5$), and identification. The selection efficiency of H_T cut in $e\mu$ channel for signal and 95%, while the efficiency of E_T^{miss} cut in ee, and $\mu\mu$ channels is 53% and 55% according to the tight E_T^{miss} cuts. The small difference between ee and $\mu\mu$ final states comes from the difference of E_T^{miss} distribution due to the lepton p_T selection difference. The probability with the events have equal to or more than two jets is ≈ 83 % for all the channels. The $H_T$cuts favor events with high p_T jets. This results in higher efficiency of jet cuts in $e\mu$ channel analysis, comparing with the other two channels.

	N_i	N_i/N_1%	N_i/N_{i-1}%
1. True ee	1931.2		
2. ≥ 2 leptons	362.4	19.41	19.41
3. LAr cleaning	341.6	18.30	94.29
4. $E_T^{miss} > 60$ GeV	180.8	9.69	52.93
5. $N_{\text{jets}} \geq 2$	150.0	8.03	82.93
6. $= 2$ leptons	149.9	8.03	99.99
7. Opposite sign	148.9	7.97	99.28
8. $M_{\ell\ell} > 15$ GeV	147,9	7.92	99.39
9. $\|M_{\ell\ell} - M_Z\| > 10$ GeV	124.9	6.69	84.43
10. Truth matching	124.0	6.64	99.24

Table D.1: Expected number of $t\bar{t}$ signals in ee channel, and the selection efficiency. The expectation is scaled into 0.70 fb^{-1}.

D.3 Details of the MC-based background.

The details of the MC-based background are summarized in Table D.4, Table D.5 and Table D.6.

	N_i	N_i/N_1%	N_i/N_{i-1}%
1. True $\mu\mu$	1917.8		
2. ≥ 2 leptons	660.0	35.60	35.60
3. LAr cleaning	624.5	33.68	94.62
4. $E_T^{miss} > 60$ GeV	345.7	18.65	55.36
5. $N_{\text{jets}} \geq 2$	286.5	15.46	82.89
6. $= 2$ leptons	286.5	15.45	99.99
7. Opposite sign	286.5	15.45	99.99
8. $M_{\ell\ell} > 15$ GeV	284.1	15.32	99.17
9. $\lvert M_{\ell\ell} - M_Z \rvert > 10$ GeV	241.3	13.02	84.95
10. Truth matching	241.3	13.02	99.99

Table D.2: Expected number of $t\bar{t}$ signals in $\mu\mu$ channel, and the selection efficiency. The expectation is scaled into 0.70 fb^{-1}.

	N_i	N_i/N_1%	N_i/N_{i-1}%
1. True $e\mu$	3848.2		
2. ≥ 2 leptons	977.8	26.28	26.28
3. LAr cleaning	923.9	24.83	94.48
4. $H_T > 130$ GeV	888.1	23.87	96.13
5. $N_{\text{jets}} \geq 2$	753.2	20.25	84.81
6. $= 2$ leptons	753.0	20.24	99.97
7. Opposite sign	749.4	20.14	99.52
8. Truth matching	745.6	20.04	99.49

Table D.3: Expected number of $t\bar{t}$ signals in $e\mu$ channel, and the selection efficiency. The expectation is scaled into 0.70 fb^{-1}.

	Single top	Diboson	$Z\tau\tau$
Yield(events)	6.4	6.1	4.9
Uncertainty			
Lumi	±3.7	±3.7	±3.7
JES	+11.9/-8.4	+9.4/-7.4	+17.9/-15.0
JER	±2.4	±0.7	±14.5
JEF	±0.4	±0.0	±0.0
MET(SoftJet)	-0.3/-0.6	+0.3/-1.0	-9.0/+0.0
MET(PileUp)	-0.7/-1.0	+0.3/-0.4	-9.0/+0.0
LAr(JetCleaning)	+0.0/-1.5	+0.0/-1.7	±0.0
SF(El.ID)	+5.2/-5.1	+5.4/-5.2	+5.4/-5.2
SF(El.Trig)	+0.9/-0.9	+0.2/-0.2	+0.3/-0.3
x-sec(Theory)	+8.6/-8.6	+5.0/-5.0	+34.4/-34.4
Stat(MC)	±9.0	±12.3	±25.0
Z pT	-	-	±21.9
El.ES	-1.7/+1.6	+0.0/-3.0	±0.0
El.ER	+2.0/-2.5	-1.1/-2.8	+0.0/+0.4
total(syst+lumi)	+18.7/-16.9	+17.5/-17.1	+53.5/-54.1

Table D.4: Uncertainties on the MC background contributions in the ee channel. The uncertainties are presented as $+1\sigma/-1\sigma$ variation of the systematic source.

	Single t	Diboson	$Z\tau\tau$
Yield(events)	16.0	8.9	11.0
Uncertainty			
Lumi	±3.7	±3.7	±3.7
JES	+4.2/-7.2	+7.2/-13.1	+9.8/-16.1
JER	±0.9	±2.4	±11.5
JEF	±0.0	±0.0	±0.0
MET(SoftJet)	-0.5/+0.4	-1.0/+1.7	+1.2/+3.8
MET(PileUp)	-0.2/+0.1	-1.5/+1.4	+1.2/+0.0
LAr(JetCleaning)	-0.1/-1.2	+0.5/+0.0	+0.0/-4.0
SF(Mu.ID)	+1.1/-1.1	+1.1/-1.1	+1.1/-1.1
SF(Mu.Trig)	+0.2/-2.0	+0.2/-1.9	+0.3/-1.8
x-sec(Theory)	+8.6/-8.6	+5.0/-5.0	+35.8/-35.8
Stat(MC)	±5.8	±9.2	±14.8
Z pT	-	-	±15.6
Mu.ES	-0.0/-0.1	±0.0	±0.0
Mu.ER(MS)	-0.1/+0.4	+1.0/-0.7	±0.0
Mu.ER(ID)	-0.4/-0.4	+0.1/-0.3	±0.0
total(syst+lumi)	+11.9/-13.5	+13.7/-17.6	+44.8/-46.6

Table D.5: Uncertainties on the MC background contributions in the $\mu\mu$ channel. The uncertainties are presented as $+1\sigma/-1\sigma$ variation of the systematic source.

	Single Top	Diboson	$Z\tau\tau$
Yield(events)	41.1	33.5	42.5
Uncertainty			
Lumi	±3.7	±3.7	±3.7
JES	+8.6/-7.7	+12.1/-11.4	+7.2/-13.1
JER	±0.4	±2.2	±2.5
JEF	±0.2	±0.2	±0.0
LAr(JetCleaning)	+0.7/-1.2	+0.7/-0.6	+0.0/-0.7
SF(El.ID)	+2.6/-2.6	+2.6/-2.6	+2.7/-2.7
SF(El.Trig)	-0.2/+0.2	+0.1/-0.1	+0.4/-0.4
SF(Mu.ID)	+0.6/-0.6	+0.6/-0.6	+0.5/-0.5
SF(Mu.Trig)	±0.0	+0.0/-0.1	±0.0
x-sec(Theory)	+8.6/-8.6	+5.0/-5.0	+35.0/-35.0
Stat(MC)	±3.8	±5.1	±8.4
Z pT	-	-	±0.4
El.ES	+0.2/-0.4	+0.7/-0.0	+1.6/-0.0
El.ER	-0.1/-0.3	-0.0/+0.9	+0.6/+1.0
Mu.ES	+0.0/-0.1	±0.0	±0.0
Mu.ER(MS)	+0.0/-0.1	±0.0	±0.0
Mu.ER(ID)	-0.1/+0.0	±0.0	±0.0
total(syst+lumi)	+13.6/-13.1	+15.0/-14.4	+37.1/-38.7

Table D.6: Uncertainties on the MC background contributions in the $e\mu$ channel. The uncertainties are presented as $+1\sigma/-1\sigma$ variation of the systematic source.

Bibliography

[1] The ATLAS Collaboration, G. Aad et al., *The ATLAS Experiment at the CERN Large Hadron Collider*, JINST 3 S08003 (2008).

[2] Lyndon Evans and Philip Bryant, *LHC Machine* CJINST 3 S08001 (2008).

[3] F. Abe et al., *Observation of the top quark production in $p\bar{p}$ collisions with the Collider Detector at Fermilab*, Phys. Rev. Lett. **74** (1995) 2626.

[4] D0 Collaboration, S.Abachi et al., *Observation of the top quark*, Phys. Rev. Lett. **74** (1995) 2632-2637.

[5] The Tevatron Electroweak Working Group for the CDF and D0 Collaborations, *Combination of CDF and D0 results on the mass of the top quark using up to 5.8 fb^{-1} of data*, 2011, arXiv:1107.5255v3.

[6] S. Moch and P. Uwer, *Theoretical status and prospects for top-quark pair production at hadron colliders*, Phys. Rev. D78 (2008) 034003.

[7] Siegfried Betheke, *The 2–0 World Average of α_s*, arXiv:0908.1135.

[8] V.N. Gribov, L,N. Lipatov, *Deep inelastic e p scattering in perturbation theory*, Sov.J.Nucl.Phys. 15:438 (1972).

[9] Pumplin, J. and others, *New generation of parton distributions with uncertainties from global QCD analysis*, JHEP 07 (2002) 012, arXiv:hep-ph/0201195.

[10] Nadolsky, Pavel M. and others, *Implications of CTEQ global analysis for collider observables*, Phys. Rev. D78 (2008) 013004, dx.doi.org/10.1103/PhysRevD.78.013004, arXiv:hep-ph/0802.0007.

[11] S. Frixione, P. Nason and B.R. Webber. *Matching NLO QCD and parton showers in heavy flavour production*, JHEP 08 (2003) 007, arXiv:hep-ph/0305252.
S. Frixione, E. Laenen and P. Motylinski, *Single-top production in MC@NLO*, JHEP 03 (2006) 092, arXiv:hep-ph/0512250. The version 3.41 are used in the analyses.

[12] R. Barate and others (LEP Working Group for Higgs boson searches and ALEPH, DELPHI, L3, and OPAL Collaborations), *Search for the standard model Higgs boson at LEP*, Phys. Lett. **B 565** (2003) 61-75, arXiv:hep-ex/030633.

[13] The ATLAS collaboration, *Combination of Higgs Boson Searches with up to 4.9 fb-1 of pp Collisions Data Taken at a center-of-mass energy of 7 TeV with the ATLAS Experiment at the LHC*, ATLAS-CONF-2011-163 (2012).

[14] The CMS Collaboration, *Combination of SM Higgs Searches*, CMS-PAS-HIG-11-032 (2012).

[15] The ALEPH, CDF, D0, DELPHI, L3, OPAL, SLD Collaborations, the LEP Electroweak Working Group, the Tevatron ElectroweakWorking Group,and the SLD electroweak and heavy flavour groups, *Precision Electroweak Measurements and Constraints on the Standard Model*, arXiv:hep-ex/1012.2367v2 (2010).

[16] J.Ellis, K.A.Olive *Supersymmetric Dark Matter Candidate*, arXiv:1001.3651 (2010).

[17] J.L.Diaz-Cruz et al., *On the Feasibility of a Stop NLSP in Gravitino Dark Matter Scenarios*, arXiv:hep-ph/0701229 (2007).

[18] The ATLAS Collaboration, *Luminosity Determination in pp Collisions at* $\sqrt{s} = 7$ TeV *using the ATLAS Detector in 2011*, ATLAS-COM-CONF-2011-116.

[19] M. Cacciari, G.P. Salam and G. Soyez, *The anti-k_t jet clustering algorithm*, JHEP **04** (2008) 063.
M. Cacciari and G. P. Salam, *Dispelling the N^3 myth for the k_t jet-finder*, Phys. Lett. **B 641** (2006) 57.

[20] The ATLAS Collaboration, G. Aad et al., *Measurement of inclusive jet and dijet cross-sections in proton-proton collisions at 7 TeV centre-of-mass energy with the ATLAS detector*, Eur. Phys. J. **C 71** (2011).

[21] *Martin-Stirling-Thorne-Watt Parton Distribution Functions*, http://projects.hepforge.org/mstwpdf.

[22] ATLAS Muon Collaboration, *ATLAS Muon Spectrometer Technical Design Report*, CERN/LHCC 97-22 (1997).

[23] S. B. Huq and J. Goldie, *An Overview of LVDS Technology*, AN-971 (1998).

[24] The ATLAS Collaboration, *Luminosity Determination in pp Collisions at* $\sqrt{s} = 7$ TeV *using the ATLAS Detector at the LHC*, Eur. Phys. J. **C71** (2011) 1630.

[25] *ATLAS Trigger Operation Public Results*, https://twiki.cern.ch/twiki/bin/view/AtlasPublic/TriggerOper

[26] G. Corcella et al., *HERWIG 6.5: an event generator for Hadron Emission Reactions With Interfering Gluons (including supersymmetric processes)*, JHEP 01 (2001) 010, arXiv:hep-ph/0011363;
G. Corcella et al., HERWIG 6.5 release notes, arXiv:hep-ph/0210213.

[27] J. M. Butterworth et al., *Multiparton interactions in photoproduction at HERA*, Z. Phys. C72 (1996) 637.

[28] S. Agostinelli et al., *GEANT4, a simulation toolkit*, Nucl. Instr. Meth. **A 506** (2003) 250.

[29] The ATLAS Collaboration, G. Aad et al., *The ATLAS Simulation Infrastructure*, Eur. Phys. J. **C 70** (2010) 823.

[30] M. Aliev, H. Lacker, U. Langenfeld, S. Moch, and P. Uwer, *HATHOR*, http://www.physik.hu-berlin.de/pep/tools.

[31] Kidonakis, Nikolaos, *Next-to-next-to-leading-order collinear and soft gluon corrections for t-channel single top quark production*, Phys. Rev.**D83** (2011) 091503.

[32] J. M. Campbell and R. K. Ellis, An update on vector boson pair production at hadron colliders, Phys. Rev. **D60** (1999) 113006.

[33] M.L. Mangano et al., *ALPGEN, a generator for hard multiparton processes in hadronic collisions*, JHEP 07 (2003) 0013.

[34] J. Pumplin et al., *New generation of parton distributions with uncertainties from global QCD analysis*, JHEP 07 (2002) 012, arXiv:hep-ph/0201195.

[35] ATLAS Collaboration, *Jet energy scale and its systematic uncertainty in proton-proton collisions at sqrt(s)=7 TeV in ATLAS 2010 data* , ATLAS-CONF-2011-032.

[36] P. Nason, *A new method for combining NLO QCD with shower Monte Carlo algorithms*, JHEP 11546 (2004) 040.

[37] Frixione, Stefano and Nason, Paolo and Oleari, Carlo, *Matching NLO QCD computations with Parton Shower simulations: the POWHEG method*, JHEP 11 (2007) 070.

[38] Alioli, Simone and Nason, Paolo and Oleari, Carlo and Re, Emanuele, *A general framework for implementing NLO calculations in shower Monte Carlo programs: the POWHEG BOX*, JHEP 06 (2010) 043.

[39] T. Sjstrand, S. Mrenna and P. Skands, *PYTHIA 6.4 physics and manual*, JHEP05 (2006) 026.

[40] B.P. Kersevan and E.Richter-Was, *The Monte Carlo Event Generator AcerMC version 2.0 with interfaces to PYTHIA 6.2, HERWIG 6.5 and ARIADNE 4.1*, arXiv:hep-ph/0405247.

[41] , Skands, Peter Zeiler, *Tuning Monte Carlo Generators: The Perugia Tune*, Phys. Rev. D**82**, 2010, arXiv:1005.3457[hep-ph].

[42] G. Aad et al., ATLAS Collaboration, Expected Performance of the ATLAS Experiment - Detector, Trigger and Physics, CERN-OPEN-2008-020, arXiv:0901.0512 [hep-ex], pages 880–881.

[43] Richard D. Ball et al., *A first unbiased global NLO determination of parton distributions and their uncertainties*, arXiv:1002.4407v2.

[44] A.D. Martin, W.J. Stirling, R.S. Thorne, G. Watt, *Parton distributions for the LHC*, Eur. Phys. J.C **63** 189-285 (2009), arXiv:0901.0002.

[45] Campbell, John M. and Ellis, R. K., MCFM for the Tevatron and the LHC, Nucl. Phys. Proc. Suppl (2010), doi:10.1016/j.nuclphysbps.2010.08.011.

[46] The ATLAS Collaboration, *Performance of the ATLAS Secondary-Vertex b-tagging Algorithm in 7 TeV collision data*, ATL-CONF-2010-042.
The ATLAS Collaboration, *Calibrating the b-Tag and Mistag Efficiencies of the SV0 b-Tagging Algorithm in 3* pb^{-1} *of Data with the ATLAS Detector*, ATL-CONF-2010-099.

[47] ATLAS Collaboration, *Measurement of the top-quark pair production cross-section in pp collisions at* $\sqrt{s} = 7\ TeV$ *in dilepton final states with ATLAS.* ATLAS-CONF-2011-100.

[48] ATLAS Collaboration, *Measurement of the ttbar production cross-section in pp collisions at* $\sqrt{s} = 7\ TeV$ *using kinematic information of lepton+jets events* ATLAS-CONF-2011-122.

[49] CDF Collaboration, *Combination of CDF top quark pair production cross-section measurements with up to 4.6* fb^{-1}, Conf Note 9913.